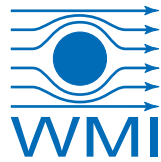




TECHNISCHE
UNIVERSITÄT
MÜNCHEN



WALTHER-MEISSNER-
INSTITUT FÜR TIEF-
TEMPERATURFORSCHUNG



BAYERISCHE
AKADEMIE DER
WISSENSCHAFTEN

Circuit quantum electrodynamics with a transmon qubit in a 3D cavity

Master's Thesis
Gustav Andersson

Supervisor: Prof. Dr. Rudolf Gross
Munich, March 2015

Contents

1	Introduction	1
2	Theory	3
2.1	Josephson Junctions	3
2.2	Superconducting qubits	5
2.2.1	The Cooper pair box	6
2.2.2	The transmon qubit	7
2.3	Cavity resonators	10
2.4	Cavity QED and 3D circuit QED	15
2.4.1	Jaynes-Cummings model	16
2.4.2	Dispersively coupled transmon	16
2.4.3	The coupling strength	19
3	Experimental methods and simulations	21
3.1	Aluminium cavities	21
3.1.1	Room temperature setup	23
3.1.2	Cryogenic setup	24
3.2	Qubit spectroscopy	27
3.2.1	3D Transmon	27
3.2.2	Two-tone spectroscopy setup	28
3.3	Simulations	32
3.3.1	Magnetic flux coupling	35
3.3.2	Dual cavity simulation results	36
3.3.3	Bias line filtering	39
4	Experimental results	43
4.1	Cavity characterization	43
4.1.1	Room temperature characterization	43
4.1.2	Frequency tuning	47
4.1.3	Cavities at cryogenic temperatures	50
4.2	Qubit spectroscopy	54
4.2.1	Two-tone continuous wave readout	54
4.2.2	High power spectroscopy	59

4.2.3	ac Stark shift and photon number calibration	63
4.2.4	Dressed cavity transmission spectrum	63
5	Conclusions and outlook	67
A	Dual cavity measurement	71
B	Cavity technical data	73
C	Time domain setup	77
 Bibliography		79
 Acknowledgement		84

List of Figures

2.1	Schematic drawing of an SIS Josephson junction. An insulating oxide barrier separates the two superconducting electrodes.	5
2.2	Bloch sphere schematic. Pure qubit states $ \psi\rangle$ are often represented in spherical coordinates. In this basis we have $ \psi\rangle = e^{i\varphi} \sin\left(\frac{\vartheta}{2}\right) 0\rangle + \cos\left(\frac{\vartheta}{2}\right) 1\rangle$. The polar coordinates are not to be confused with the superconducting phase variables.	6
2.3	Circuit diagram of the Cooper pair box. Charges tunnel onto the island through the Josephson junction, represented by the crossed square. . . .	7
2.4	The transmon qubit equivalent circuit. Compared to the Cooper pair box, an extra capacitance has been added between the island and ground. . .	8
2.5	The first four energy levels of the charge qubit as a function of n_g , plotted for different values of E_J/E_C . The levels are eigenenergies of the Hamiltonian of Eq. (2.7).	9
2.6	Schematic illustration of the 3D transmon design. The pad structures provide the shunt capacitance as well as the resonator coupling. The Josephson junction is marked with the junction energy E_J and junction capacitance E_J . The length of the qubit structure l influences the dipole moment of the structure, which is critical to the electric field coupling. .	10
2.7	Equivalent circuit diagram and 3D schematic design of a tunable transmon. The effective Josephson energy is altered by coupling an external magnetic flux into the split junction loop.	11
2.8	The resonator transmission lineshape is a Lorentzian. The bandwidth of the transmission is determined by the loss rate.	12
2.9	Schematic of a rectangular cavity resonator (top). Electric field distribution of the TE_{101} (bottom left) and TE_{102} (bottom right) modes on the schematic cutplane. The field is polarized perpendicular to the figure plane. . . .	14
2.10	3D cQED schematic	15
2.11	Time evolution of the qubit excited state occupation in the Jaynes-Cummings model for different values of the detuning simulated using QuTiP. The resonant case leads to the entire excitation energy oscillating between qubit and cavity. In the detuned limit, the exchange of energy is blocked almost completely.	17

3.1	CAD generated drawing of the pure aluminium cavity. The alloy cavity has identical internal dimensions, but differs in that the top and bottom metal hull is thicker	22
3.2	Profile drawings showing the internal dimensions of the cavities.	22
3.3	Photographs showing the pure aluminium cavity (left) as well as a pin connector along with samples of the spacers used to adjust the pin insertion depth (right). The numbers on the spacers indicate their height in mm.	22
3.4	The alloy cavity following modifications introducing a magnetically permeable copper face as well as a tuning screw.	23
3.5	The cryogen-free dilution refrigerator used for low-temperature experiments.	25
3.6	Bottom view of the cryostat mixing chamber plate. Both cavities are mounted at the sample stage and connected to the microwave switches. .	25
3.7	Circuit diagram of the cryogenic setup used to measure transmission of both the alloy and pure aluminium cavities. The coloured boxes indicate temperature stages of the cryostat.	26
3.8	SEM micrograph of a Josephson junction, as schematically represented in Fig. 2.1.	27
3.9	Microscopy image of the transmon sample. The junction is in the center line between the pads, which are 50 μm apart. The gridded pads have 20 μm by 20 μm cells and the bars are 5 μm wide. During fabrication, the aluminium has not been removed entirely from the grid cells. The blue bar near the bottom is a 100 μm length scale reference.	28
3.10	Alloy cavity with a silicon wafer mounted. At cryogenic temperatures, thermal and mechanical coupling is ensured by adding Indium to the spherical corners of the milled chip frame.	29
3.11	The pure aluminium cavity mounted at the sample stage for qubit spectroscopy. The power splitter in the foreground enables sharing an input line with another experiment.	29
3.12	Circuit diagram of the cryogenic setup used in two-tone spectroscopy. The probe and drive signals are mixed at room temperature using a power combiner. The coloured boxes indicate temperature stages of the cryostat.	31
3.13	CST model of the cavity with a mounted transmon wafer. The dimensions shown in Fig. 3.2. Waveguide ports are added to the model at the top end of the metallic pins, modelled after the Huber and Suhner connectors. The blue colour represents vacuum, brown teflon, grey PEC and the silicon wafer is shown in green.	33

3.14	CST model of flux bias line with $\lambda/4$ filter stubs. The substrate is 26.5 mm long and 3 mm wide and has a thickness of 0.25 mm. The material is modelled after sapphire and has a relativ dielectric constant of $\epsilon_r = 11.5$. The stubs vary in length between 5.1 mm and 6.5 mm. The metal structures are 1 μm thick and 10 μm to 15 μm wide.	34
3.15	CST model of the two cavity model, highlighting the qubit and bias line structures. The top right inset shows the port numbering relevant to the S-parameter calculations.	34
3.16	CST simulation of magnetic field penetration from an external coil through a copper face of the cavity. The field value at the transmon chip is relevant to flux bias tuning, and amounts to $B = 4.3 \mu\text{T}$	35
3.17	CST simulation of the electric field distribution from a near-resonant excitation in a two-cavity model (logarithmic scale). The simulated input power is 1 W.	36
3.18	Cross-section of CST simulation of the electric field distribution showing the transmon structure (logarithmic scale). The propagation of the electric field through the flux bias line is clearly suppressed by the $\lambda/4$ stubs. The simulated input power is 1 W.	37
3.19	S-parameter simulation results of intra-cavity (S_{21}) and cross-cavity (S_{41}) transmission with the bridge transmon mounted and pin depth -1.6 mm at all ports.	38
3.20	S-parameter simulation results of intra-cavity (S_{21}) and cross-cavity (S_{41}) transmission with the bridge transmon mounted and pin depth 1.4 mm at all ports.	38
3.21	Time evolution of a qubit coupled resonantly to two cavities. The coupling g , resonator loss and qubit dephasing parameters are derived from the experimental results of Ch. 4. Direct photon exchange between the resonator is assumed to occur at a rate g_{AB} much lower than the qubit-resonator coupling frequency ($g = 10g_{AB}$). The initial state corresponds to a single photon in one of the cavities.	39
3.22	Electric Field distribution from CST simulation of a flux bias line model with $\lambda/4$ filter stubs. The excitation is introduced at the qubit side, where the line is parallel to the short end of the substrate. The simulated excitation frequency is 4.5 GHz, inside the stop-band of the filter stubs.	40
3.23	Simulated transmission $ S_{21} $ between the two endpoints of the bias line, meaning the signal travels through both branches.	41
4.1	Resonant volume defined for simulations in the CST environment (top) and simulated electric field distribution of fundamental cavity mode at 1 W input power (bottom).	44

4.2	Broad frequency sweep of the alloy cavity transmission at room temperature. The peaks corresponding to the first and second cavity modes are marked. The VNA power is set at -10 dBm.	45
4.3	Cavity transmission spectrum data and fit at room temperature compared to simulation. Fitted parameters are shown next to the corresponding peaks. The differences in resonance frequency ($\sim 3\%$) and Q ($\sim 10\%$) are caused mainly by fabrication issues. The different transmission magnitude is attributed to the pin depth calibration.	45
4.4	Quality factor vs. pin insertion depth for simulated and measured configurations.	46
4.5	Alloy cavity transmission with a silicon wafer of the type used as substrate for qubit structure mounted in the center. The first mode is suppressed at room temperatures, where the silicon has a high impurity conductivity.	47
4.6	Quality factor and resonance frequencies for alloy cavity tuning by pin depth variation. Data points are annotated with the pin depth.	48
4.7	Quality factor and resonance frequencies for alloy cavity tuning by dielectric and shape perturbation. We use the absolute value of the frequency change as the different tuning mechanisms lead to shifts of different sign.	48
4.8	Transmission data (dots) and fit (line) for the alloy cavity at 50 mK before electropolishing. The resonance linewidth (FWHM) equals 15.3 kHz. The measurement is done with a pin depth of -1.1 mm.	51
4.9	Transmission data (dots) and fit (line) for the alloy cavity at 50 mK after electropolishing. The resonance linewidth (FWHM) equals 18.1 kHz. The measurement is done with a pin depth of -1.1 mm.	51
4.10	Calibrated transmission data (dots) and fit (line) for the pure aluminium cavity at 50 mK. The resonance linewidth (FWHM) equals 8.43 kHz. The measurement is done with a pin depth of -1.6 mm.	52
4.11	Loaded quality factor versus estimated input power at the cavity at 50 mK for the aluminium cavity. Single photon power corresponds to an input power of -115 dBm.	53
4.12	Probe tone phase shift data vs. drive frequency. The probe tone power is -42 dBm (average photon number $n_p = 0.5$). at the frequency $f_p = 5.4635$ GHz.	55
4.13	(a) Qubit two-tone spectroscopy. Colourscale indicates phase shift ϕ in degrees of the probe signal, at $f_p = 5.4635$ GHz. The reduced phase shift is observed when the drive tone excites the qubit out of the ground state. Increasing the readout power leads to broadening and ac Stark shift of this transition. The drive tone power is -15 dBm. (b) Qubit transition frequency at different readout powers. The data points are obtained from the best fit (Lorentzian or Gaussian) to two-tone spectroscopy data.	56

4.14 Qubit two-tone spectroscopy in the low power limit. Colourscale indicates phase shift ϕ in degrees of the probe signal, at $f_p = 5.4635$ GHz. The drive tone power is -25 dBm.	57
4.15 Squared qubit linewidth (FWHM) as a function of input power. Linear fit extrapolated to zero power for T_2 estimate.	57
4.16 Qubit two-tone spectroscopy sweeping the drive power. At high drive powers, it is possible to discern the second qubit transition. The probe power amounts to -35 dBm ($n_p = 2.5$).	58
4.17 (a) Two-tone spectroscopy with strong drive. (b) Frequencies for the first and second transition. (c) Anharmonicity $f_{01} - f_{12}$. The drive power is 5 dBm.	58
4.18 (a) Single tone spectroscopy power sweep. At high readout power, the cavity frequency is abruptly downshifted. No qubit drive is applied in this measurement. (b) Two-tone spectroscopy power sweep with -10 dBm drive tone at 3.65 GHz. Due to the ac Stark shift, this drive has a considerable detuning from the first qubit transition. (c) Two-tone spectroscopy power sweep with -10 dBm drive tone at 5.4635 GHz. When driving at the upper branch frequency, the lower branch resonance is observed at all readout powers. (d) Two-tone spectroscopy power sweep with -10 dBm drive tone at 3.58 GHz.	60
4.19 Cavity spectra without qubit drive for different readout powers. At $P_p = -15$ dBm ($n_p = 250$), both branches are observed to coexist.	61
4.20 Cavity model with transmon mounted in the experimental configuration. The image shows the electric field distribution for one half of the cavity, with the cut through the transmon wafer. The simulated input power is 1 W and the pin depth 1.4 mm.	62
4.21 Qubit frequency vs. readout photon population in the cavity. The photon number calibration is obtained by comparing qubit frequency data (red boxes) to the ac Stark shift estimated from the coupling strength calculated from the dispersive shift in Sec. 4.2.2. This estimated ac Stark shift (black dotted line) is plotted for comparison. Fitting a line to the qubit frequency (red line) gives an additional estimate g_{fit} for the coupling strength. The fit is restricted to data below $n_p = 2.5$.	64
4.22 Qubit two-tone spectroscopy. Both the drive and readout frequencies are varied in order to observe the effect on the cavity resonance. Colourscale indicates transmission. The resonance frequencies (red line) are obtained by Lorentzian fit, and show a shift when driving at the qubit frequency.	65
4.23 Dressed cavity frequency as a function of qubit drive frequency and readout power. The cavity frequency minima occur at different drive frequencies due to the ac Stark shift of the qubit. The drive power is -10 dBm.	66

5.1	Rendered image of CAD drawing of the two-cavity concept. The dimensions are those of the simulated 3D model.	69
-----	---	----

Chapter 1

Introduction

Quantum information processing is a rapidly advancing field of physics showing great potential for future applications in the computing industry. The fundamental component of quantum information systems is the quantum bit (qubit), a quantum two-level system whose state can be read and manipulated in a controlled manner. Using arrays of such qubits coupled together, quantum superposition and entanglement of states could enable the implementation of certain algorithms providing an immense increase in efficiency as compared to classical computing. The perhaps most famous example is Shor's algorithm for factorizing integers, with potentially great implications for modern cryptography. On an ideal quantum computer, this algorithm finds the prime factors of any integer in polynomial time [1].

Among the most promising candidates for realizing quantum computing are superconducting qubits. These are electric circuits based on the special physical properties of the Josephson junction, a circuit element with a nonlinear inductance [2]. Named after British physicist Brian Josephson, the Josephson junction consists of two superconducting metal electrodes separated by a thin insulating layer, typically a few nanometres thick. The integration of Josephson junctions into electric circuits has given rise to the field circuit quantum electrodynamics (QED). In this field, circuits play the roles of natural atoms and optical cavities in quantum-optical cavity QED. Thanks to the macroscopic nature of quantum phenomena in superconductivity, qubit properties can to a large extent be engineered to meet desired specifications, rather than just relying on the natural properties of atoms or molecules. Using well developed microwave engineering principles, circuit QED enables study of light-matter interaction by coupling qubits to resonant structures, such as coplanar waveguide resonators.

Due to their size, superconducting qubits are difficult to isolate from their environment. The quantum states necessary for quantum computing or other experimental schemes are sensitive to stray fields and thermal noise. The preservation of the quantum properties of the system, coherence, is therefore an important aspect of qubit design. The transmon qubit [3], conceived in 2007, is designed to mitigate this problem by reducing sensitivity to fluctuations in local electric charge density in the sample. This has helped maintain the strong trend in increasing coherence times for superconducting qubit designs.

In recent developments, the planar circuits where the qubit is embedded have been replaced by three-dimensional cavity resonators. Such configurations offer several advantages, in particular towards coherence. As qubits decay from excited states by emitting a photon, the mode volume of the final photon state may significantly affect this process. These so-called 3D transmons therefore combine the high coupling strength of typical superconducting qubits with long coherence times. This is typically challenging to achieve as strong coupling to the cavity fields usually implies strong coupling also to the environment, inducing loss of coherence. Times for excited state qubit decay, commonly denoted T_1 , close to 100 μs have been recorded [4].

In this thesis, we characterize superconducting cavities for use with transmon qubits. We employ microwave measurement techniques and cryogenics to determine the cavity transmission properties. We proceed to investigate a system with a transmon coupled to a cavity resonator in 3D circuit QED experiments. Using microwave spectroscopy in a dilution refrigerator setup, the qubit parameters and the properties of the combined system are investigated experimentally.

A long-term goal of this project is to extend the qubit-cavity system to a network of two or more resonators, with qubit-mediated interaction. Such a system may allow experimental studies of entangled photon states, where a single photon may be present in different cavities simultaneously. It also shows promise for quantum information processing applications, due to the increased coherence times accessible in cavity resonators. This thesis therefore includes preliminary analysis towards such implementations, mainly from a microwave engineering analysis point of view.

We begin in Ch. 2 by introducing fundamental theoretical concepts regarding superconducting circuits, cavity resonators and light-matter interaction. Having laid the foundation to the investigations carried out in this work, we proceed in Ch. 3 to describe the particulars of the experimental design and setup involved. This section also contains the numerical methods used and the simulation results. The main results obtained are presented in Ch. 4, starting with cavity characterization data. We then outline the results obtained from qubit spectroscopy in single as well as two-tone measurements. Finally, Ch. 5 states our conclusions and provides an outlook.

Chapter 2

Theory

In this section, we introduce the theoretical aspects underlying the experiments carried out and the results presented in this work. The fundamentals of Josephson junctions are discussed, and the relevant energy scales for applications in superconducting circuits are introduced. We outline the principles of superconducting charge qubit circuits and their operation. In particular, the properties and ideas behind the transmon qubit are described.

We also introduce the classical theory of three-dimensional electromagnetic resonators necessary for the investigated implementations. The qubit and resonator theory are then combined to discuss the fundamentals of light-matter interaction in a quantum mechanical picture. These principles are then applied to the parameter range relevant to our experimental configurations.

2.1 Josephson Junctions

A fundamental element in any superconducting qubit design is the Josephson junction, consisting of two superconducting electrodes separated by a thin insulating barrier. In the macroscopic quantum model of superconductivity [5], the density of the superconducting charge carrier component is related to a macroscopic wavefunction of definite magnitude and phase

$$\Psi(\mathbf{r},t) = |\Psi(\mathbf{r},t)| \cdot e^{i\theta(\mathbf{r},t)} = \sqrt{n(\mathbf{r},t)} e^{i\theta(\mathbf{r},t)}. \quad (2.1)$$

The squared magnitude of this wavefunction gives the density $n = n(\mathbf{r},t)$ of the superconducting charge carriers. The presence of a phase θ gives rise to macroscopic quantization and interference phenomena. The origin of this macroscopic state in the formation of electron pairs, called Cooper pairs, of charge $2e$ and spin zero, is explained by the theory of Bardeen, Cooper and Schrieffer (BCS theory) [6].

In a Josephson junction, the separation between two superconducting electrodes is sufficiently small to create a weak coupling between them. The macroscopic superconducting wavefunctions of the electrodes overlap, leading to the tunnelling of Cooper pairs across the barrier. The Josephson junction is so named because of Brian Josephson's prediction

of the Josephson relations for this system, in 1962 [7]. The first Josephson equations reads

$$I_s = I_c \sin(\phi). \quad (2.2)$$

This equation, the current-phase relation, describes the supercurrent flow between the electrodes. The relative phase between the superconductors is given by $\phi = \theta_2 - \theta_1$ and I_c is the critical current, the maximum supercurrent the Josephson current can sustain in a zero voltage state. The second Josephson relation concerns the time evolution of the phase difference when a voltage is applied across the junction,

$$\frac{d\phi}{dt} = \frac{2\pi}{\Phi_0} V. \quad (2.3)$$

This equation is known as the voltage-phase relation. The factor Φ_0 entering on the right-hand side is the magnetic flux quantum, and is equal to $h/2e$. The way both current and voltage are related to the phase causes the Josephson junction to act as a non-linear inductance. In electric circuits, inductances are associated with stored magnetic field energy. The Josephson junction likewise accumulates potential energy, but rather than in a magnetic field it is stored in the kinetic energy of the moving electrons [8]. This *Josephson coupling energy* is given by

$$U = \frac{\Phi_0 I_c}{2\pi} (1 - \cos \phi). \quad (2.4)$$

This energy, whose scale is set by $E_J = \Phi_0 I_c / 2\pi$, will turn out to be important to Josephson junction based qubit schemes. Due to the parallel geometry of the superconducting electrode faces, the Josephson junction also has a capacitance. This gives rise to a capacitive charging energy whenever there is a potential difference across the junction. The relevant scale for this energy is set by $E_C = e^2 / 2C$, where C is the junction capacitance.

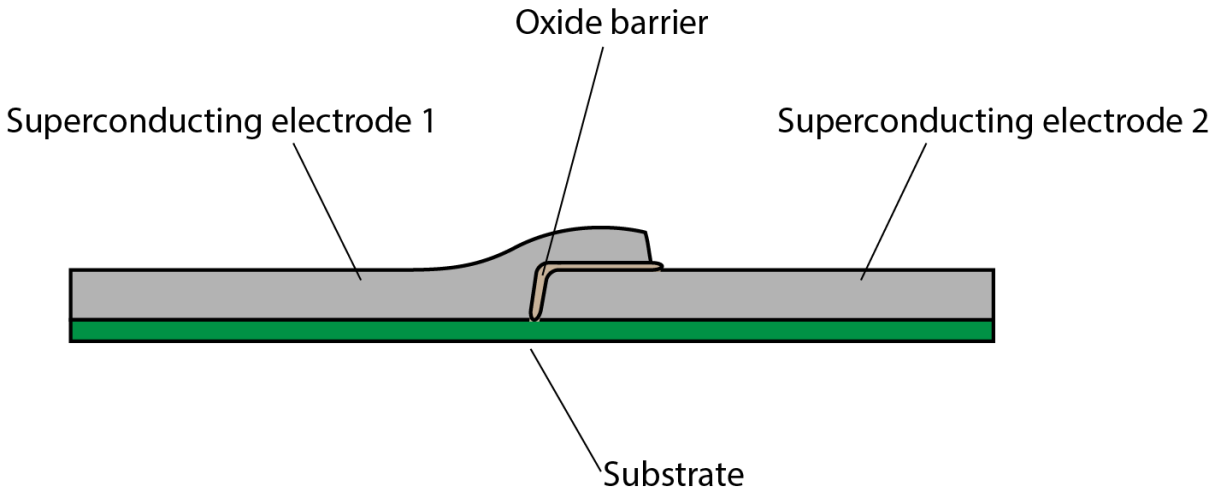


Figure 2.1: Schematic drawing of an SIS Josephson junction. An insulating oxide barrier separates the two superconducting electrodes.

Figure 2.1 shows a schematic drawing of a Josephson junction with a thin oxide tunnel barrier. It is worth noting that although Brian Josephson's original theoretical predictions were made considering a system as described above with a superconductor-insulator-superconductor (SIS) structure, the Josephson relations also hold for other types of weak links between superconductors. Examples include a barrier of normal state, non superconducting metal as well as a constriction in the form of a bottleneck-like narrow section of the superconductor [9].

2.2 Superconducting qubits

When cooled down to sufficiently low temperatures, where $k_B T \ll E_J, E_C$, Josephson junction circuits exhibit quantum properties. The junction charge and phase variables Q and ϕ then have to be replaced by operators, which crucially obey a quantum commutation relation

$$[\hat{\phi}, \hat{Q}] = 2ie. \quad (2.5)$$

The charge operator \hat{Q} is thus canonically conjugate to the phase, similarly to the position and momentum operators, meaning that they are subject to Heisenberg's uncertainty principle. This implies that if ϕ is well defined, Q fluctuates strongly and vice versa. This quantum behaviour is the basis for turning superconducting circuits into qubits.

Any quantum two-level system is analogous to a spin 1/2 system, elegantly described by the Pauli matrices [10]. In this picture, the qubit excited and ground states $|1\rangle$ and $|0\rangle$ are the eigenstates of σ_z . General qubit states in this basis are represented using the Bloch sphere, a unit sphere centered at the origin of a cartesian coordinate system. A point within the enclosed volume corresponds to an expectation value $\mathbf{R} = \langle \vec{\sigma} \rangle$. Qubit operation

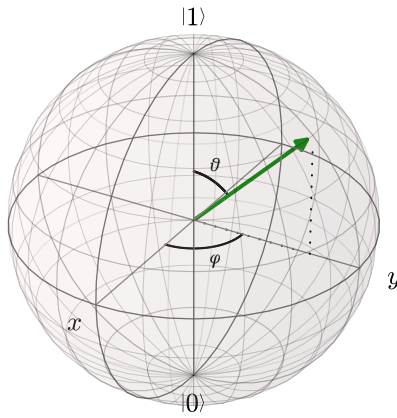


Figure 2.2: Bloch sphere schematic. Pure qubit states $|\psi\rangle$ are often represented in spherical coordinates. In this basis we have $|\psi\rangle = e^{i\varphi} \sin\left(\frac{\vartheta}{2}\right) |0\rangle + \cos\left(\frac{\vartheta}{2}\right) |1\rangle$. The polar coordinates are not to be confused with the superconducting phase variables.

implies manipulation and control of this Bloch vector \mathbf{R} . The norm of the Bloch vector is preserved under unitary time evolution and states on the surface of the Bloch sphere ($|\mathbf{R}| = 1$) are possible observable eigenstates. Such a "pure" state is illustrated in Fig. 2.2. States in the interior $|\mathbf{R}| < 1$ correspond to a statistical mixture, representing a lack of precise knowledge of the quantum state. Such states are probabilistic in a classical sense, not related to quantum uncertainty, and the irreversible time evolution that increases this mixing is one of the major obstacles to successful qubit operation.

The cause of this loss of certainty and the reason we consider it irreversible is that it arises from interaction with the environment, due to the naturally imperfect isolation of the qubit system. Two characteristic timescales are relevant to describe this process. The decay time, $T_1 = 1/\pi\Gamma_1$, is the inverse rate of depopulation of the excited qubit state. The loss of quantum coherence, corresponding to a projection of the Bloch vector onto the z -axis, occurs in the characteristic time $T_2 = 1/\pi\Gamma_2$. As states outside the Bloch sphere are unphysical, depopulation must be accompanied by a certain decoherence, leading to the limit $\Gamma_2 \geq \Gamma_1/2$.

2.2.1 The Cooper pair box

The single Cooper pair box (CPB) couples a small superconducting island via a Josephson junction to a gate electrode. Figure 2.3 shows an equivalent circuit diagram. Two characteristic energies are of interest for this system. The capacitive coupling of the island to the environment produces a charging energy when a gate voltage is applied or the island carries excess charge. This island is sufficiently small to make a single Cooper pair the relevant charge scale (hence its name), leading us to introduce the dimensionless charge variable $n = Q/2e$ and modify the charging energy scale $E_C = e^2/2C_\Sigma$ to account

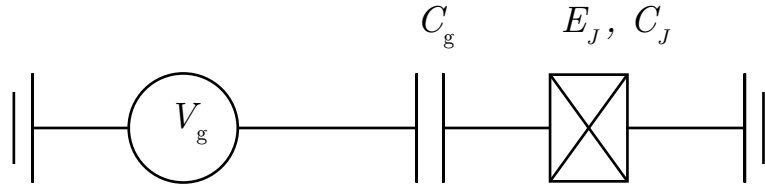


Figure 2.3: Circuit diagram of the Cooper pair box. Charges tunnel onto the island through the Josephson junction, represented by the crossed square.

for the additional capacitance. The total capacitance $C_{\Sigma} = C_g + C_J$ is the sum of the gate and Josephson junction capacitances. Together with the Josephson energy of Eq. (2.4), we obtain a circuit Hamiltonian

$$\hat{H} = 4E_C (\hat{n} - n_g)^2 - E_J \cos \hat{\phi}. \quad (2.6)$$

The effective offset charge introduced by the gate bias V_g is $n_g = C_{\Sigma}V_g/2e$. Using the quantum commutation relation $[\hat{n}, \hat{\phi}] = i$, it is possible to express this Hamiltonian in the charge basis as [11]

$$\hat{H} = 4E_C (\hat{n} - n_g)^2 - \frac{E_J}{2} \sum_n |n+1\rangle \langle n| + |n+1\rangle \langle n| \quad (2.7)$$

For qubit operations, the CPB is typically biased at the "sweet spot" $n_g = 1/2$, where the charging energy degeneracy of the $n = 0$ and $n = 1$ states is only broken by the Josephson energy. There are two distinct advantages with this regime. As the charging energy is typically dominant, $E_C \gg E_J$, the higher charge energy levels will be far away, so that a two-level approximation will be valid for the system in this case. In addition, this bias point provides reduced sensitivity to charge noise fluctuations, an important cause of decoherence.

2.2.2 The transmon qubit

The transmon is a qubit design similar to the Cooper pair box. It differs in that a shunt capacitance is added between the gate and the island (cf. Fig. 2.4). By increasing the capacitance of the island, this lowers the charging energy $E_C = e^2/2C$, leading to an increased E_J/E_C ratio. A higher E_J/E_C leads to a more harmonic energy spectrum, and also flattens the charge dispersion. By charge dispersion we mean the relationship between the qubit eigenenergies and offset charge n_g . A steep charge dispersion implies the energies change rapidly with n_g , and vice versa. While a certain anharmonicity is required for the two-level approximation of the qubit to remain valid, a flattened charge dispersion can significantly mitigate the problem of charge noise dephasing. A critical property to the operation of the transmon is the fact that as E_J/E_C is increased, the charge dispersion is exponentially suppressed, the anharmonicity only reduces by a power law. The result is

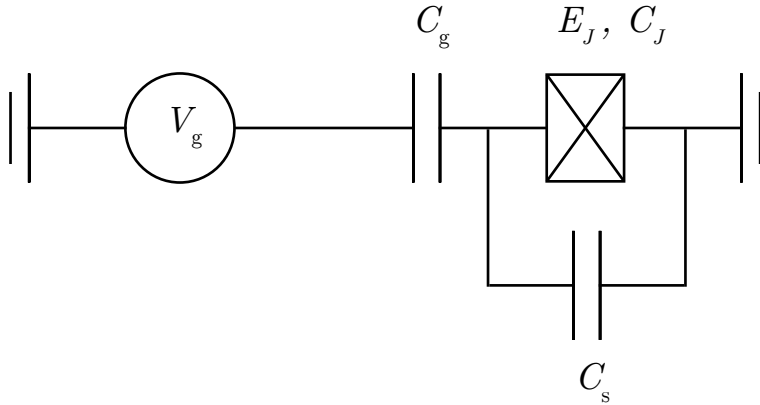


Figure 2.4: The transmon qubit equivalent circuit. Compared to the Cooper pair box, an extra capacitance has been added between the island and ground.

that the n_g -dependence of the energy levels may be practically eliminated, while retaining sufficient anharmonicity for qubit operation. The eigenenergies of the four lowest qubit levels are plotted for different values of E_J/E_C in Fig. 2.5. The energy eigenvalues were obtained using the QuTiP library [12].

Applying second order perturbation theory to find the transmon energies gives for the first two transitions gives [3]

$$E_{01} = \sqrt{8E_C E_J} - E_C \quad (2.8)$$

$$E_{12} = \sqrt{8E_C E_J} - 2E_C \quad (2.9)$$

where E_{01} and E_{12} are the energies of the first and second transitions, respectively. They are related to the corresponding transition frequencies f_{ij} by Planck's constant, $E_{ij} = \hbar f_{ij}$. Transmon qubits are typically designed to operate in the $E_J/E_C \sim 50$ regime. We then get an approximate relative anharmonicity

$$A_{rel} \equiv \frac{E_{01} - E_{12}}{E_{01}} = \sqrt{\frac{E_C}{8E_J}}. \quad (2.10)$$

Though commonly referred to as charge qubits, this term is not entirely consistent with the fact that the Josephson energy dominates over the charging energy in most applications. The flattened charge dispersion of the transmon has an important implication for qubit experiments besides the improved coherence lifetime. Since n_g is not a relevant tuning parameter any more, no bias circuitry is necessary to ensure functional operation. This makes the transmon suitable for applications where control circuits may be impractical to implement. Relevant for this thesis is the three-dimensional configuration enclosing the transmon in a superconducting cavity. Here, we let the shunt capacitance serve also as the antennas necessary for the interaction with the electric field. As seen in the schematic

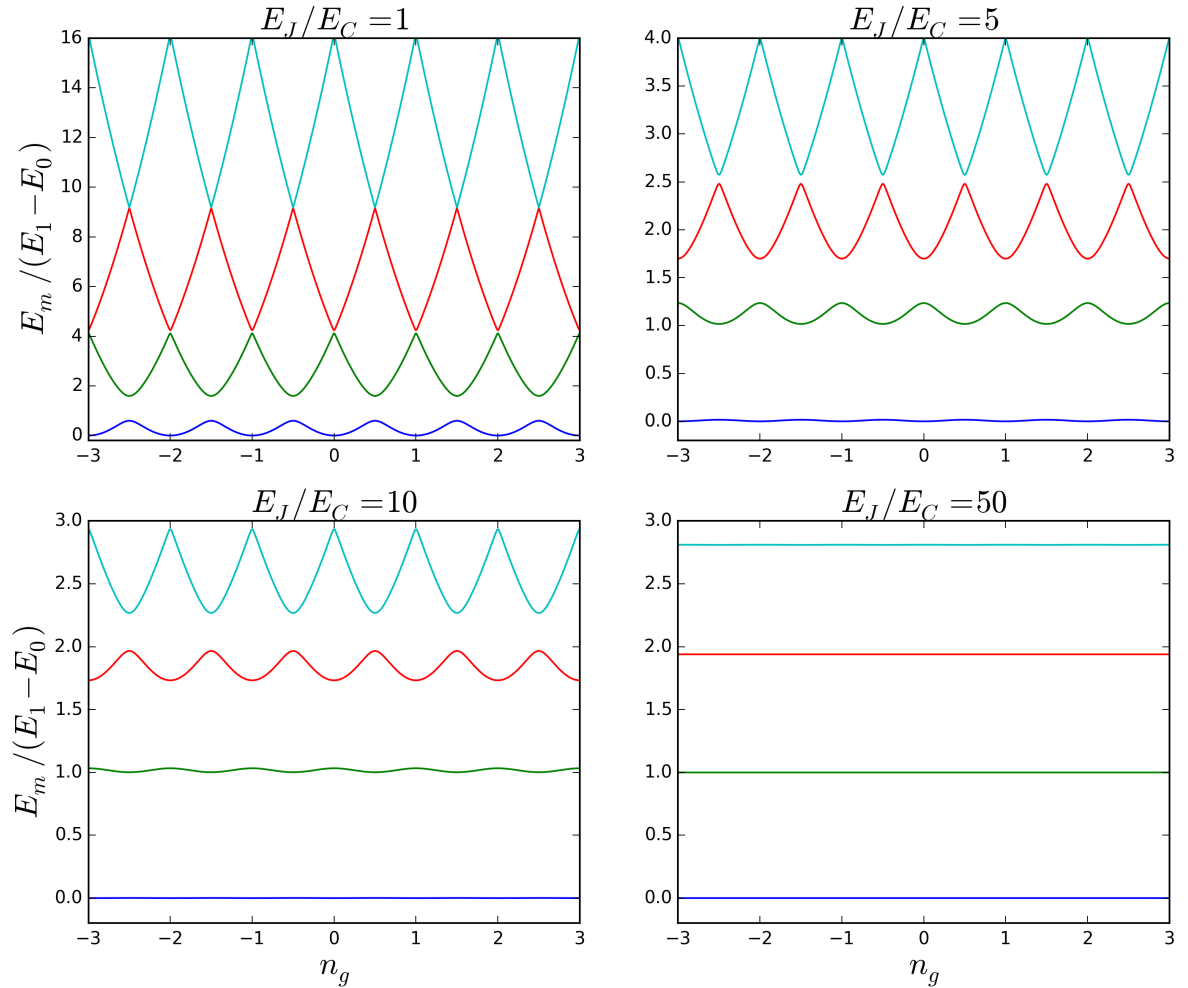


Figure 2.5: The first four energy levels of the charge qubit as a function of n_g , plotted for different values of E_J/E_C . The levels are eigenenergies of the Hamiltonian of Eq. (2.7).

presented in Fig. 2.6, this leads to a design less complex than the equivalent circuit diagram may suggest.

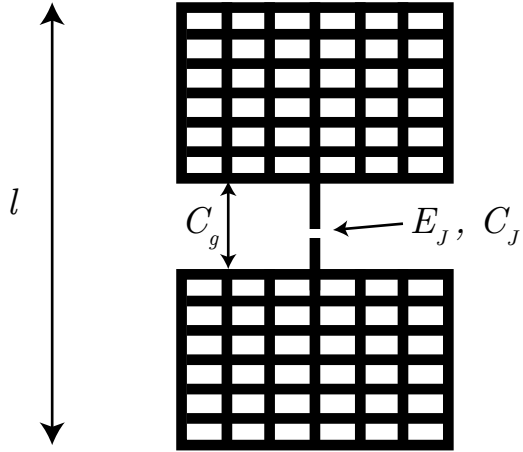


Figure 2.6: Schematic illustration of the 3D transmon design. The pad structures provide the shunt capacitance as well as the resonator coupling. The Josephson junction is marked with the junction energy E_J and junction capacitance C_J . The length of the qubit structure l influences the dipole moment of the structure, which is critical to the electric field coupling.

While the low charging energy of the transmon removes the relevance of a gate bias voltage, a modification enabling tuning of the Josephson energy may substantially expand the scope of possible experiments [13]. This is done by splitting the junction into two symmetric branches, effectively turning it into a loop with two Josephson junctions, commonly known as a superconducting quantum interference device (SQUID) [8]. Flux quantization requires the total flux penetrating the loop be an integer multiple of Φ_0 [8]. An important consequence is an effective change in E_J when an external flux is applied, as screening currents in the loop arise to compensate the bias flux and maintain flux quantization.

The circuit diagram of a tunable transmon is displayed in Fig. 2.7. The split junction has an effective combined capacitance and flux tunable Josephson energy.

2.3 Cavity resonators

A 3D cavity resonator is a vacuum volume enclosed in metal. The eigenmodes of the electromagnetic field in such structures have a dilute field strength and large vacuum participation with a minimum of lossy components inside the mode volume. As a result it is relatively easy to operate such cavities at a low photon loss rate. The damping of the resonator is described by the dimensionless quality factor, or Q-factor, defined as ratio of energy stored in the electromagnetic field to the loss per period of oscillation T , multiplied by a factor of 2π

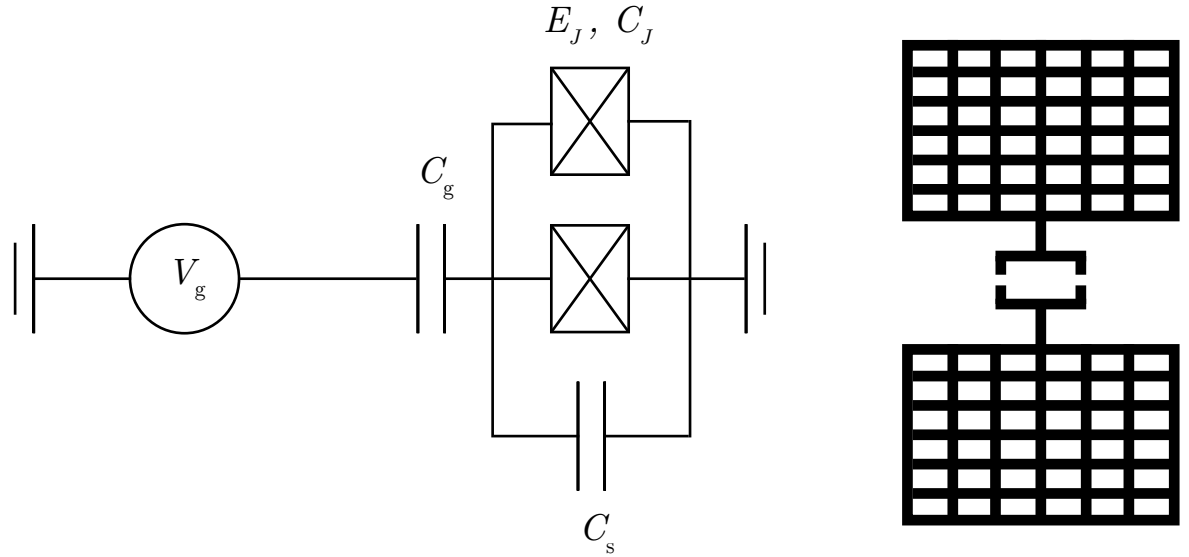


Figure 2.7: Equivalent circuit diagram and 3D schematic design of a tunable transmon. The effective Josephson energy is altered by coupling an external magnetic flux into the split junction loop.

$$Q = \frac{2\pi}{T} \frac{U}{P_d} = \frac{\omega U}{P_d}. \quad (2.11)$$

The stored energy is given by U . The power dissipation due to resonator losses is described by P_d and ω is the angular frequency of the oscillations. In the limit where $Q \gg 1$, the cavity transmission has a Lorentzian lineshape centered at the resonance frequency, with a linewidth determined by the loss rate κ . The Q-factor may then be expressed as

$$Q = \frac{\omega_r}{\kappa} = \frac{\omega_r}{\Delta\omega_r}. \quad (2.12)$$

The resonant bandwidth $\Delta\omega_r = \kappa$ is given by the full width at half maximum (FWHM) of the Lorentzian. This is illustrated in Fig. 2.8. The quality factor may be decomposed into the internal and external quality factors. The internal Q-factor Q_{int} describes internal losses in the metal surface or absorption from two-level systems inside the resonant volume. The external Q-factor Q_{ext} accounts for photons exiting the cavity through the input or output lines that couple the cavity to the environment, in this case the setup electronics. Equation (2.12) gives the total, or loaded quality factor. As the loss rates through different channels add up, and the Q-factor is reciprocal to loss, the total quality may be calculated as

$$\frac{1}{Q} = \frac{1}{Q_{\text{ext}}} + \frac{1}{Q_{\text{int}}}. \quad (2.13)$$

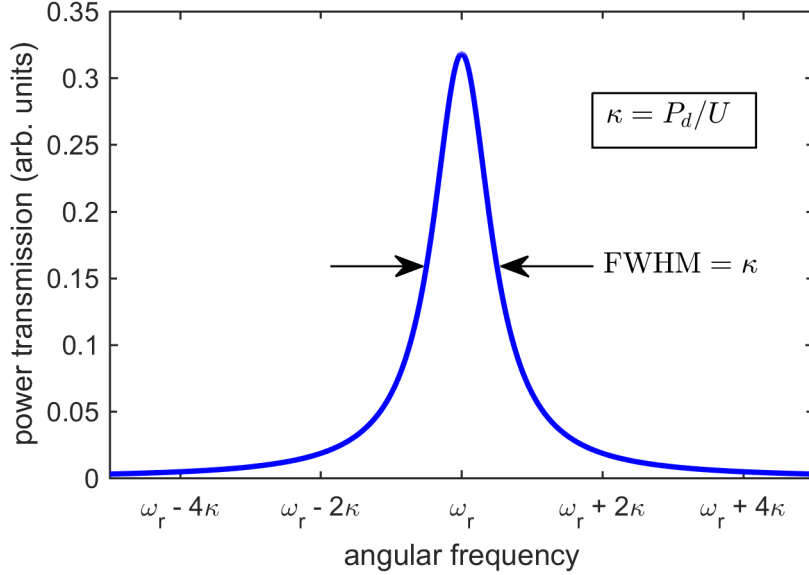


Figure 2.8: The resonator transmission lineshape is a Lorentzian. The bandwidth of the transmission is determined by the loss rate.

Internal loss

The cavity losses that yield the internal quality factor occur mainly in the conducting metal walls, and so depend on the surface resistivity of the material. The power dissipation in the walls is given by [14]

$$P_{\text{walls}} = \frac{R_s}{2} \int_{\text{walls}} |H_t|^2 ds. \quad (2.14)$$

The surface resistivity is denoted by R_s and H_t is the magnetic field tangential to the cavity surface. A common approach to achieve high Q-factors is the use of superconducting cavities, which have minimal surface resistivity. Much of the development towards low-loss resonators and other superconducting radio frequency applications has been done within accelerator physics, aiming at methods to efficiently accelerate charged particles. An expression for the surface resistivity can be formulated using BCS theory [15]

$$R_s = R_{\text{BCS}} + R_{\text{res}} \quad (2.15)$$

where R_{BCS} is the BCS surface resistivity, up to a prefactor given by

$$R_{\text{BCS}} \propto \frac{\omega^2}{T} e^{-1.76 T_c/T}. \quad (2.16)$$

Dissipation occurs due to oscillations in normal-component electrons induced by the penetration of the magnetic field into the metal. The density of electrons not bound in

Cooper pairs decreases exponentially with T_c/T , where T_c is the superconducting critical temperature. The other term in the total surface resistivity is the residual resistivity R_{res} . It is associated with surface imperfections, such as lattice distortions and defects, as well as trapped magnetic flux. The surface resistivity is independent of temperature, but surface treatment approaches such as electropolishing have been shown to reduce this component [16]. Apart from losses to the cavity walls, internal losses may arise from absorption due to two-level systems in dielectrics present within the mode volume, such as the qubit chip substrate.

Cavity modes

We seek to fit a transmon qubit inside an approximately rectangular cavity. The lowest electromagnetic field modes of such a cavity and the ones relevant for our qubit experiments are the TE_{10l} modes, $l = 1, 2$. In this context, TE stands for transverse electric, meaning the electric field is everywhere perpendicular to the direction of propagation. Letting the polarization define the y -axis gives $\mathbf{E} = E_y \mathbf{e}_y$. In a rectangular cavity resonator, the electric field of the TE_{10l} modes is then given by [14]

$$E_y = E_0 \sin\left(\frac{\pi x}{a}\right) \sin\left(\frac{l\pi z}{d}\right). \quad (2.17)$$

The first two modes are visualized in Fig. 2.9. The fundamental mode has an electric field anti-node in the cavity center and the length of the cavity corresponds to $\lambda/2$, meaning there is one standing wave antinode in the propagation direction. The second cavity mode has two standing wave antinodes along the length of the cavity d , does however not correspond to twice the frequency of the first mode.

Scattering parameters

The transmission and reflection amplitudes of signals coupled into the cavity are often described using scattering parameters, or S-parameters. Generally, S-parameters describe the propagation of electrical signals between ports in a network and are represented as a matrix [14]:

$$\begin{bmatrix} V_1^- \\ V_2^- \\ \vdots \\ V_n^- \end{bmatrix} = \begin{bmatrix} S_{11} & S_{12} & \cdots & S_{1n} \\ S_{21} & S_{22} & \cdots & S_{2n} \\ \vdots & \vdots & \ddots & \vdots \\ S_{N1} & S_{N2} & \cdots & S_{NN} \end{bmatrix} \begin{bmatrix} V_1^+ \\ V_2^+ \\ \vdots \\ V_n^+ \end{bmatrix} \quad (2.18)$$

The incident voltage signal at port i is given by V_i^+ and V_i^- represents the outgoing amplitude at the same port. The individual matrix elements S_{ij} may be determined by exciting port j while terminating all others except port i with no impedance mismatch.

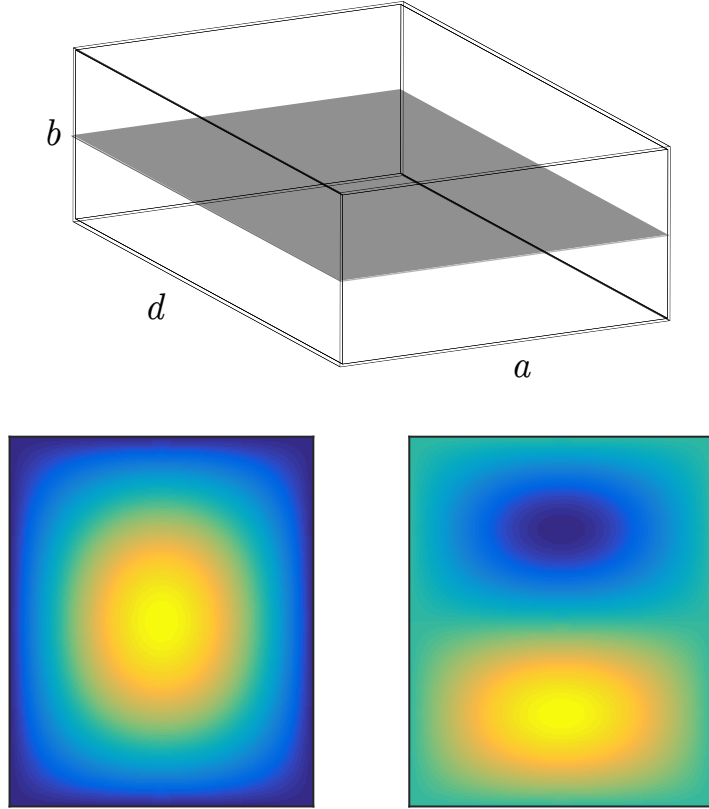


Figure 2.9: Schematic of a rectangular cavity resonator (top). Electric field distribution of the TE_{101} (bottom left) and TE_{102} (bottom right) modes on the schematic cutplane. The field is polarized perpendicular to the figure plane.

We may express this as

$$S_{ij} = \left. \frac{V_i^-}{V_j^+} \right|_{V_k^+=0, k \neq j}. \quad (2.19)$$

A network without active components, such as circulators or amplifiers, has a symmetric scattering matrix. Furthermore, if the S-matrix is non-unitary, this indicates internal losses are present in the network.

Cavities with one input and one output port may be regarded as a two-port network in scattering matrix analysis. From the S-parameters we can determine the quality factor and its internal and external components. The ratio of incident to transmitted power is given by $|S_{21}|^2$. Therefore $|S_{21}(\omega)|^2$ will describe a Lorentzian lineshape as plotted in Fig. 2.8, providing the resonator quality. The external and internal loss components may be determined by accounting for the amplitude reflected back at the input. For a two-port network they are related by [17]

$$Q_{\text{int}} = (1 + k_1 + k_2)Q. \quad (2.20)$$

The coupling coefficients k_i quantify the how strongly port i is coupled to the system environment. They are given by the scattering parameters at the resonance frequency f_r :

$$k_i = \frac{|S_{21}(f_r)|^2}{1 - |S_{ii}(f_r)|^2 - |S_{21}(f_r)|^2}. \quad (2.21)$$

Measuring the magnitudes of the reflected and transmitted signals of a two-port cavity will thus enable characterization in terms of internal and external quality, as well as the coupling coefficients. Assuming the cavity is connected to the environment in a symmetric fashion ($k_1 = k_2$), it is sufficient to record the scattering amplitudes $|S_{21}|$ and $|S_{11}|$.

2.4 Cavity QED and 3D circuit QED

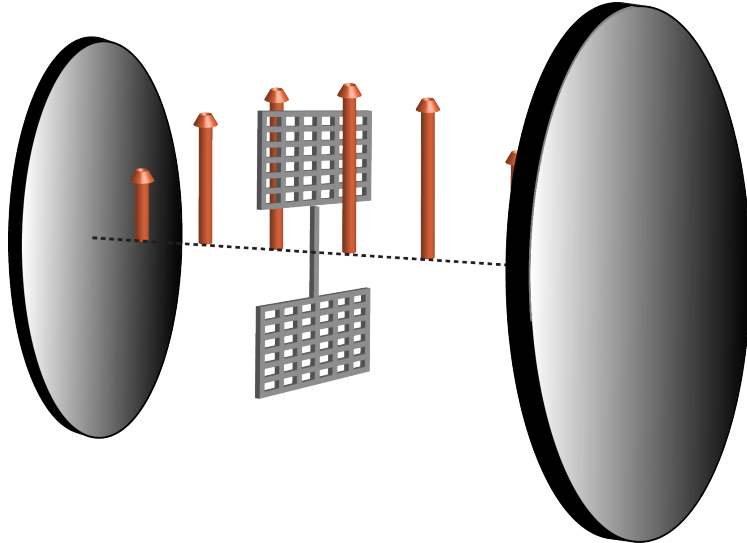


Figure 2.10: 3D cQED schematic

We are now ready to examine the combined system of qubit and resonator. The theory describing the interaction between a two-level system and a quantized electromagnetic field was first developed in the context of cavity quantum electrodynamics (cavity QED) [18]. Rather than artificial qubits, cavity QED involves atoms coupled to light fields in optical cavities, a research field that notably lead to the 2012 Nobel Prize in physics being awarded to Serge Haroche and David Wineland [19]. Starting out with a discussion of the fundamental model of this interaction, the Jaynes-Cummings model, we then apply this formalism to the transmon. Finally, we describe in greater detail the physics behind the coupling of the transmon to the microwave field. Figure 2.10 shows a schematic drawing of the interaction involved in this 3D circuit QED picture, with a transmon qubit polarized by an electric field confined between two mirrors.

2.4.1 Jaynes-Cummings model

The quantum mechanical interaction between a two-level atom and a single resonant cavity mode gives rise to the well known Jaynes-Cummings Hamiltonian. As two-level systems are generally described using Pauli matrices, the atomic state enters the Hamiltonian as $\hat{H}_a = (\hbar\omega_a/2) \hat{\sigma}_z$. The resonator mode is described by a quantum harmonic oscillator and appears as $\hat{H}_r = \hbar(\hat{a}^\dagger \hat{a} + 1/2)$. The non-trivial dynamics of the system arise due to a third term in the Hamiltonian, accounting for the coupling of the atomic dipole moment of the atom and the cavity electric field. The electric field operator corresponds to the position operator of the harmonic oscillator. Ignoring quickly oscillating terms, this gives $\hat{H}_{\text{int}} = \hbar g (\hat{a}\hat{\sigma}^+ + \hat{a}^\dagger\hat{\sigma}^-)$, where $\hat{\sigma}^+$ ($\hat{\sigma}^-$) is the raising (lowering) operator for the atomic state. The strength of the interaction is given by the parameter g , the coupling strength, which provides a characteristic angular frequency for the exchange of energy between atom and cavity. We will find reason to return to this important quantity below. For $g \ll \omega_q, \omega_r$ and ignoring any losses or decoherence, we obtain

$$\hat{H} = \frac{\hbar\omega_a}{2} \hat{\sigma}_z + \hbar\omega_r \left(\hat{a}^\dagger \hat{a} + \frac{1}{2} \right) + \hbar g (\hat{a}\hat{\sigma}^+ + \hat{a}^\dagger\hat{\sigma}^-). \quad (2.22)$$

In 3D circuit QED, a qubit placed inside a cavity resonator is substituted for the atom, but the dynamics of the system still obey Eq. (2.22). For the transmon qubit however, the low anharmonicity may require taking higher qubit levels into account in certain parameter ranges.

For the Jaynes-Cummings Hamiltonian to describe well the time evolution of a 3D circuit QED system, it is necessary to reach the strong coupling limit, where the coupling strength is larger than the qubit decay and cavity loss rates ($g > \kappa, \Gamma_1, \Gamma_2$). Otherwise, the non-Hermitian interaction with the environment will dominate the system dynamics.

2.4.2 Dispersively coupled transmon

The time evolution generated by Eq. (2.22) differs considerably depending on whether the qubit frequency is near the cavity resonance. If the magnitude of the detuning $\Delta \equiv \omega_q - \omega_r$ is smaller than the coupling strength, the first excited state of the system will see energy being coherently transferred back and forth between qubit and resonator. Thus, neither a ground state qubit with a single cavity photon, nor an excited state qubit in an empty cavity are eigenstates of the system. The system investigated below (cf. Sec. 4.2) couples the cavity to a qubit whose first transition frequency is far detuned from the fundamental mode. This parameter range, where $\Delta \gg g$, is known as the dispersive regime. The large detuning inhibits the exchange of energy between qubit and resonator, resulting in eigenstates close to their bare parameters. Figure 2.11 shows how the state of an initially excited qubit evolves depending on the detuning in an ideal picture without decay or resonator losses. For an open system, with losses and decoherence induced by

the environment, the time evolution of mixed states is described using density matrix formalism [20], incorporating Lindblad operators for the decay [21]. For a review of the dynamics of such systems, see Ref [22].

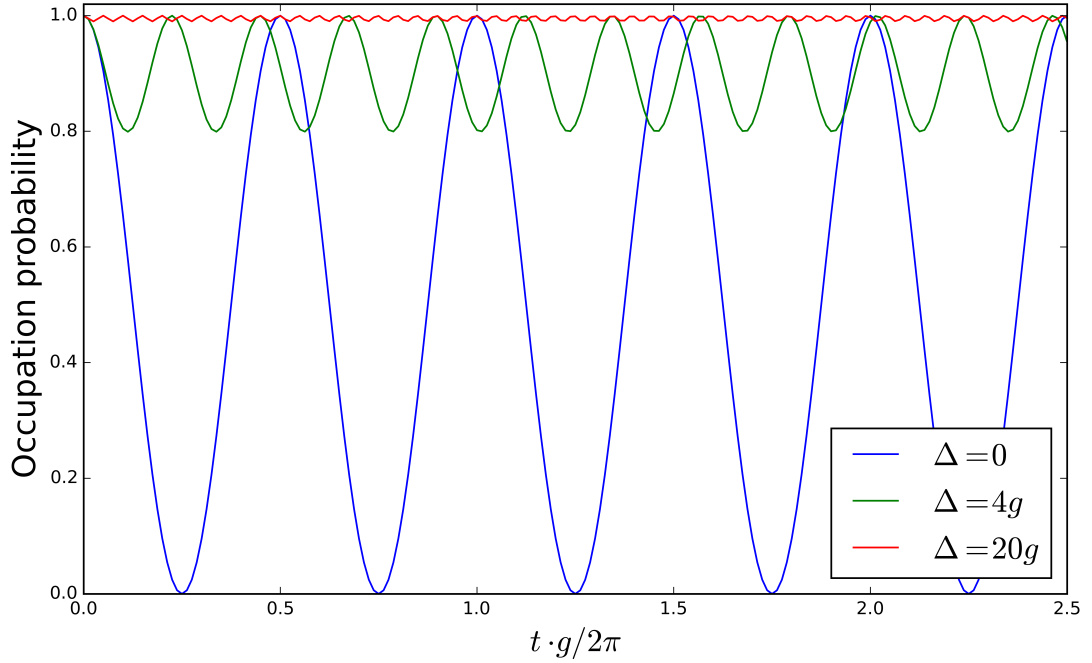


Figure 2.11: Time evolution of the qubit excited state occupation in the Jaynes-Cummings model for different values of the detuning simulated using QuTiP. The resonant case leads to the entire excitation energy oscillating between qubit and cavity. In the detuned limit, the exchange of energy is blocked almost completely.

In the dispersive limit, a unitary transformation may be applied to eliminate the coupling. The deviations from the bare, uncoupled qubit and resonator parameters can then be obtained from perturbation theory. In the two-level approximation this yields an effective Hamiltonian [23]

$$\hat{H}_{\text{eff}} = \hbar \left(\omega_r + \frac{g^2}{\Delta} \hat{\sigma}_z \right) \hat{a}^\dagger \hat{a} + \frac{\hbar}{2} \left(\omega_q + \frac{g^2}{\Delta} \right) \hat{\sigma}_z. \quad (2.23)$$

We note how the cavity field deviates from the bare resonator by the qubit state dependent shift of $\pm g^2/\Delta$. Known as the dispersive shift, this allows readout of the qubit state via the cavity. Grouping together terms in Eq. (2.23) acting on the qubit state, we obtain the qubit frequency in the composite system as

$$\omega_{01} = \omega_q + 2 \frac{g^2}{\Delta} \left(\hat{a}^\dagger \hat{a} + \frac{1}{2} \right). \quad (2.24)$$

Qubit and resonator states and frequencies in the combined system are often referred to as the *dressed* state frequencies. This is a way to distinguish the composite eigenstates from the parameters of the isolated qubit and cavity.

For the transmon in the dispersive regime, the moderate anharmonicity may lead to higher qubit transitions affecting the dispersive shift of the cavity. In second order perturbation theory, the second transmon level also appears in the Hamiltonian. The result is a reduced dispersive shift and the effective Hamiltonian

$$\hat{H}_{\text{eff}} = \hbar \left(\omega_r - \frac{\chi_{12}}{2} + \chi \hat{\sigma}_z \right) \hat{a}^\dagger \hat{a} + \frac{\hbar}{2} (\omega_q + \chi_{01}) \hat{\sigma}_z. \quad (2.25)$$

We introduced here the interaction parameters

$$\chi = \chi_{01} - \chi_{12}/2 \quad (2.26)$$

$$\chi_{ij} = \frac{g^2}{\Delta_i} \quad (2.27)$$

where $\Delta_i \equiv \omega_{i-1,1} - \omega_r$ is the detuning between the i th transition and the resonator. Combining these expressions, the coupling strength can be determined from a recorded dispersive shift as

$$g = \left(\frac{\chi}{\frac{1}{\Delta_1} - \frac{1}{2\Delta_2}} \right)^{1/2}. \quad (2.28)$$

This relation allows for measurement of g via the cavity in a photon number independent way. It is therefore highly useful for determining the coupling strength and calibrating the photon number population of the cavity.

Since, as illustrated in Fig. 2.11, the qubit-resonator detuning prevents the qubit from decay by emitting a photon into the cavity mode, it is reasonable to expect an effect on the characteristic decay time T_1 . By Fermi's golden rule, the rate of spontaneous emission of an excited state, the vacuum rate of photon emission decay, is given by [24]

$$\Gamma = 2\pi g(\omega)^2 D(\omega). \quad (2.29)$$

This rate depends on the final photon density of states D . Whereas in free space, the volume normalized density of states writes

$$D(\omega) = \frac{\omega^2}{\pi^2 c^3}, \quad (2.30)$$

the cavity Lorentzian filtering leads to an approximate expression for high Q resonators

$$D(\omega) = \frac{1}{\pi} \frac{\kappa/2}{(\omega - \omega_r)^2 + (\kappa/2)^2}. \quad (2.31)$$

This leads to a strong modulation of the decay rate due to the cavity impact on the photon density of states. For a qubit resonant with the cavity, the decay rate equals g in the strong coupling limit, much larger than the free space decay rate Γ_{free} . For qubits or atoms resonantly coupled to a cavity, the parameter g determines the rate of exchange of energy between them. This is one of the reasons why resonators are important to the study of light-matter interaction.

In the far detuned limit the decay rate is instead suppressed by the Lorentzian filtering of the cavity. Compared to the free space value, it is reduced by a factor depending on Q as well as a geometry factor.

$$\Gamma = \Gamma_{\text{free}} \frac{3}{16\pi^2 Q} \frac{\lambda^3}{V} \quad (2.32)$$

This coefficient is known as the Purcell factor and the associated effect is called the Purcell effect, after their discoverer E.M. Purcell [25]. A consequence of the Purcell effect is that high quality resonators can be used to increase coherence times. This entails a compromise with respect to measurement, as a high total Q requires the coupling of the cavity to the measurement setup to be weak. High internal quality is however always preferable. Since reaching high Q_{int} is typically easier with 3D cavities than planar structures, the longest qubit coherence times have been recorded in such configurations.

It is clear that the system dynamics differ substantially depending on the cavity-qubit detuning. With a split junction transmon as outlined in Fig. 2.7 and a some means of applying external magnetic flux through the loop, it is possible to tune the experiment continuously and in situ between the dispersive and resonant limits.

2.4.3 The coupling strength

In the Jaynes-Cummings model, the electric field couples to the dipole moment of the atom. The characteristic coupling strength per photon g is given by

$$g = \frac{\mu E_{\text{rms}}}{\hbar} \quad (2.33)$$

where μ is the expectation value of the dipole moment operator $-e\mathbf{r}$ applied to the atomic state and E_{rms} the root mean square of the vacuum electric field.

For the 3D transmon, μ is given by the dipole moment of the qubit structure where the Cooper pair charge $2e$ has been displaced from one pad to the other [26]. This dipole moment couples to the y-component of the vacuum RMS electric field of the first cavity mode at the qubit position. With electromagnetic FEM computations, we are able to compute these quantities and provide an a priori estimate for the coupling strength.

The vacuum electric field fluctuations for a single mode is given by [27]

$$E_{\text{rms}} = \sqrt{\frac{\hbar\omega}{2\epsilon_0 V}}. \quad (2.34)$$

Taking V to be the cavity volume would imply the assumption that the field is evenly distributed inside the cavity. A more rigorous consideration takes into account the field distribution of the fundamental cavity mode and relates it to the field at the qubit position. Instead of the cavity volume, we calculate the *mode volume* of the first resonant cavity mode, which we define as

$$V_{\text{mode}} = \frac{\int_V \epsilon(\mathbf{r}) \mathbf{E}^2(\mathbf{r}) d^3r}{\epsilon(\mathbf{r}_q) \mathbf{E}^2(\mathbf{r}_q)}. \quad (2.35)$$

Here, \mathbf{r}_q refers to the qubit position inside the cavity. As the transmon is small compared to the fundamental mode wavelength, its dimensions may be disregarded for this analysis. For a rectangular cavity with homogeneous dielectric constant and side lengths a, b and d , integrating the analytical expression for the TE₁₀₁ mode gives $V_{\text{mode}}/(abd) = 1/4$. An approach to refine this figure would be to use a numerical simulation more accurately representing the experimental design. Obtaining the electrodynamic parameters μ and V_{mode} in this manner, we may obtain an estimate of the coupling strength from

$$g = \mu \sqrt{\frac{\omega}{2\hbar\epsilon_0 V_{\text{mode}}}}. \quad (2.36)$$

In cavity QED with atoms, coupling strengths rarely exceed $g/2\pi = 20$ MHz. As it has a much larger dipole moment, the transmon couples much more strongly to the electric field. For transmons coupled to 3D cavities, couplings $g/2\pi > 100$ MHz have been observed. With typical decay rates $\Gamma_1/2\pi$ on the order of 1MHz, 3D transmon configurations are usually not difficult to operate in the strong coupling regime.

Chapter 3

Experimental methods and simulations

In this chapter we present and outline the methods used for characterizing the aluminium cavities and acquiring qubit data. We also describe the complementary numerical techniques and present simulation results.

3.1 Aluminium cavities

The project involves two waveguide cavity resonators of the same internal dimensions, fabricated by the in-house workshop. The cavities are volumes of space enclosed by metal, with a pair of SMA pin connectors to couple microwave signals in and out. The first cavity is machined from an aluminium alloy material, EN AW-2007, with an aluminium content of 88 % - 93 %. The impurities consist mainly of copper (3.3 % - 4.6 %), manganese ($\leq 1.8 \%$), and lead ($\leq 1.5 \%$). The second cavity has an aluminium purity greater than 99.99 %. Pure aluminium has higher thermal and electrical conductivity than the alloy. It is, however, soft and ductile and may more easily sustain damage to the surface or to screw windings. The aluminium based alloy is robust and also considerably less expensive. The cavities are milled from two pieces each, enclosed using pins and screws. The symmetry of the cavity design means the two parts are identical. We will call the EN AW-2007 sample the alloy cavity, while referring to the other resonator as the pure aluminium cavity. A drawing of the pure aluminium cavity is shown in Fig. 3.1. The internal dimensions of the resonant volume are shown in Fig. 3.2.

The input of microwave signals into the cavities and the output signal coupling occur via antenna pins. These penetrate into the cavity volume through circular, 2.1 mm diameter holes drilled through the top metal wall. We use Huber and Suhner Type 23 SMA connectors, whose pin ends introduce the electromagnetic excitation into the resonator volume. These connect to microwave experiment equipment via female SMA connectors, a standard interface in rf and microwave applications.

The coupling of the cavity to the environment can be controlled by varying the insertion depth of the connector pins into the resonant volume. Using combinations of spacers to mount the connectors, we are able to rigidly fix the pins in the desired configuration. The spacers are metal pieces with drilled holes through which the connectors fit. Their length

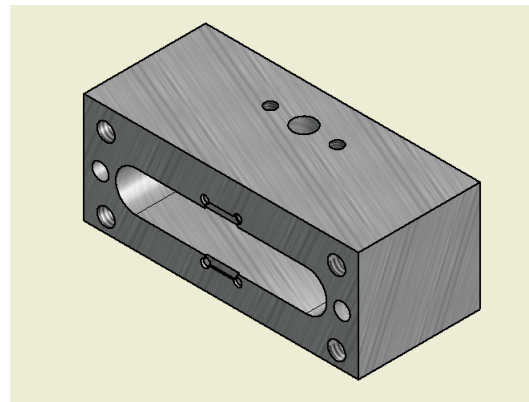


Figure 3.1: CAD generated drawing of the pure aluminium cavity. The alloy cavity has identical internal dimensions, but differs in that the top and bottom metal hull is thicker

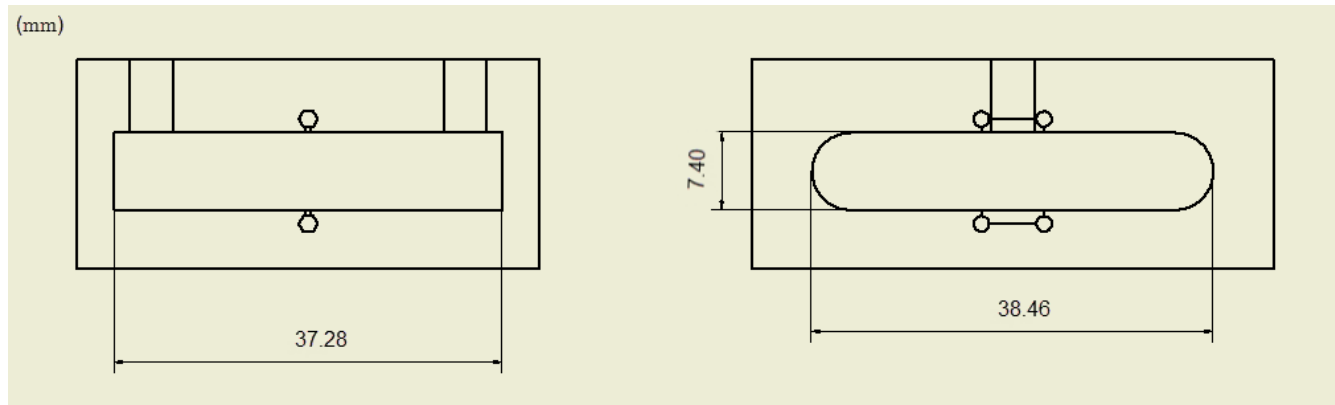


Figure 3.2: Profile drawings showing the internal dimensions of the cavities.



Figure 3.3: Photographs showing the pure aluminium cavity (left) as well as a pin connector along with samples of the spacers used to adjust the pin insertion depth (right). The numbers on the spacers indicate their height in mm.

determine the penetration distance of the pin into the cavity. By a pin depth of 0 mm we denote the case where the bottom of the pins are level with the surface of the cavity. A negative pin depth means further retraction, the end point of the pin is then inside the opening in the cavity wall. Examples of the spacers and connectors used are shown in Fig. 3.3.

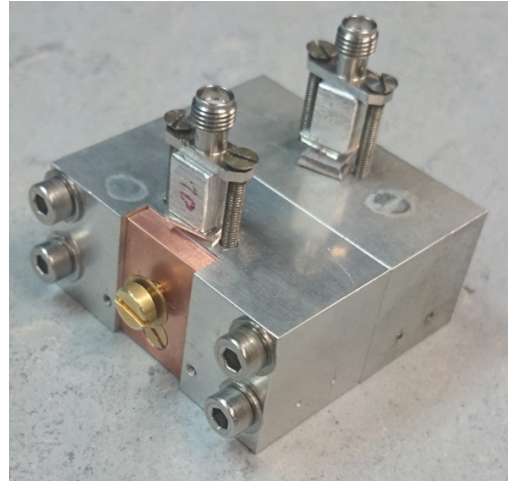


Figure 3.4: The alloy cavity following modifications introducing a magnetically permeable copper face as well as a tuning screw.

The alloy cavity is further modified to accommodate tuning of the resonant frequency as well as magnetic field penetrations (cf. Fig. 3.4). One section is milled open and replaced with a copper plate. Not being a superconductor, this face is permeable by magnetic fields at cryogenic temperatures, opening up the possibility of flux bias tuning of qubit parameters. A shape perturbation tuning the resonance frequency of the cavity may be introduced in the form of a metallic screw through the copper plate.

3.1.1 Room temperature setup

The first step towards cavity characterization is to measure the S-parameters at room temperature, and compare to simulations. The resonance frequency and quality factor are determined by fitting a Lorentzian to the transmitted power $|S_{21}|^2$. For measuring the S-parameters, we use Rohde & Schwarz ZVA and ZVB Series vector network analysers (VNA). An essential instrument for microwave engineering, network analysers generate, receive and measure electric signals in the radiofrequency and microwave regime. Unlike scalar analysers, which only measure amplitude properties of the signals, a VNA also provides the relative phase of the generated and received signals.

In the room temperature cavity measurement setup, each cavity port is connected via SMA cables to a port of the VNA. In this configuration, we measure the S-parameters of the resulting network. The instrument is calibrated to account for losses in the microwave

cables. The data acquisition is controlled via a computer, using the measurement and control software NI LabView [28].

3.1.2 Cryogenic setup

As qubit experiments are carried out at cryogenic temperatures, it is necessary to determine the properties of our 3D cavities under these conditions. In order to reach temperatures relevant to qubit operations, on the order of 50 mK, we use a dry He³-He⁴ dilution refrigerator setup. The dilution refrigerator, pictured in Fig. 3.5, cools the sample stage using the heat of mixing He³ with superfluid He⁴. In a strongly simplified picture, the operation principle can be pictured as analogous to standard compressor refrigerators. Instead of the evaporation of a refrigerant, the corresponding phase change involves high concentration He³ "expanding" into a background of inert He⁴. The enthalpy of crossing this boundary between the concentrated and dilute phases (referring to He³ density) results in heat removal from the sample. Dilution refrigerators have been in operation at the WMI for several decades, and our experiments are carried out in the latest installed unit, a cryogen free refrigerator built in-house to accommodate bulky microwave components at all temperature stages. The sample stage bottom plate (cf. Fig. 3.6) has a diameter of 30 cm and the sample space extends vertically approximately 40 cm. The cavities are suspended from the bottom plate using annealed silver wire, which secures the cavity mechanically and provides good thermal contact.

The setup, outlined in Fig. 3.7, has an input and output line for each cavity. The input lines is fitted with attenuators at all cryostat temperature stages, to reduce the effect of thermal noise propagating down to the 30 mK sample stage. On the output side of the cavities, this is accomplished using passive cryogenic circulators. The output signal is amplified at low temperature by cryogenic high electron mobility transistor (HEMT) amplifiers, as well as by an additional amplifier at room temperature. The HEMT amplifiers have an estimated gain slightly below 45 dB in our frequency range, while the room temperature amplification amounts to approximately 28 dB. The noise temperature of the amplification chain is limited by that of the HEMTs to approximately 40 K. Via a pair of switches, either measurement line can be redirected to bypass the cavity, passing instead through a short (20 cm) Minibend™ cable. This scheme provides a straightforward way of calibrating the measurement lines, allowing us to account for the total effect of losses and amplification on the signal amplitude when analysing the acquired data. A thermometer is fitted in direct contact with the cavity in order to enable us to ensure thermalization. High power transmitted to the sample stage, for instance to change the state of the cryogenic switches, may lead to significant heating. With a thermal sensor anchored to the cavity, we observe clearly when it returns to a steady temperature state. A photograph of the two cavities and switches with calibration line is shown in Fig. 3.6.

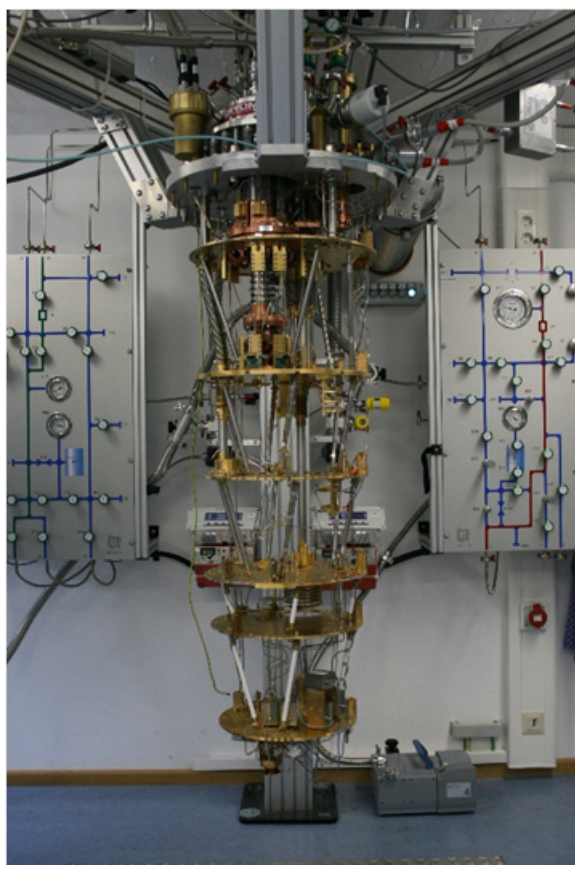


Figure 3.5: The cryogen-free dilution refrigerator used for low-temperature experiments.

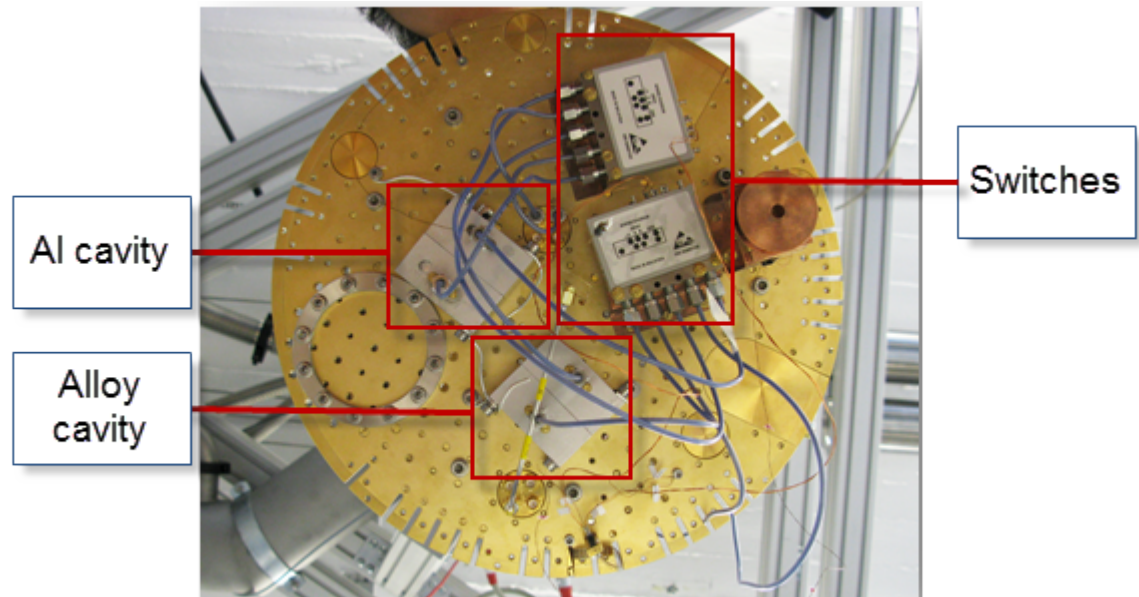


Figure 3.6: Bottom view of the cryostat mixing chamber plate. Both cavities are mounted at the sample stage and connected to the microwave switches.

Data analysis and plotting is carried out using Matlab. The cavity parameters are extracted by Lorentzian fitting to the transmission data.

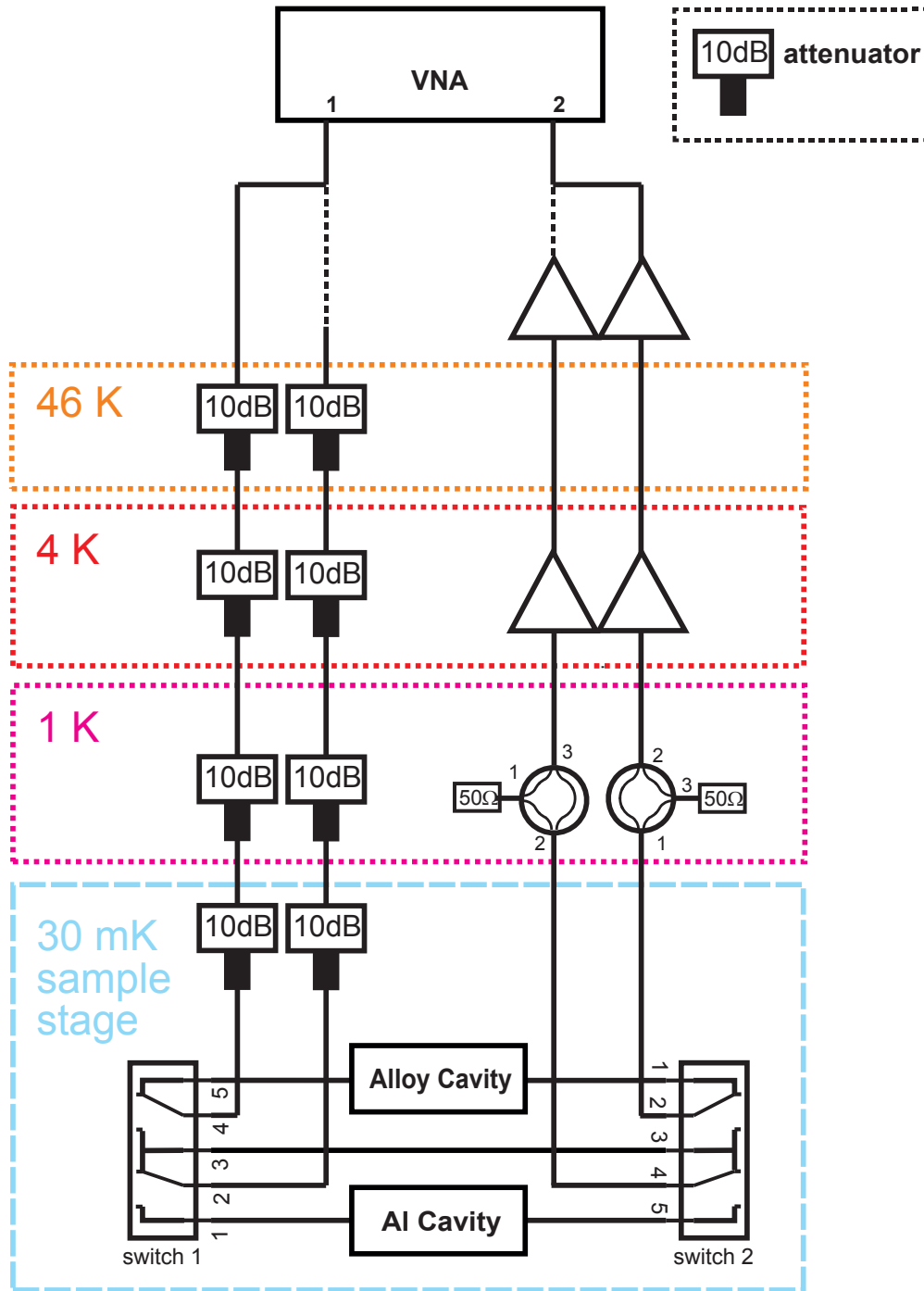


Figure 3.7: Circuit diagram of the cryogenic setup used to measure transmission of both the alloy and pure aluminium cavities. The coloured boxes indicate temperature stages of the cryostat.

3.2 Qubit spectroscopy

We perform qubit spectroscopy of a transmon fitted inside the pure aluminium cavity. Similarly as for the low-temperature cavity characterization, these experiments are carried out in a dilution refrigerator at millikelvin temperatures. In this section, we briefly describe the transmon sample. Then we outline the spectroscopy setup and procedure used to perform qubit measurements.

3.2.1 3D Transmon

The transmon consists of a single Josephson junction with antenna pads on either side (cf. Fig. 2.6). The pads and junction electrodes are made from aluminium and the tunnel barrier is provided by an aluminium oxide. The pads, which also provide the shunt capacitance, are $750\text{ }\mu\text{m}$ wide and $350\text{ }\mu\text{m}$ long. Although aluminium, as a type I superconductor, should expel any magnetic field penetration when cooled below T_c , thin films such as the transmon pads have been shown to support magnetic flux vortices. As vortex motion may lead to flux noise dephasing of the qubit, we attempt to fabricate the pads in a grid structure, with rectangular holes. The resulting superconductor boundaries provide a trapping potential pinning the vortices, preventing their motion across the sample. The structure is patterned with electron beam lithography and evaporated onto

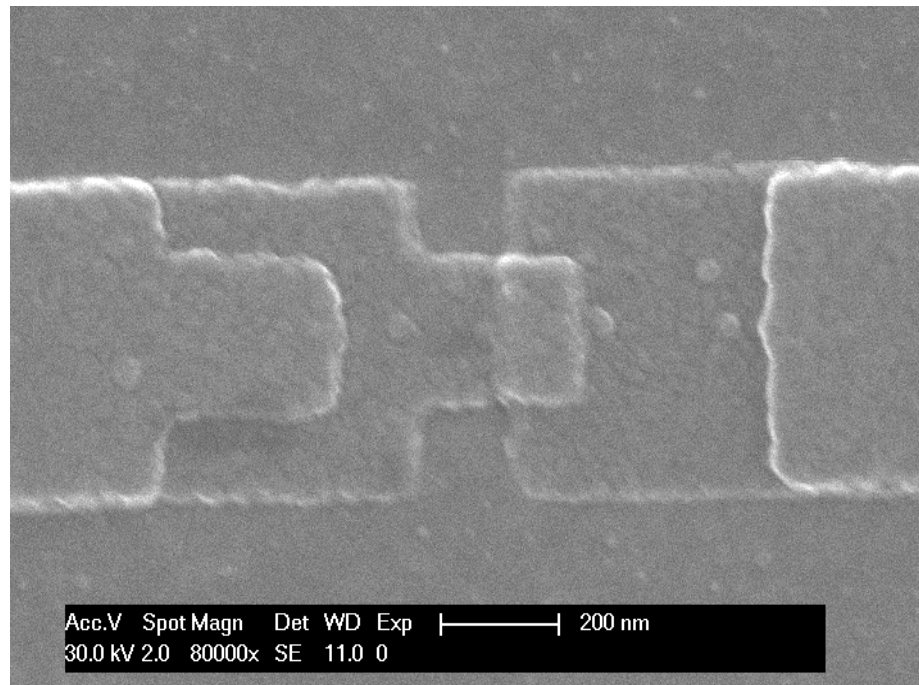


Figure 3.8: SEM micrograph of a Josephson junction, as schematically represented in Fig. 2.1.

a 10 mm by 6 mm silicon wafer using a shadow angle evaporation technique [29]. These processes are standard procedure at the WMI [30]. A scanning electron microscopy (SEM)

image of a junction fabricated with this process is shown in Fig. 3.8. Figure 3.9 shows an image of the transmon sample used in two-tone spectroscopy taken with an optical microscope. In this figure it is clear that the aluminium is not completely removed from the grid holes. The structure pattern may however still create flux pinning potentials.

The chip with the transmon is then mounted vertically in the center of the cavity, where it fits into a milled slit structure. Figure 3.10 shows the mounted chip in the pure aluminium cavity. Additional pieces of indium are used to ensure sufficient thermal coupling to the aluminium. This configuration leads to strong coupling between the fundamental mode of the resonator and the qubit, as the qubit is located in the antinode of the electric field with the antennas extending in the plane of electric polarization.



Figure 3.9: Microscopy image of the transmon sample. The junction is in the center line between the pads, which are 50 μm apart. The gridded pads have 20 μm by 20 μm cells and the bars are 5 μm wide. During fabrication, the aluminium has not been removed entirely from the grid cells. The blue bar near the bottom is a 100 μm length scale reference.

3.2.2 Two-tone spectroscopy setup

We now turn to the details of the spectroscopy setup used to perform measurements of the qubit. The pure aluminium cavity is again attached to the bottom plate of the fridge using silver wire for thermal contact. Compared to the bare cavity measurements at millikelvin temperatures, the cryogenic part of the setup is changed to include extra

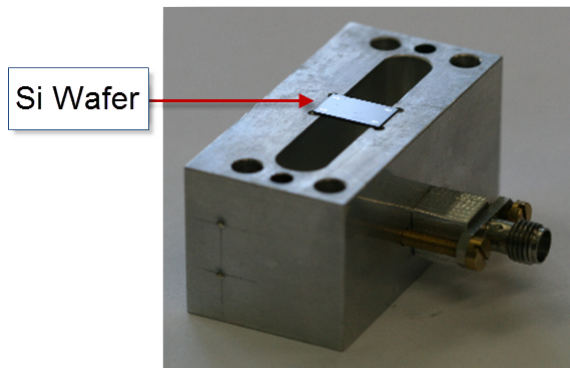


Figure 3.10: Alloy cavity with a silicon wafer mounted. At cryogenic temperatures, thermal and mechanical coupling is ensured by adding Indium to the spherical corners of the milled chip frame.

attenuation at the input of the cavity. This is in order to shield the qubit from thermal photons generated at the higher temperature stages. The pin insertion depth of the cavity is also changed, from -1.6 mm to 1.4 mm . This reflects the priority of detecting the qubit effect on the cavity, as a higher port coupling coefficient facilitates the introduction of off-resonant qubit drive signals. Other changes made to the cryogenic part of the setup are only made in order to accommodate parallel experiments unrelated to this thesis. The cavities have thick superconducting bulk metal walls that allow no magnetic field penetration. Therefore, no additional magnetic shielding is required to protect the qubit from flux noise.

The room temperature part of the setup is altered more substantially to incorporate simultaneous driving and cavity readout. In two-tone spectroscopy, we use two simultane-

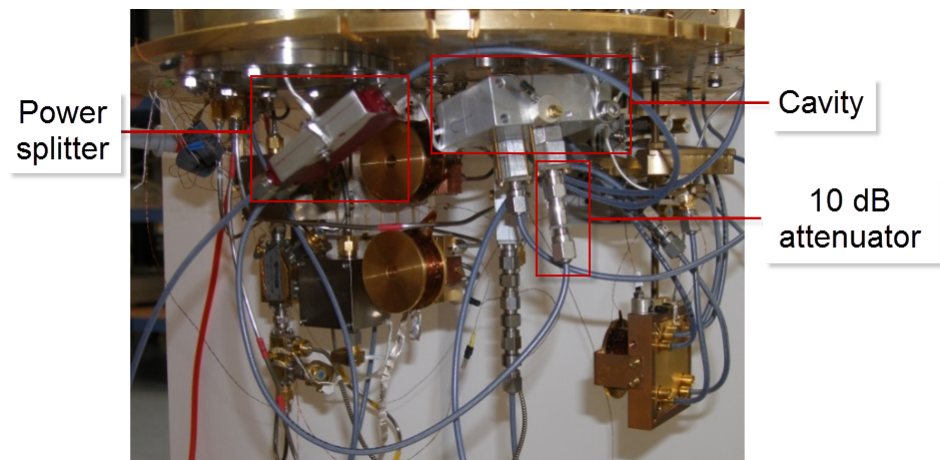


Figure 3.11: The pure aluminium cavity mounted at the sample stage for qubit spectroscopy. The power splitter in the foreground enables sharing an input line with another experiment.

ous microwave signals to find the frequency of the first qubit transition. This is done by feeding a weak readout tone, also referred to as the probe tone, at the resonance frequency

of the cavity, while sweeping the frequency of the second tone, the drive, close to the estimated transmon frequency. If sufficiently close to the qubit frequency, the drive tone will drive the qubit out of the ground state and into an incoherent mixed state. Due to the dispersive shift, this is then observed as a dip in the magnitude and phase shift of the readout transmission signal [31].

This can be seen in the dispersive approximation Hamiltonian of Eq. 2.25. Here, the dressed cavity frequency has a qubit state dependent shift $\omega_r = \omega_{r,0} + \chi\sigma_z$ relative to the bare cavity not coupled to the qubit. A probe sweep of the ground state, where $\langle\sigma_z\rangle = -1$ will produce a resonance at $\omega_r = \omega_{r,0} - \chi$. When a drive tone is applied at the qubit frequency, the steady state of the qubit will be incoherent with the cavity field and have an equal occupation probability of the ground and first excited states. This mixed state gives $\langle\sigma_z\rangle = 0$, which implies the bare cavity frequency $\omega_{r,0}$ will be observed in this case. We exploit the qubit-cavity interaction to measure the qubit via the cavity. With a readout tone fixed at $\omega_{r,0} - \chi$, a frequency sweep is performed with a much stronger drive tone. When the drive hits the qubit frequency, the cavity resonance changes by an amount χ , reducing the transmission and phase shift of the readout signal. Controlled rotations of the qubit on the Bloch sphere are thus not accessible in this scheme. In particular, there is no way to prepare the qubit in its excited state. The characterization of the qubit depends on the different system properties associated with the qubit ground state and the strongly driven incoherent state.

Substituting a frequency sweep for the fixed frequency readout signal allows for direct observation of the dispersive shift. This entails sweeping frequency in two dimensions, making simultaneous power sweeps exceedingly time consuming. Measurements are thus carried out at a fixed drive power of -10 dBm, and for a small number of different readout powers. Specifically, single photon power provides a strong signal without significant impact on the qubit state and coherence. The drive and probe tones are swept across the dressed qubit and cavity frequencies, respectively.

Naturally, then, for the two-tone experimental setup (cf. Fig. 3.12), a microwave source providing the drive tone is used in addition to the VNA, which generates the probe tone and records the output from the cavity. The drive and probe signals are mixed at room temperature using a power splitter/combiner. The mixed signal is then fed through the input line of the dilution refrigerator. As a microwave source generating the drive tone, we use three different devices, the SMF100A and SGS100A microwave signal generators from Rohde & Schwarz, as well as an Anritsu MG369C. For the purposes of our experiments, they perform the exact same function and are controlled via the LabView interface.

To protect the VNA port from the high power signal of the drive, 20 dB of attenuation is added at the probe tone output. Jitter and phase drift of the probe and drive tones are mitigated by connecting the microwave generator and VNA instruments to an external 10 MHz reference signal generated by a Rubidium source.

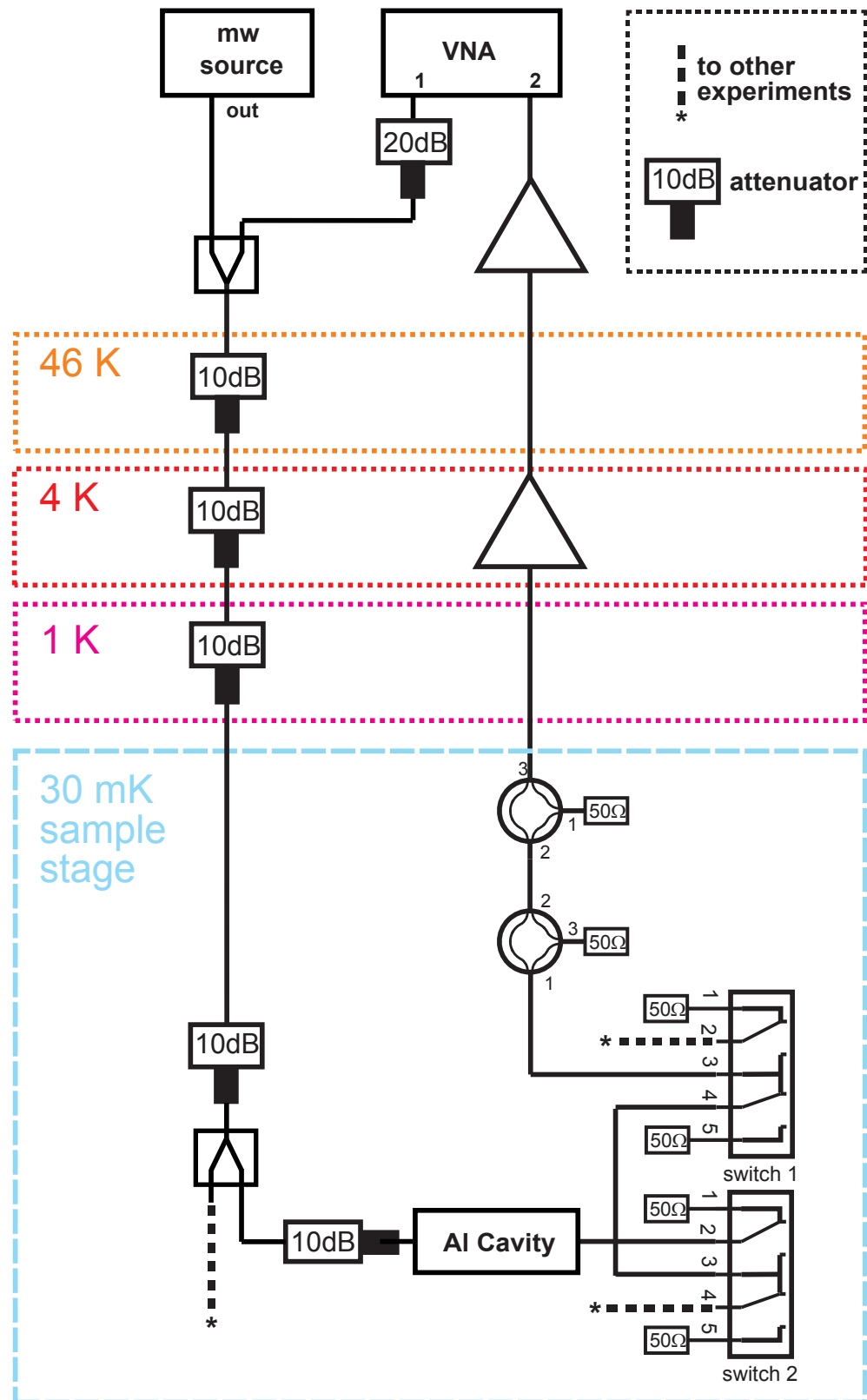


Figure 3.12: Circuit diagram of the cryogenic setup used in two-tone spectroscopy. The probe and drive signals are mixed at room temperature using a power combiner. The coloured boxes indicate temperature stages of the cryostat.

3.3 Simulations

The physics of microwave resonators and components play an important role in the design of quantum information processing experiments. For the analysis of our cavity resonators, qubits and other microwave elements, we rely heavily on finite element method (FEM) simulations of the electromagnetic field. With the commercial software tool CST Microwave Studio, we are able to conveniently implement representations of our designs and input signals, and solve for S-parameters as well as electromagnetic field distributions.

The FEM method is used to solve partial differential equation problems across many disciplines. It subdivides the domain into cells, and defines a finite-dimensional function space by introducing a set of basis functions that are each typically non-zero only on a few neighbouring cells. The solution to the differential equation problem is then projected onto this function space in such a way that the residual norm is in some sense minimized. This method is well suited to electromagnetic problems in the microwave regime, where geometric features are comparable in size to the wavelength. Compared to other computational methods, it is relatively straightforward to implement with complex domains [32] as there are few restrictions on the cell mesh. For the same reason, it can often handle boundary conditions rather easily and allows locally higher resolved regions to capture small and important features in an efficient manner.

In the CST environment, fully three-dimensional structures are discretized into a tetrahedral mesh. On the resulting geometry, Maxwell's equations are solved for a range of excitations in the frequency domain. Microwave ports are defined within the models to control the input and output signals and calculate S-parameters. With field monitors, it is also possible to obtain the full electromagnetic field distribution at given excitation ports and frequencies. The solver supports adaptive refinement of the mesh, enhancing accuracy in high-field regions and helping resolve small dimension segments such as qubit structures. Planar structure design is done in the circuit design tool, from which 3D models are automatically generated.

A model of the cavity geometry is implemented to analyse efficiently the effect of modifications and provide comparison for experimental data. It is also used to compute electric field values to analyse the coupling between qubit and resonator. Cross-sections of this model are shown in Fig. 3.13. The boundary conditions are obtained from the electronic properties of aluminium, available in the CST materials database.

Simulations are an excellent tool for the design and analysis of more advanced experimental configuration concepts. A scaled model is developed where two cavities are connected via a transmon qubit. The cavities have identical internal dimensions to the ones investigated experimentally. The model includes a transmon structure designed with a split junction with a loop area of $750 \mu\text{m}^2$, to enable flux bias tuning of the Josephson energy. In the model, the transmon is represented by its geometry, thereby coupling capacitively to cavity fields. Using the CST circuit design tool, we separately synthesize a

flux bias line with filtering to prevent qubit decay and resonator losses (cf. Fig. 3.14). It has to efficiently couple magnetic flux into the qubit junction inside the metal structure, meaning the filtering elements must be implemented on a compact space. This component is analysed independently and then incorporated into the two-cavity model. Figure 3.15 shows the composite system as implemented in CST. By defining waveguide ports at all cavity pins, the cross-transmission of the electric field between the cavities may be analysed. To represent the superconducting metallic structures and cavity walls, we use perfect electric conductor (PEC) boundary conditions. Although as discussed in Sec. 2.3, real superconductors have non-vanishing surface resistivity at radio frequencies, PEC boundaries provide the best approximation available while minimizing the computational complexity. The pin insertion depth of the two-cavity model is variable, but we will

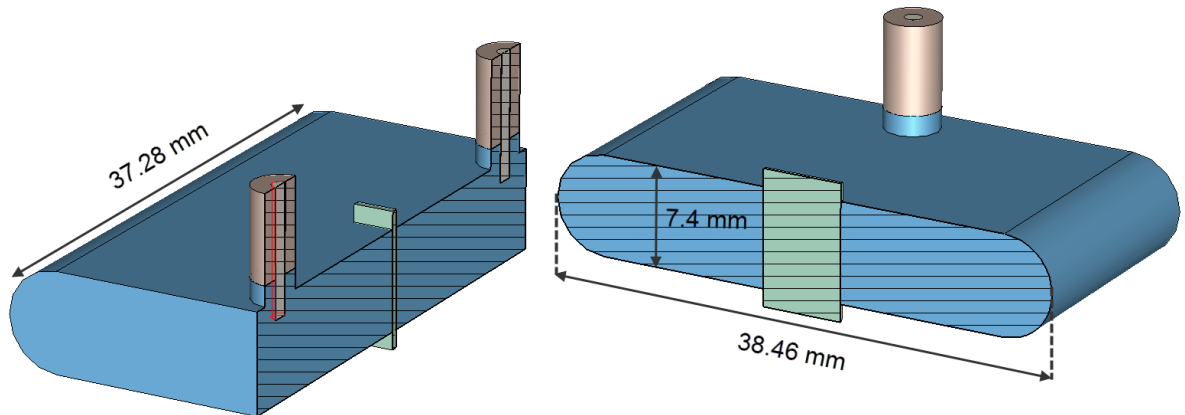


Figure 3.13: CST model of the cavity with a mounted transmon wafer. The dimensions shown in Fig. 3.2. Waveguide ports are added to the model at the top end of the metallic pins, modelled after the Huber and Suhner connectors. The blue colour represents vacuum, brown teflon, grey PEC and the silicon wafer is shown in green.

typically let -1.6 mm represent weak coupling to the environment and use a pin depth of 1.4 mm for the strongly coupled case. These values are chosen for comparison as they were implemented experimentally in the cryogenic setup. The simulated input power for S-parameter and electric field calculation is 1 W. Renormalizing this figure to reflect the much lower power accessible in our experiments was deemed redundant as this does not change the S-parameter results or the relative distribution of electromagnetic field energy.

We now turn to reviewing the results obtained from CST simulations of the models introduced here. We begin with a scheme for introducing magnetic bias flux into the single cavity model. Then, we present the results of the dual cavity architecture. Finally, we discuss the flux bias line in more detail.

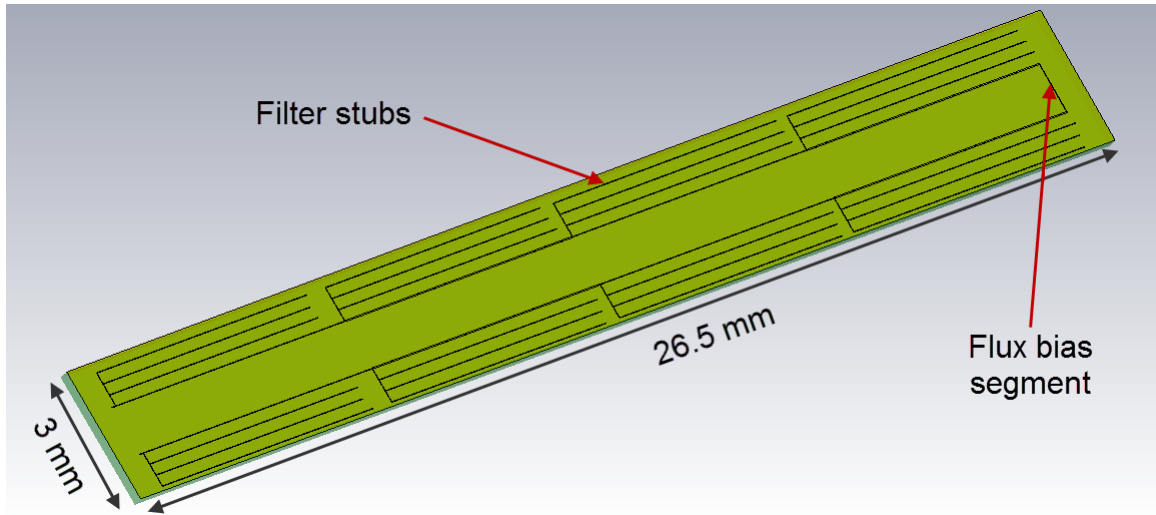


Figure 3.14: CST model of flux bias line with $\lambda/4$ filter stubs. The substrate is 26.5 mm long and 3 mm wide and has a thickness of 0.25 mm. The material is modelled after sapphire and has a relativ dielectric constant of $\epsilon_r = 11.5$. The stubs vary in length between 5.1 mm and 6.5 mm. The metal structures are 1 μm thick and 10 μm to 15 μm wide.

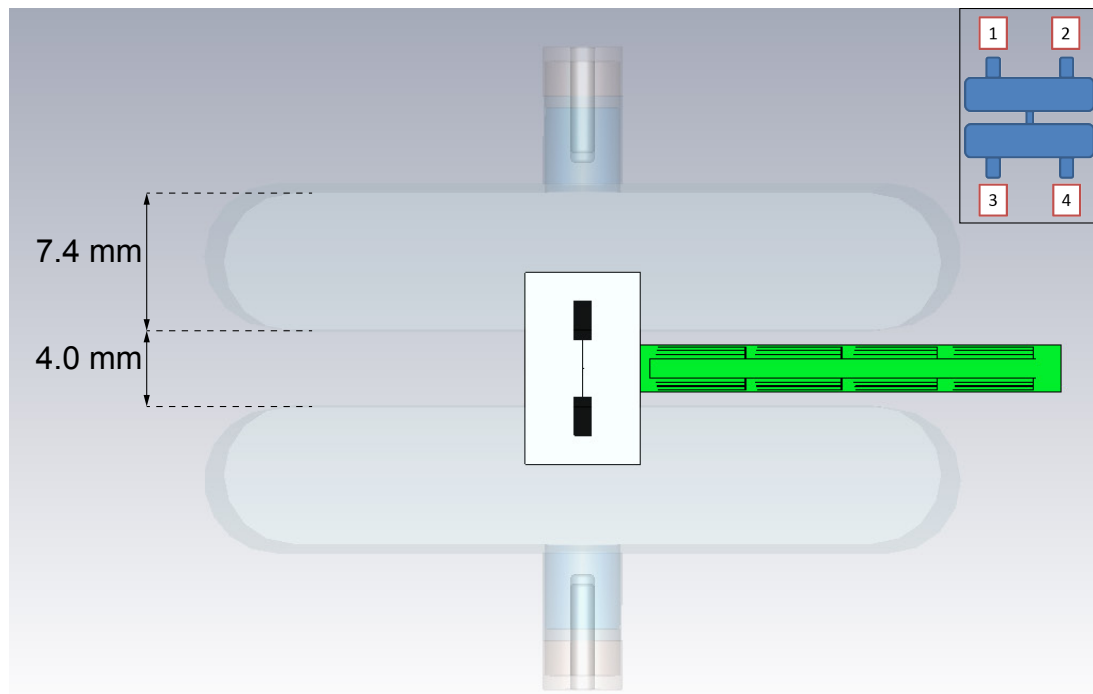


Figure 3.15: CST model of the two cavity model, highlighting the qubit and bias line structures. The top right inset shows the port numbering relevant to the S-parameter calculations.

3.3.1 Magnetic flux coupling

In our experimental configuration, the qubit parameters are fixed and other than the AC Stark shift, there is no way of tuning the transition frequencies. The ability to move the qubit in frequency space in and out of resonance with the cavity would open up a range of intriguing experimental possibilities, such as the influence of the cavity on the qubit decay rate. With a near resonant qubit, it is also possible to conduct vacuum Rabi oscillation experiments. However, the superconducting cavity walls effectively shields the transmon from any magnetic flux penetration. To enable tunability, we modify the alloy cavity to have one short end made from copper, which is magnetically permeable at all temperatures, rather than superconducting aluminium. In order to tune the Josephson

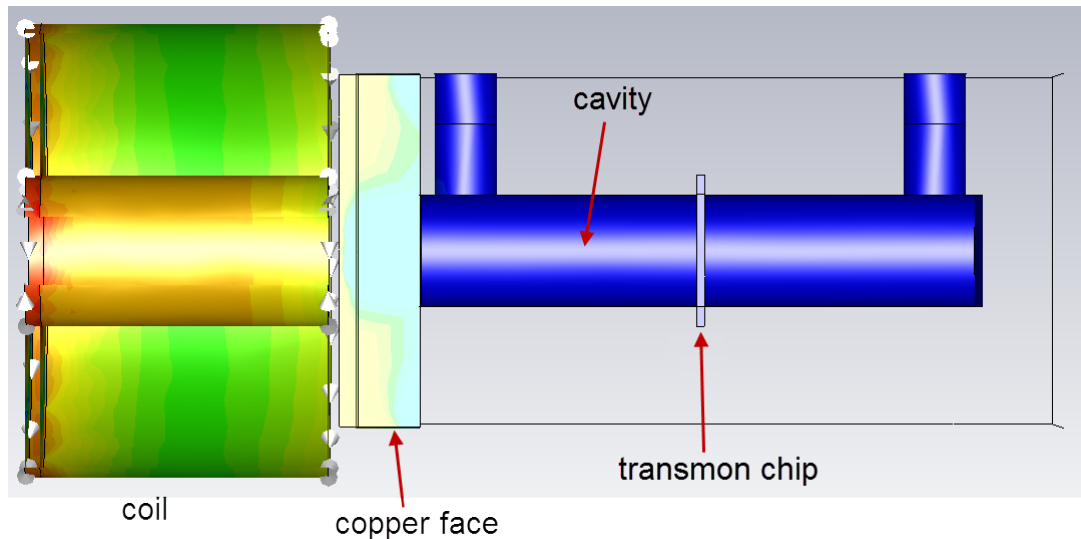


Figure 3.16: CST simulation of magnetic field penetration from an external coil through a copper face of the cavity. The field value at the transmon chip is relevant to flux bias tuning, and amounts to $B = 4.3 \mu\text{T}$.

energy of a split junction transmon, we have to be able to couple a magnetic flux of the order of one flux quantum Φ_0 through the SQUID loop. We simulate the copper face modified cavity, with the magnetic flux generated by a solenoid coil of the same dimensions as the superconducting coils available at WMI. The coil has inner and outer radii of 1 cm and 2 cm, respectively, and has 3000 turns on a length of 1 cm. With a loop current of 100 mA, which should not present any problems in an experimental setup, we observe a magnetic flux density of $4.3 \mu\text{T}$ at the qubit. The resulting magnetic flux through the $750 \mu\text{m}^2$ transmon loop for the design geometry exceeds Φ_0 . The simulated geometry is shown in Fig. 3.16.

3.3.2 Dual cavity simulation results

A possible future direction for 3D transmon experiments involves multiple resonators coupled via qubits. The perhaps most straightforward implementation of this idea consists of two resonators coupled via a "bridge" transmon whose pads extend into both cavities. In preliminary analysis, we are interested in how the microwave field propagates through the system, depending on the resonator architecture and qubit structures. Figure 3.17 shows a simulated electric field distribution for our two-cavity model for a near-resonant upper cavity input signal. The field shows significant amplitude also in the lower cavity. In Fig. 3.18, the excitation is further away from resonance, leading to a lower cross-transmission. The simulations are done with a transmon structure whose pads extend into either cavity by a distance of 1.5 mm. Computing the S-parameters, we observe strong field transmission between the cavities. In a low coupling coefficient configuration (retracted pins), the diagonal cross-cavity transmission S_{41} reaches the same magnitude as the internal transmission S_{21} (cf. Fig 3.19). In the opposite limit, the loss rate through the pins of the excited cavity dominate over the cross-transmission, leading to a suppressed signal at the diagonal port. This is plotted in Fig 3.20. Notably, when the qubit and wafer are removed from the cavity, the cavity-cavity coupling is further suppressed for the first mode while the second mode still couples significantly.

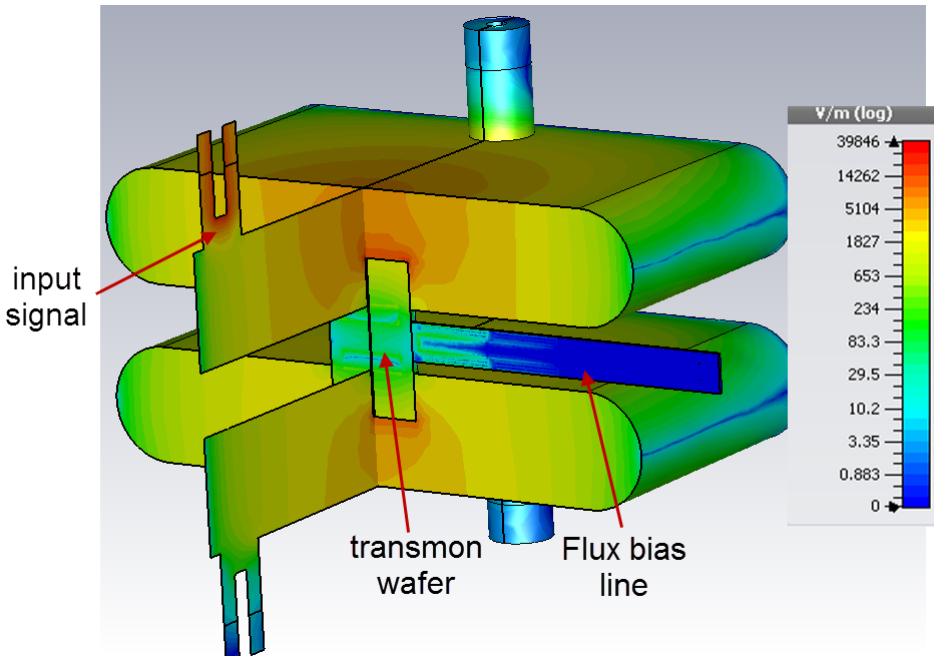


Figure 3.17: CST simulation of the electric field distribution from a near-resonant excitation in a two-cavity model (logarithmic scale). The simulated input power is 1 W.

The exchange of electromagnetic field energy between the cavities associated with the fundamental mode thus gives rise to three different transmission regimes, depending on the configuration. Without an inserted bridge transmon, the mode is isolated to a

single cavity by more than 100 dB.. With the transmon mounted, the field amplitude distributes evenly between the cavities in the limit where the external quality is high. The cross-cavity transmission then exceeds the external loss rate. With the pins inserted deeply into the cavities, leading to a high coupling coefficient, the external losses dominate over cross-transmission, resulting in an intermediate regime. If the qubit is in the strong coupling regime with respect to the cavity losses $g \gg \kappa$, the additional direct photon transfer between the cavities will not rule out the creation of two-cavity entangled photon states via the transmon. For a detailed discussion of the dynamics of such a system, see Ref. [33].

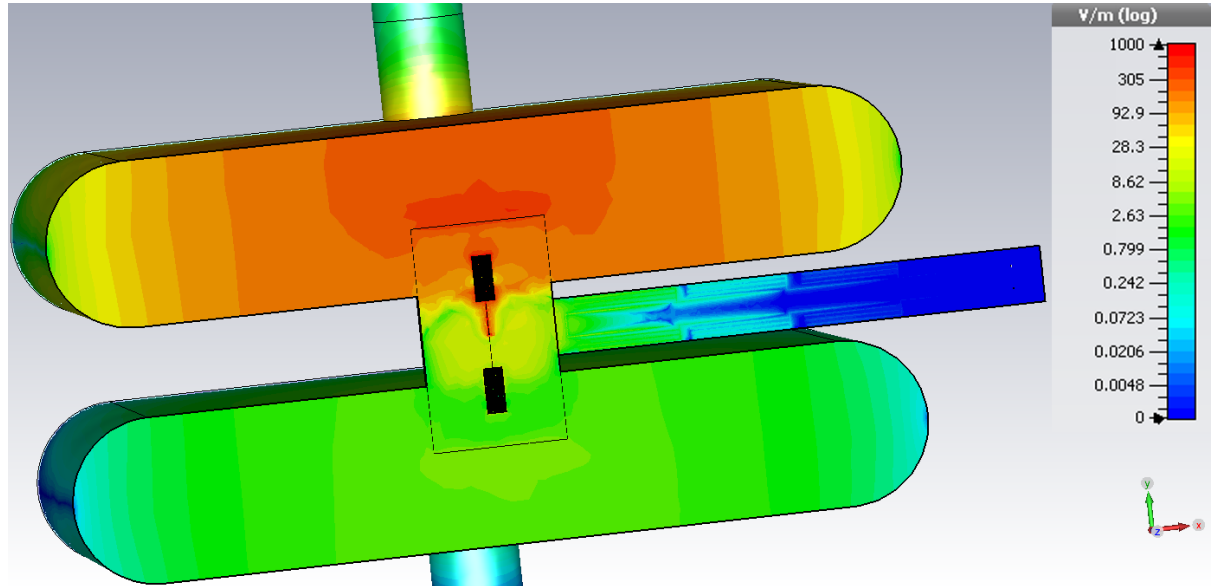


Figure 3.18: Cross-section of CST simulation of the electric field distribution showing the transmon structure (logarithmic scale). The propagation of the electric field through the flux bias line is clearly suppressed by the $\lambda/4$ stubs. The simulated input power is 1 W.

With coupling and loss parameters derived from our experimental investigation in Sec. 4.2, we perform basic simulations of qubit dynamics in a dual cavity system. Figure 3.21 shows the time evolution for a qubit coupled resonantly to two frequency-degenerate cavities, for the lowest excitation of the system. The amplitude of the Rabi oscillations decays slowly on the timescale of one cycle, suggesting that experiments with Rabi oscillations and non-local entangled state should be feasible in a scaled version of the current geometry.

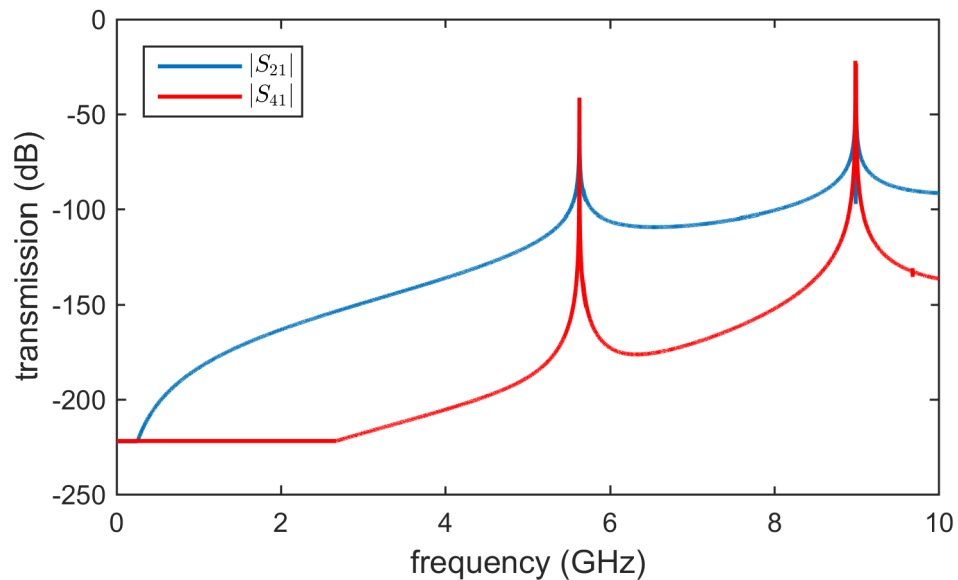


Figure 3.19: S-parameter simulation results of intra-cavity (S_{21}) and cross-cavity (S_{41}) transmission with the bridge transmon mounted and pin depth -1.6 mm at all ports.

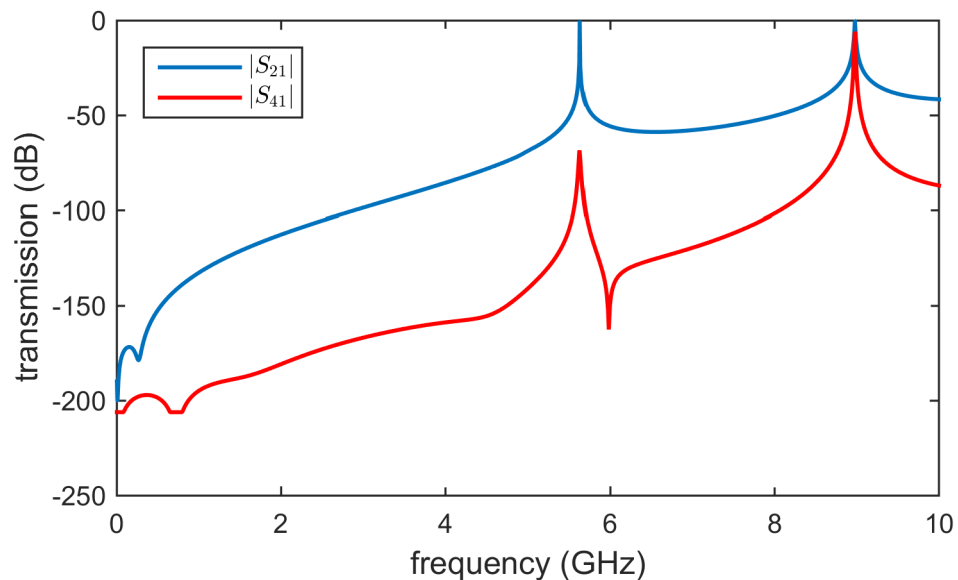


Figure 3.20: S-parameter simulation results of intra-cavity (S_{21}) and cross-cavity (S_{41}) transmission with the bridge transmon mounted and pin depth 1.4 mm at all ports.

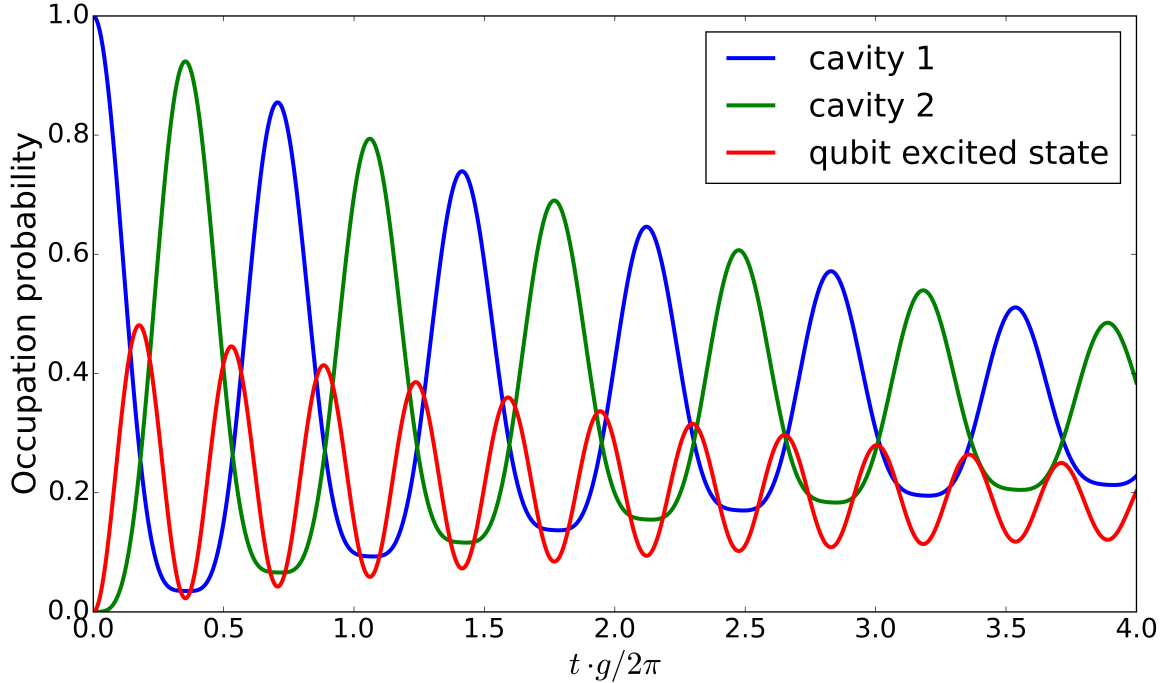


Figure 3.21: Time evolution of a qubit coupled resonantly to two cavities. The coupling g , resonator loss and qubit dephasing parameters are derived from the experimental results of Ch. 4. Direct photon exchange between the resonator is assumed to occur at a rate g_{AB} much lower than the qubit-resonator coupling frequency ($g = 10g_{AB}$). The initial state corresponds to a single photon in one of the cavities.

3.3.3 Bias line filtering

An important aspect of the bridge transmon design is the tunability of the Josephson energy E_J by magnetic flux coupled into the qubit loop via a flux bias line (FBL). While this enables tuning, the line also provides a decay channel for the qubit, potentially limiting coherence times [34]. In a Fermi's golden rule picture, the decay rate through the bias line turns out to be [35]

$$\Gamma_{FBL} = \frac{\text{Re}[Y(\omega)]}{C_q}. \quad (3.1)$$

Here, $Y(\omega)$ is the admittance of the bias line and C_q is the transmon capacitance. A low impedance line at the qubit frequency may thus contribute significantly to excited state depopulation. One way to overcome this problem is to filter the transmission line using $\lambda/4$ stubs [36]. These are stubs branching off from the transmission line that cause propagating microwaves with a wavelength four times the stub length to acquire a 180° phase shift, leading to effective suppression of transmission at this frequency. By adding multiple stubs of varying lengths, we are able to filter out a band of frequencies where

the qubit is in the dispersive regime. In this stop-band, the qubit may be tuned freely without coherence limitations due to the bias line. We aim to establish a stop-band around the cavity resonance at about 5.6 GHz, broad enough that we can access the dispersive limit $\Delta \gg g$ both above and below the cavity resonance. As the bias line loop remains connected, this scheme should not impair its ability to carry dc currents to generate the magnetic flux necessary for tuning.

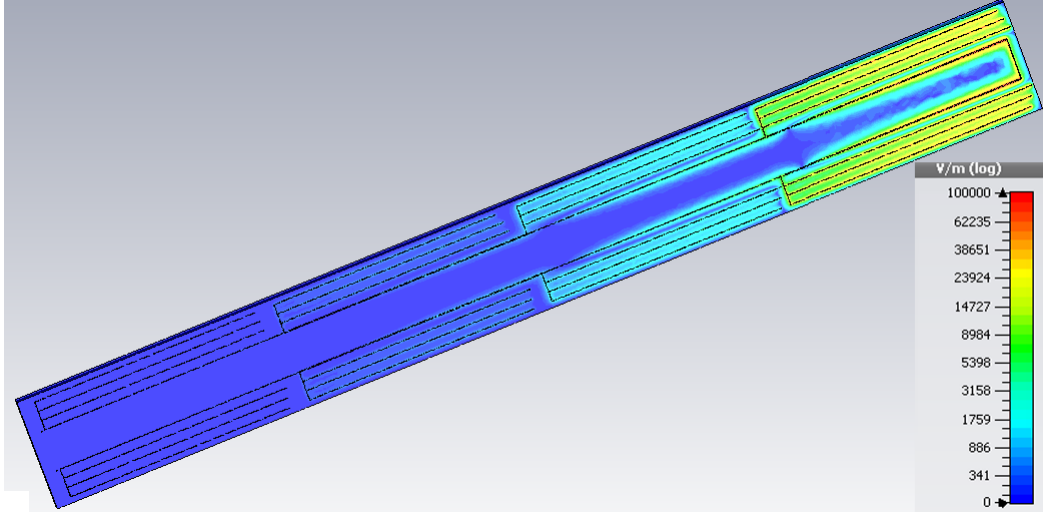


Figure 3.22: Electric Field distribution from CST simulation of a flux bias line model with $\lambda/4$ filter stubs. The excitation is introduced at the qubit side, where the line is parallel to the short end of the substrate. The simulated excitation frequency is 4.5 GHz, inside the stop-band of the filter stubs.

It turns out that the filtering effect is significantly impaired by crosstalk between the stubs, especially inductive crosstalk between parallel stubs on different branches. To optimize the design, ensuring sufficient filtering while keeping the structure compact to fit the narrow two-cavity geometry, we place the stubs on the outside of the flux bias line. The line is then designed to have a varying conductor width, to add further filtering and suppress resonances. Figure 3.22 shows the final design. The frequency-dependent transmission of the flux bias line is shown in Fig. 3.23. We obtain a stop-band of at least 30 dB suppression compared to low-frequency signals across a span of more than 3 GHz around the resonator frequency. The S-parameter magnitudes are related to the admittance [14], meaning S-parameter filtering directly affects this qubit decay channel. Our conclusion is that the simulated performance of the filter is sufficient to ensure qubit decay through the flux bias line is not limiting T_1 .

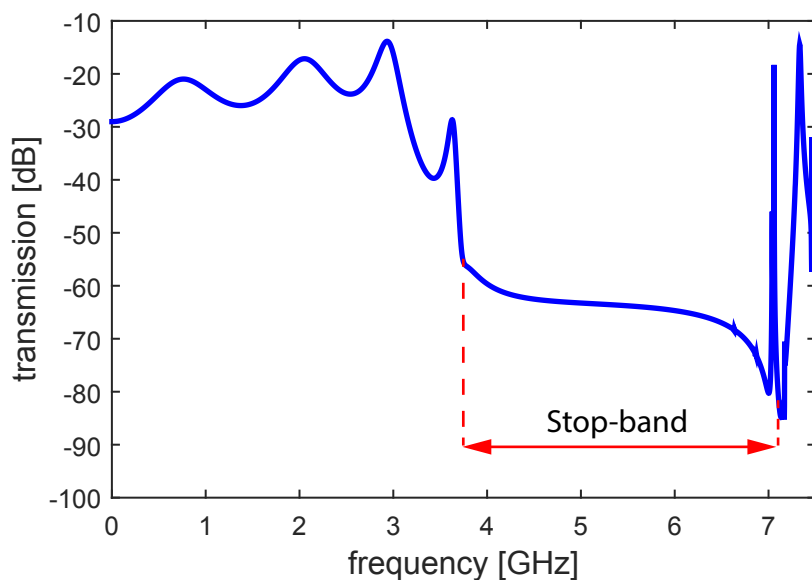


Figure 3.23: Simulated transmission $|S_{21}|$ between the two endpoints of the bias line, meaning the signal travels through both branches.

Chapter 4

Experimental results

In this chapter, the results obtained from the experimental investigations previously outlined are presented. We start with characterization of the cavities at room temperature as well as at cryogenic temperatures far below the superconducting critical temperature. Subsequent sections deal with qubit spectroscopy. Here we determine qubit parameters, calculate the coupling strength and calibrate the photon number population of the cavity.

4.1 Cavity characterization

As coupling qubits to 3D cavities is not something done previously at the WMI, an important first step is to understand the properties of the cavities themselves. This section presents the results of these investigation, focusing on transmission around the fundamental resonance frequency.

VNA recordings of the cavity spectra are compared with simulations to make sure the cavities display the intended properties. Figure 4.1 shows the absolute value of the electric field at the fundamental resonant mode at $f_r = 5.71$ GHz. Field values are displayed for a cut in the $x - z$ plane at $y = 3.4$ mm, which is the symmetry plane normal to the y -axis. The electric field distribution corresponds to the TE_{101} mode of a rectangular waveguide cavity, with a maximum in the center and polarization along the y -axis.

4.1.1 Room temperature characterization

We characterize the cavity transmission at room temperature in terms of fundamental resonance frequency and quality factors. We observe that the quality depends on the metal surface and how strongly the cavity is coupled to the environment. The resonance frequency may be tuned by varying the insertion depth of the pins as they introduce a small shape perturbation into the resonant volume, altering the mode shape. The pin depth also determines the coupling of the resonator to the input and output lines and thereby the external quality factor.

With the pins retracted, 1.1 mm away from entering the cavity volume, we measure the transmission sweeping the frequency up to 17 GHz for the alloy cavity. The first mode

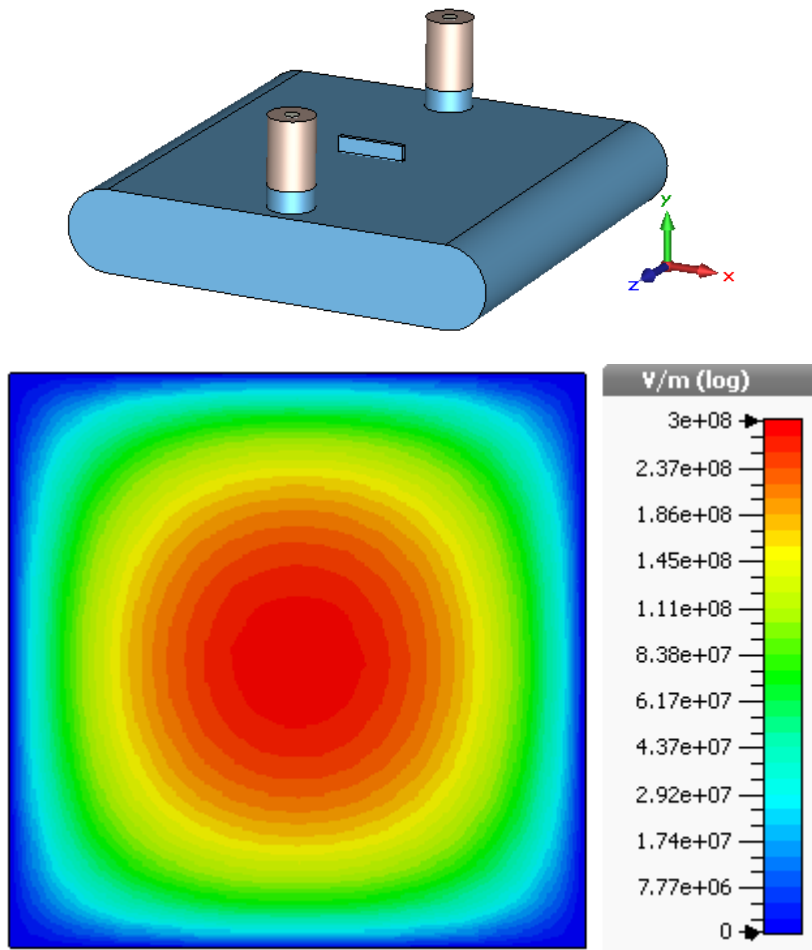


Figure 4.1: Resonant volume defined for simulations in the CST environment (top) and simulated electric field distribution of fundamental cavity mode at 1 W input power (bottom).

of the cavity is found at 5.69 GHz and the second 8.97 GHz. These correspond to the TE₁₀₁ and TE₁₀₂ modes, respectively. As plotted in Fig. 4.2, the latter exhibits stronger transmission, the reason being that this mode has a greater electric field amplitude at the pin positions.

In Fig. 4.3 we compare measurements for the aluminium cavity to CST simulations for a pin depth of -0.1 mm. The results are in good agreement, with a higher quality obtained in simulation. The simulated system has a perfectly smooth surface of perfect metallic purity. As further analyses will show it is not surprising that the measured cavity performance is slightly lower. The difference in resonance frequency of $\sim 3\%$ is also attributed to fabrication imprecision, the plausible cause being that excess volume is removed during milling compared to specification. The different transmission magnitudes is caused mainly by different couplings to the environment, a result of imperfect pin depth calibration. At -0.1 mm, the value used in this measurement, a change in pin depth of approximately 0.2 mm is sufficient to double the transmission. The resonance frequency

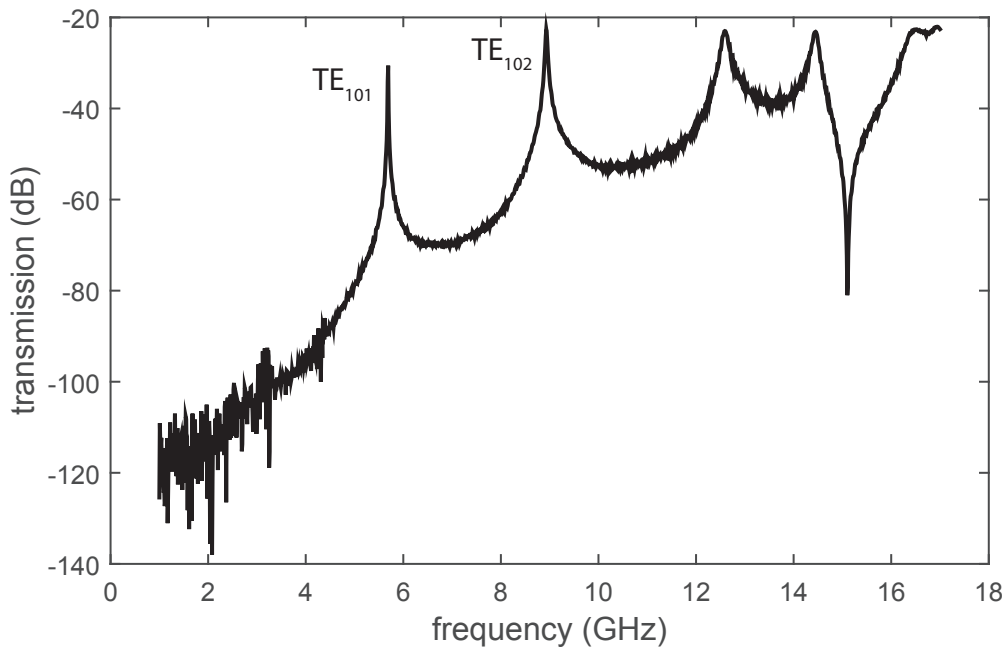


Figure 4.2: Broad frequency sweep of the alloy cavity transmission at room temperature. The peaks corresponding to the first and second cavity modes are marked. The VNA power is set at -10 dBm .

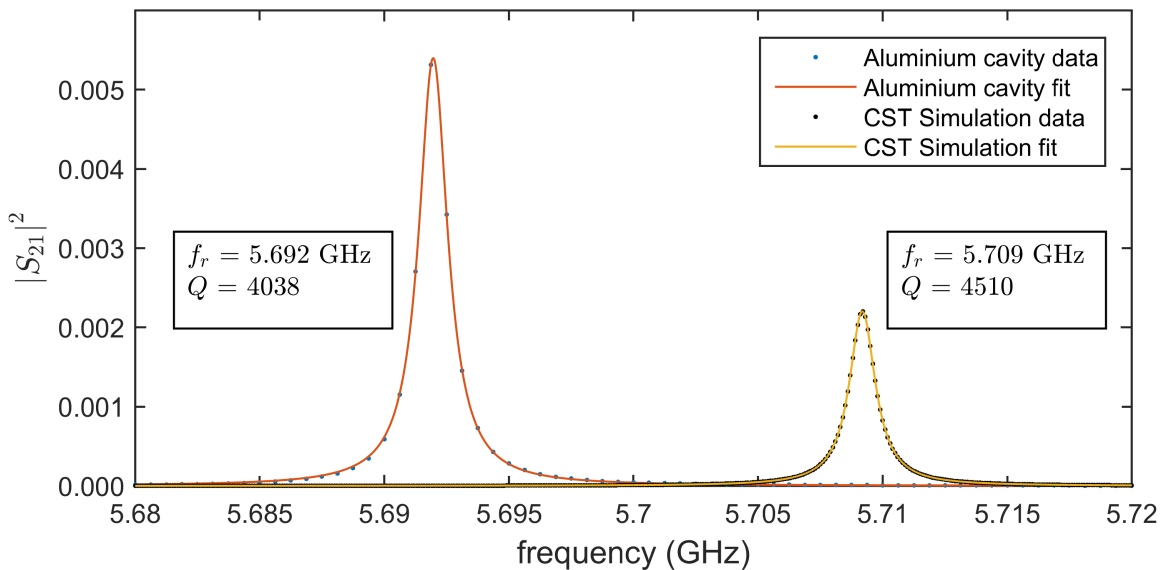


Figure 4.3: Cavity transmission spectrum data and fit at room temperature compared to simulation. Fitted parameters are shown next to the corresponding peaks. The differences in resonance frequency ($\sim 3\%$) and Q ($\sim 10\%$) are caused mainly by fabrication issues. The different transmission magnitude is attributed to the pin depth calibration.

and Q are not strongly affected to pin depth variations in this regime (cf. Figures 4.4 and 4.6).

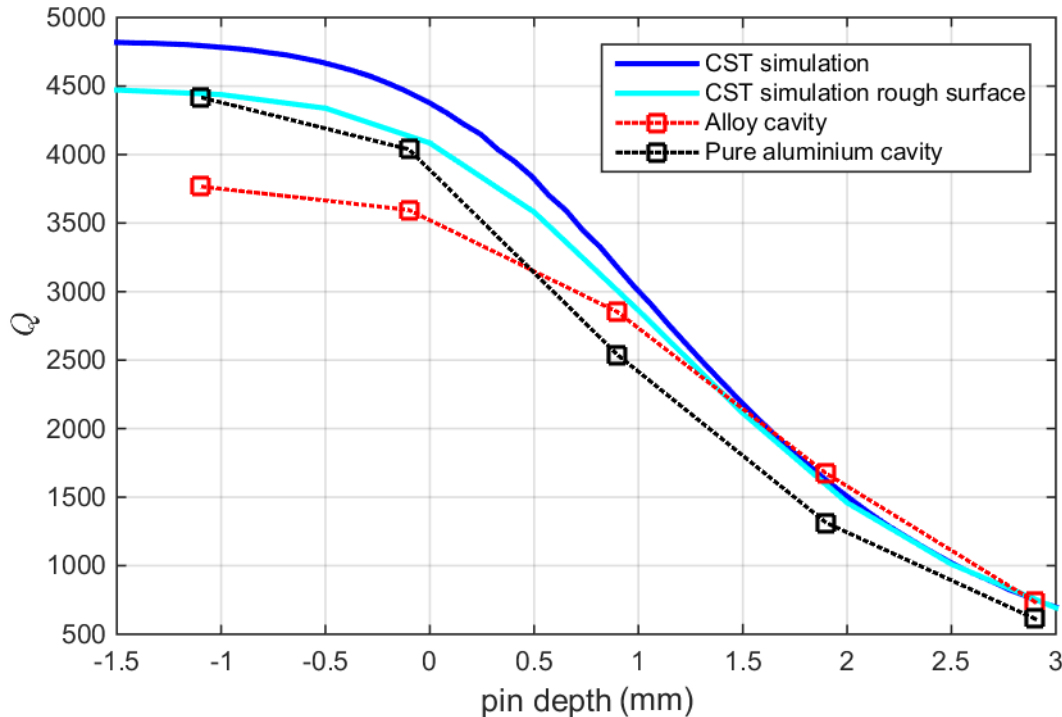


Figure 4.4: Quality factor vs. pin insertion depth for simulated and measured configurations.

Figure 4.4 shows how the loaded quality factor varies with pin insertion depth. A pin depth of 0 mm indicates that the bottom of the pin is level with the inner top surface of the cavity. Results for the two cavities are compared to simulations. One of the simulated models incorporates a number of surface structures of feature size $100 \mu\text{m}$ to investigate the effect of surface roughness. In the retracted pin limit, the input signal couples weakly into the cavity and the loaded Q -factor is limited by the internal Q . A pin insertion depth of several millimetres ensures almost all input power enters the cavity and couples the cavity field strongly to the measurement lines. The external quality deteriorates and dominates Q in this limit. We observe that surface roughness does cause losses, which may explain part of the deviation of our systems from ideal simulations. The inferior performance of the alloy cavity at negative pin depth has plausible causes in surface damage sustained in the milling process as well as the lower grade fabrication material. When the pin extends far into the cavity, the alloy cavity gives a higher Q than the pure cavity. This is due to its weaker coupling coefficient, leading to a higher external quality, which is the limiting factor in this regime. The weaker coupling is apparent in the transmission magnitudes and likely caused by the slightly larger internal volume of the alloy cavity, a result of fabrication imprecision.

Measurements with a silicon wafer mounted are also carried out at room temperature.

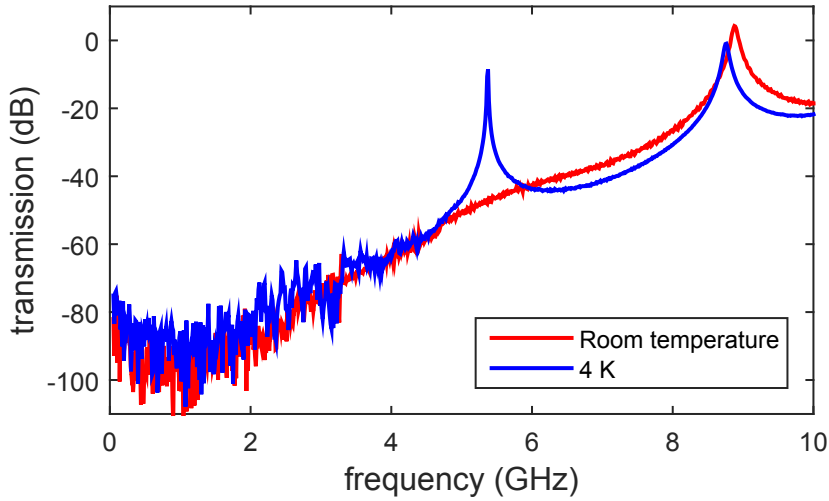


Figure 4.5: Alloy cavity transmission with a silicon wafer of the type used as substrate for qubit structure mounted in the center. The first mode is suppressed at room temperatures, where the silicon has a high impurity conductivity.

The high impurity conductivity of the silicon at room temperature leads to complete suppression the first mode, as the amplitude of the electric field is maximal precisely at the wafer position. When cooling the system sufficiently to freeze out the impurity conductivity, the first mode appears again, at a frequency shifted down due to the effect of the dielectric chip. This is shown in Fig. 4.5. The second mode, with a minimal electric field at the cavity center, is only moderately affected. The effect of the wafer on the fundamental mode frequency and Q is therefore not accessible by room temperature measurements.

4.1.2 Frequency tuning

One objective of this thesis is to develop and evaluate methods of tuning the resonance frequency. Tunability is useful for scaling up the number of frequency degenerate cavities in a qubit coupled resonator network. Ideally, tuning should be possible *in situ*, even as the cavity is cooled down to millikelvin temperatures, and not significantly impact the cavity parameters in other ways. In general, tuning is accomplished by altering the mode volume of the cavity [14].

Changing the pin depth is one obvious way of tuning, as the metal pins protrude into the mode volume of the cavity. However, as variations in the pin depth change the coupling of the cavity to the environment, this tuning approach brings about a substantially larger relative difference in external Q than in resonance frequency (cf. Fig. 4.6). We are therefore interested in developing and testing other manipulation methods.

A dielectric perturbation shifts the resonance frequency by changing the dielectric

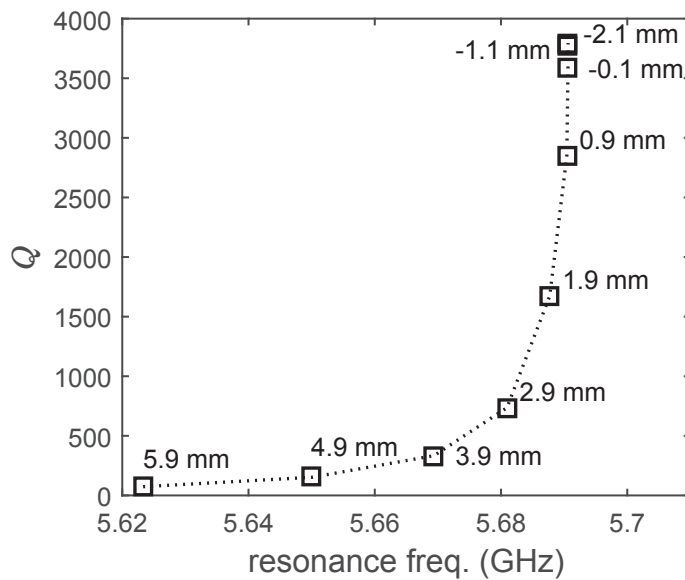


Figure 4.6: Quality factor and resonance frequencies for alloy cavity tuning by pin depth variation. Data points are annotated with the pin depth.

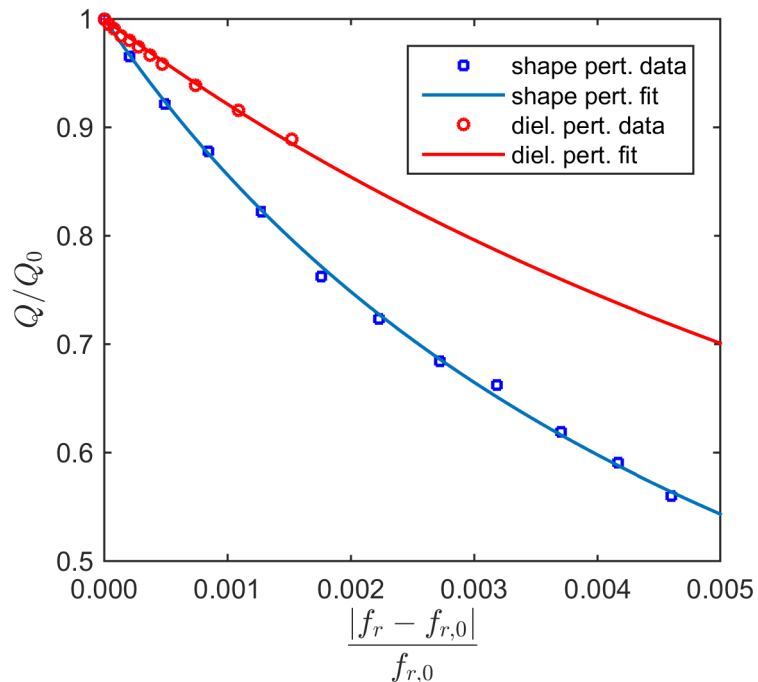


Figure 4.7: Quality factor and resonance frequencies for alloy cavity tuning by dielectric and shape perturbation. We use the absolute value of the frequency change as the different tuning mechanisms lead to shifts of different sign.

constant of a segment of the resonant volume [14]. Tuning by insertion of a dielectric perturbation in the form of a sapphire chip has been investigated previously in this project [37]. We modify this approach and use instead a teflon screw inserted through one of the cavity short end faces. This increases the dielectric constant for part of the volume, leading to a downshift in the resonance frequency.

In addition, we alter the resonance by perturbing the shape of the resonating volume. This is done by substituting a metallic screw for the teflon. Note that as this effectively leads to a smaller cavity, the resonance is shifted up in frequency rather than down. It is clear that either method provides more efficient tuning than varying the pin depth. As the components of the total Q add reciprocally, we have

$$Q = \left(\frac{1}{Q_0} + \frac{1}{Q_p} \right)^{-1} \quad (4.1)$$

where Q_0 denotes the loaded Q in absence of tuning, and Q_p describes losses due to the perturbation. Normalizing Q with respect to the initial value, this gives

$$\frac{Q}{Q_0} = \left(1 + \frac{Q_0}{Q_p} \right)^{-1}. \quad (4.2)$$

For tuning structures much smaller than the mode volume, the relative change in the resonant frequency is linear in the volume of the perturbation [14]. In this limit, we also expect the surface or dielectric losses due to tuning to be linear in the screw insertion distance and therefore proportional to the perturbation volume

$$\frac{1}{Q_p} \propto |\Delta\nu| \quad (4.3)$$

$$\Delta\nu = \frac{f_r - f_{r,0}}{f_{r,0}}. \quad (4.4)$$

Here, the unperturbed cavity resonance frequency is denoted by $f_{r,0}$. In order to compare the two methods of tuning, we again normalize to Q_0 and express (4.4) as

$$\frac{Q_0}{Q_p} = \kappa_{\text{pert}} |\Delta\nu|. \quad (4.5)$$

The constant κ_{pert} quantifies the additional losses introduced by tuning, meaning a low value is desirable. Inserting into Eq. (4.2), we get

$$\frac{Q}{Q_0} = (1 + \kappa_{\text{pert}} |\Delta\nu|)^{-1}, \quad (4.6)$$

where $\kappa_{\text{pert}} = \kappa_{\text{shape}}, \kappa_{\text{dielectric}}$ for shape and dielectric perturbation, respectively. We fit the expression from Eq. (4.6) to the measured data and plot the result in Fig. 4.7.

The obtained parameters are $\kappa_{\text{shape}} = 168$ and $\kappa_{\text{dielectric}} = 85$. At room temperature, the dielectric provides more efficient tuning. The same relative change in resonance frequency induces almost twice as high additional losses for the shape perturbation. At cryogenic temperatures, however, the shape perturbation may provide superior tuning. In the following section, we will see that losses in the cavity wall are drastically reduced for a superconducting cavity.

4.1.3 Cavities at cryogenic temperatures

A superconducting cavity greatly enhances the internal quality compared to normal state metal. Ideally, superconducting cavity walls have a minimal surface resistivity, reducing internal losses [38]. We therefore obtain a drastically higher Q-factor at cryogenic temperatures of approximately 50 mK, far below the superconducting critical temperature for aluminium of 1.2 K. For the alloy cavity, we compare results recorded before and after electropolishing. The electropolishing was performed by Poligrat GmbH in Munich. The data with fitted Lorentzian lineshapes is plotted in Fig. 4.8 and Fig. 4.9.

Previous studies have demonstrated improvement in the Q-factor for copper cavities after surface treatment with electropolishing [16]. It may appear as counter-intuitive that in our case, the resonator quality decreased as a result of this procedure. The supplier attributed this effect to the varying etch rates of different elements of the alloy. Surface profile recordings show a characteristic average roughness of 0.295 μm and 0.627 μm , respectively. The curved sections of the cavity has visible ridges from the milling process. Here, electropolishing did reduce the characteristic roughness, from 1.280 μm to 0.978 μm . Note also the lowered resonance frequency for the electropolished cavity (cf. Fig. 4.9). Detailed electropolishing results are presented in Appendix B. The polishing process removes surface material, thus expanding slightly the cavity volume. The lower noise level in the polished cavity data is due to the addition of a room temperature amplifier to the output line. The reduction in resonator quality did not persist at room temperature, indicating that the electropolishing procedure did indeed cause lattice defects in the metal walls. This affects the residual surface resistance important in the BCS picture, while at room temperature the normal-metal resistivity dominates.

Figure 4.10 plots the transmission of the pure aluminium cavity in the high power limit, with a cavity photon number population $n_{ph} > 10^6$. Compared to room temperature data, we obtain a Q of 678 000, an effect of superconductivity, while the resonance frequency is shifted upwards. This indicates a shrinking of the cavity due to thermal contraction of the aluminium hull. The transmission and loaded Q may be used to establish a lower bound to the internal quality factor Q_{int} . We recall from Sec. 2.3 that for a cavity with

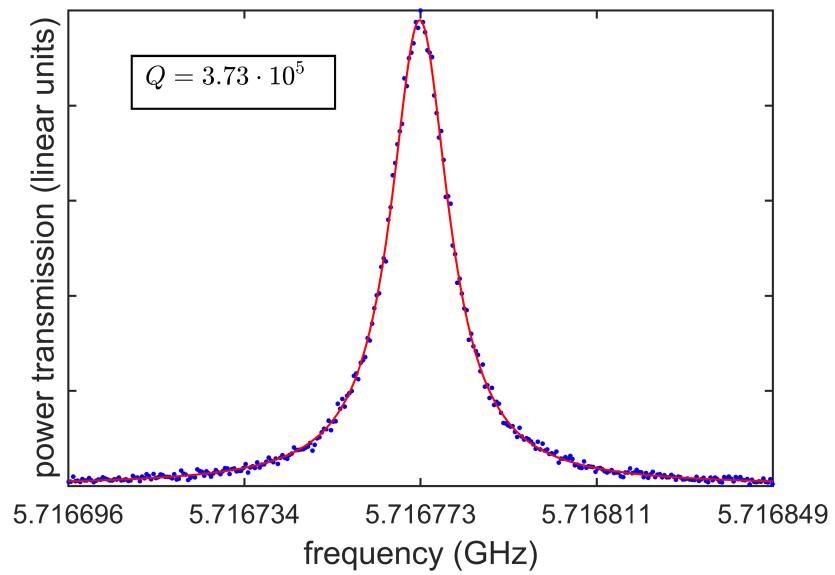


Figure 4.8: Transmission data (dots) and fit (line) for the alloy cavity at 50 mK before electropolishing. The resonance linewidth (FWHM) equals 15.3 kHz. The measurement is done with a pin depth of -1.1 mm.

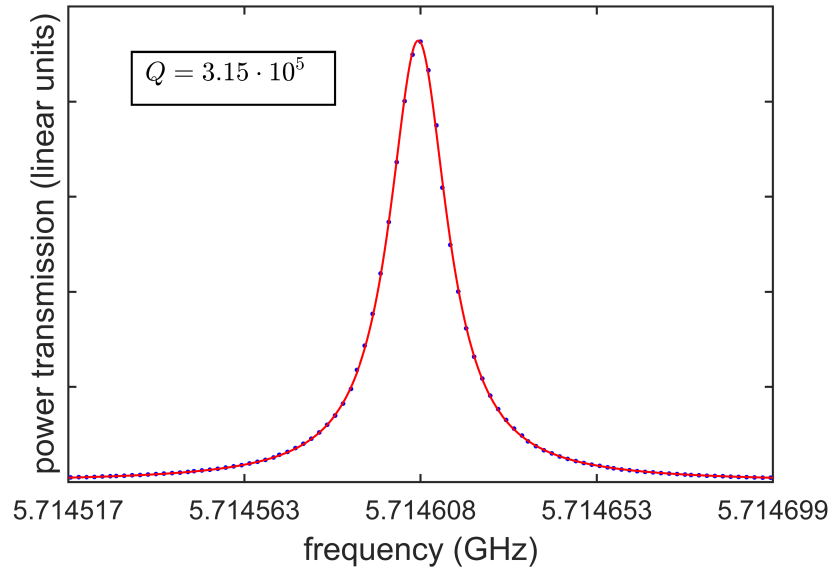


Figure 4.9: Transmission data (dots) and fit (line) for the alloy cavity at 50 mK after electropolishing. The resonance linewidth (FWHM) equals 18.1 kHz. The measurement is done with a pin depth of -1.1 mm.

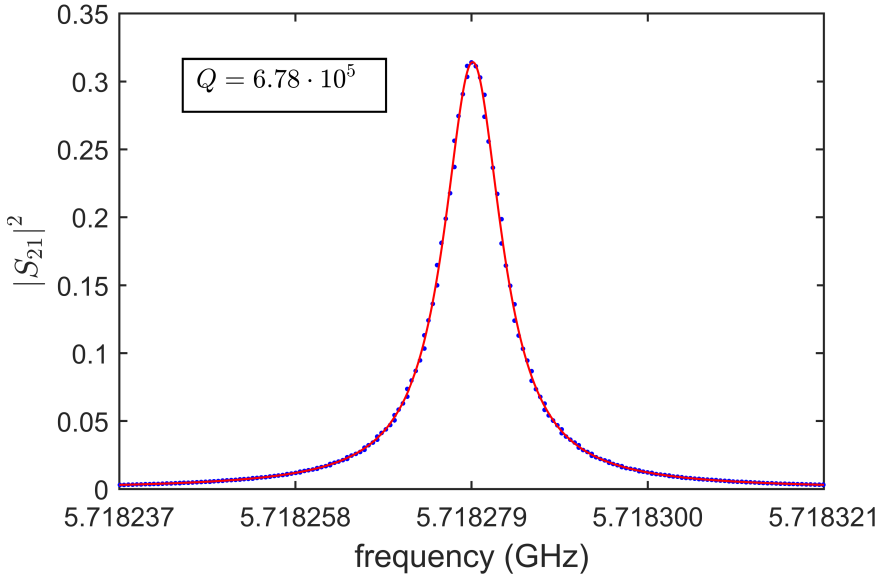


Figure 4.10: Calibrated transmission data (dots) and fit (line) for the pure aluminium cavity at 50 mK. The resonance linewidth (FWHM) equals 8.43 kHz. The measurement is done with a pin depth of -1.6 mm .

symmetric coupling to the environment, these quantities are related by

$$Q_{int} = (1 + 2k)Q \quad (4.7)$$

$$k = \frac{|S_{21}(f_r)|^2}{1 - |S_{22}(f_r)|^2 - |S_{21}(f_r)|^2} \quad (4.8)$$

Assuming, quite unrealistically, that $|S_{22}(f_r)|^2 = 0$, we obtain $Q_{in} > 1.3 \cdot 10^6$ for the aluminium cavity. This estimate neglects completely the reflected power. The cavity impedance, as measured with time domain reflectometry (TDR), does not deviate significantly from the vacuum value of $Z_0 \approx 377\Omega$. The impedance mismatch between the cavity and the input line (matched to 50Ω) then causes reflection, which our TDR measurements confirmed. In addition, the input line acts as a loss channel for photons that have entered the cavity, meaning the lower bound obtained in our estimate is a conservative one. Room temperature measurements and simulations show consistently a greater reflected than transmitted power at resonance for the pin depth used. Taking the reflection to equal the transmission, which then should still underestimate the internal quality, the estimated bound is improved to $Q_{int} > 1.9 \cdot 10^6$.

Measurements during cooldown at temperatures above T_c show moderate increases in Q . For the alloy cavity, the loaded quality improves by less than a factor of two until the aluminium turns superconducting, showing that the reduced ohmic resistivity associated with cooling does have an effect, however not comparable to the superconducting phase transition.

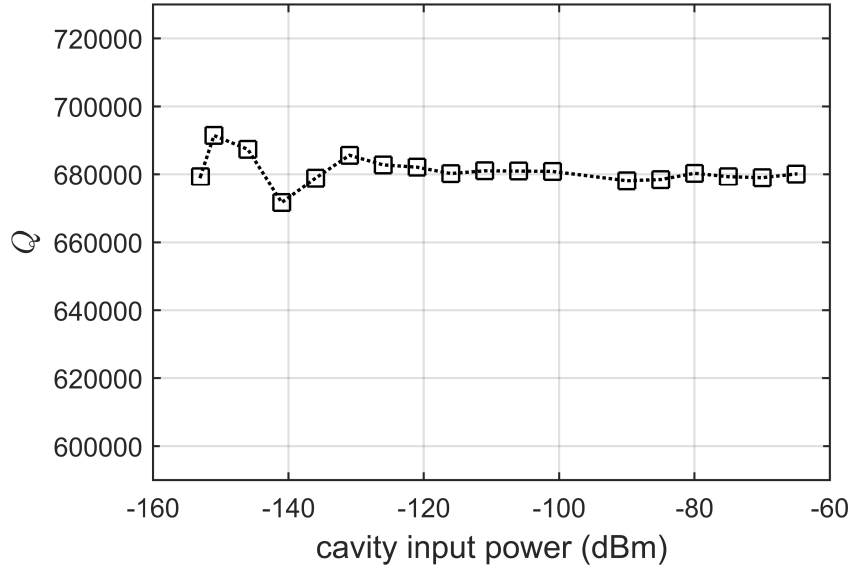


Figure 4.11: Loaded quality factor versus estimated input power at the cavity at 50 mK for the aluminium cavity. Single photon power corresponds to an input power of -115 dBm.

A rough photon number estimate can be obtained by relating the input power to the loss rate per photon κ . From conservation of energy

$$P_{\text{in}} = E_{\text{stored}}\kappa \quad (4.9)$$

$$E_{\text{stored}} = \hbar\omega n. \quad (4.10)$$

The losses in the input lines are estimated to -56 dB. We sweep the input power down to the single photon level to determine the power dependence of the loss rate. For coplanar waveguide (CPW) resonators, the quality factor degrades in the low power limit [39]. As evident from Fig. 4.11, no such effect is observed for our 3D cavity. Our aluminium cavity demonstrates a high, power independent quality factor. An important reason for the power dependence of CPW resonator loss is absorption due to two-level systems in the substrate [40]. At high powers, defects at dielectric surfaces, interfaces and bulk get saturated, reducing this contribution to the loss rate. In the 3D cavity there is no expected introduction of two-level systems into the mode volume through circuit boards or other dielectric materials. The diluted field in the large mode volume also reduces sensitivity to localized concentrations of defects. Low cavity losses even in the single photon limit enhance the efficiency of quantum experiments as the number of repetitions required to obtain good statistics is reduced. Higher resonator quality also means stronger T_1 modulation via the Purcell effect, as discussed in Sec. 2.4.

4.2 Qubit spectroscopy

This section contains the results obtained from experiments with the transmon qubit mounted in the cavity. First, we present data recorded using a fixed frequency, continuous wave readout tone while sweeping the power and frequency of the drive. This is done at low readout powers to determine the qubit properties, as well as in the high power regime where the bare cavity resonance appears. This data is used to determine the dispersive shift and resolve the photon number population of the cavity. We also observe the qubit-induced shift directly in the cavity spectrum, by sweeping the frequency of the readout tone as well as that of the drive. This allows us to map out the effect of the qubit drive on the full resonance lineshape, rather than a single frequency. Power figures refer to output power at room temperature microwave sources.

4.2.1 Two-tone continuous wave readout

With a variable frequency drive, we measure the cavity response at the ground state resonant frequency to infer the properties of the qubit. The first qubit transition frequency is found at $f_{01} = 3.648 \text{ GHz}$ for low readout power (~ 1 photon). As this implies negative detuning Δ , we have $\chi < 0$ and the ground state dispersively shifted cavity frequency is higher than the bare resonance. The steady-state population of the qubit excited state is a Lorentzian centred around the transition frequency [41]. Figure 4.12 shows a spectroscopic line recorded at low power with a Lorentzian fit. At higher powers, where the spectroscopy photon number $n_p > 10$, Gaussian profiles turn out to fit data better (lower residual norm) than Lorentzians. This is likely due to inhomogeneous broadening of the qubit caused by electric field fluctuations that arise when the photon injection rate into the cavity exceeds the loss rate per photon.

As the readout power is increased, the qubit transition broadens and shifts down in frequency. This change in transition frequency is known as the ac Stark shift. From Eq. (2.24), we know that it is proportional to the photon population in the cavity and has a slope of $2g^2/\Delta$. Our transmon is coupled strongly to the cavity field, leading to a significant effect as evident in Fig. 4.13 (a). Fitting lines to this data, we extract the qubit frequencies from the peak locations. These are plotted in Fig. 4.13 (b). In the low power limit, where the photon population $n_p < 1$, no spectroscopy power effect on the qubit frequency is observed. Here, we confirm the dressed vacuum qubit frequency to be $f_{01} = 3.648 \text{ GHz}$. Spectroscopy data for low powers is plotted in Fig. 4.14.

The FWHM of the qubit spectroscopy line depends on the probe power and qubit decay times [42]

$$\pi \cdot \Delta f_{FWHM} = \left(\frac{1}{T_2^2} + \frac{n_p (2g)^2 T_1}{T_2} \right)^{1/2} \quad (4.11)$$

where n_p denotes the number of spectroscopy photons in the cavity. In the low power

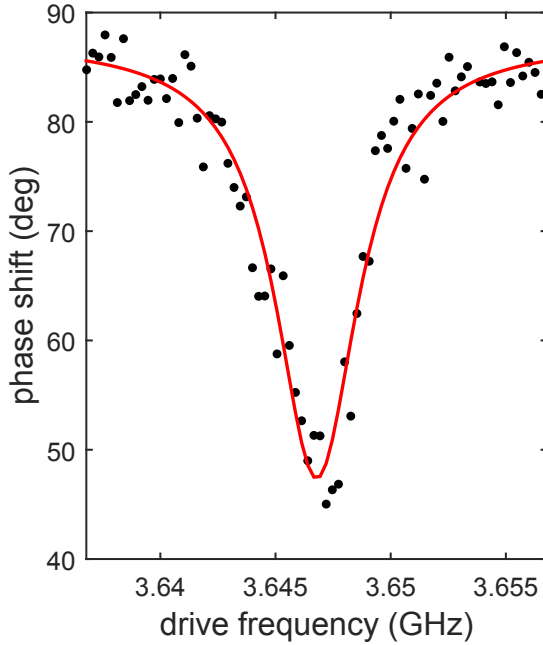


Figure 4.12: Probe tone phase shift data vs. drive frequency. The probe tone power is -42 dBm (average photon number $n_p = 0.5$). at the frequency $f_p = 5.4635$ GHz.

limit, the linewidth of the qubit transition yields a rough estimate of the dephasing time T_2 [41].

$$1/T_2 = \pi \cdot \Delta f_{FWHM}. \quad (4.12)$$

We fit Lorentzians to the spectroscopic lines to estimate the linewidth at different readout powers (cf. Fig. 4.15). The photon number depends linearly on the probe power. By Eq. (4.11), the square of the qubit FWHM should as well. Making a linear fit and extrapolating to zero power, we obtain a T_2 in excess of 500 ns (cf. Fig. 4.15). The energy relaxation time T_1 is not accessible by a similar estimate, but a lower bound is given by the relation $T_1 \geq T_2/2$. For comparison we estimate the spontaneous emission rate in free space using Fermi's golden rule. Suppression of the energy relaxation rate compared to free space due to the Purcell effect has been observed in similar architectures [26]. This decay time is given by [43]

$$\frac{1}{T_1} = \frac{\omega^3 |\mu|^2}{3\pi\epsilon_0\hbar c^3}. \quad (4.13)$$

Here, ω is the angular frequency of the transition and μ is the dipole moment of the qubit, which we estimate in Sec. 4.2.2 based on the transfer of a single Cooper pair across the junction. The thus obtained estimate of $T_{1,FGR} = 1.2 \mu\text{s}$ does not indicate any improvement over the vacuum decay rate due to the cavity for our system. However, as sources of dephasing are likely present in the system [3, 44], T_2 may not reach the $2T_1$

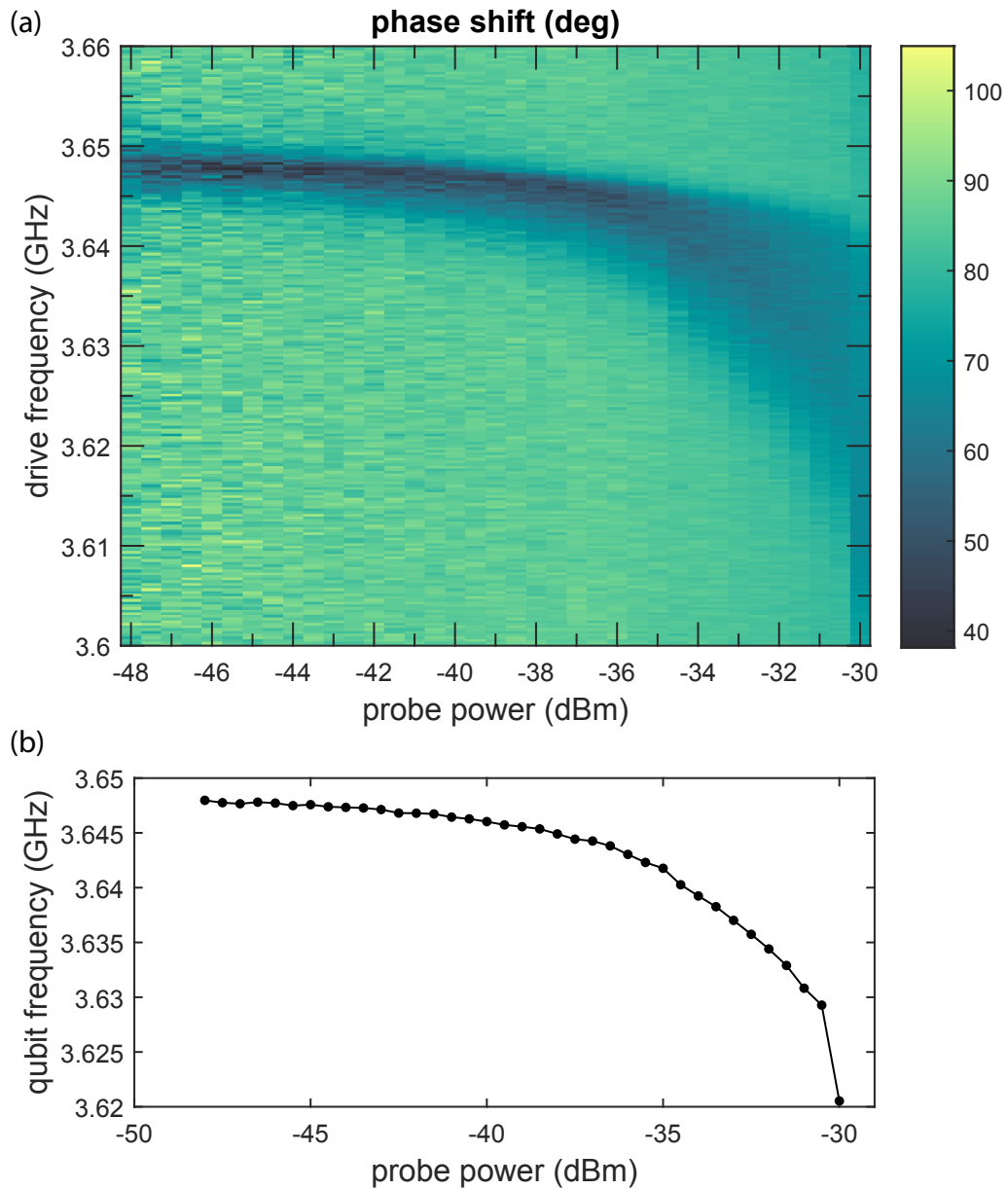


Figure 4.13: (a) Qubit two-tone spectroscopy. Colourscale indicates phase shift ϕ in degrees of the probe signal, at $f_p = 5.4635$ GHz. The reduced phase shift is observed when the drive tone excites the qubit out of the ground state. Increasing the readout power leads to broadening and ac Stark shift of this transition. The drive tone power is -15 dBm. (b) Qubit transition frequency at different readout powers. The data points are obtained from the best fit (Lorentzian or Gaussian) to two-tone spectroscopy data.

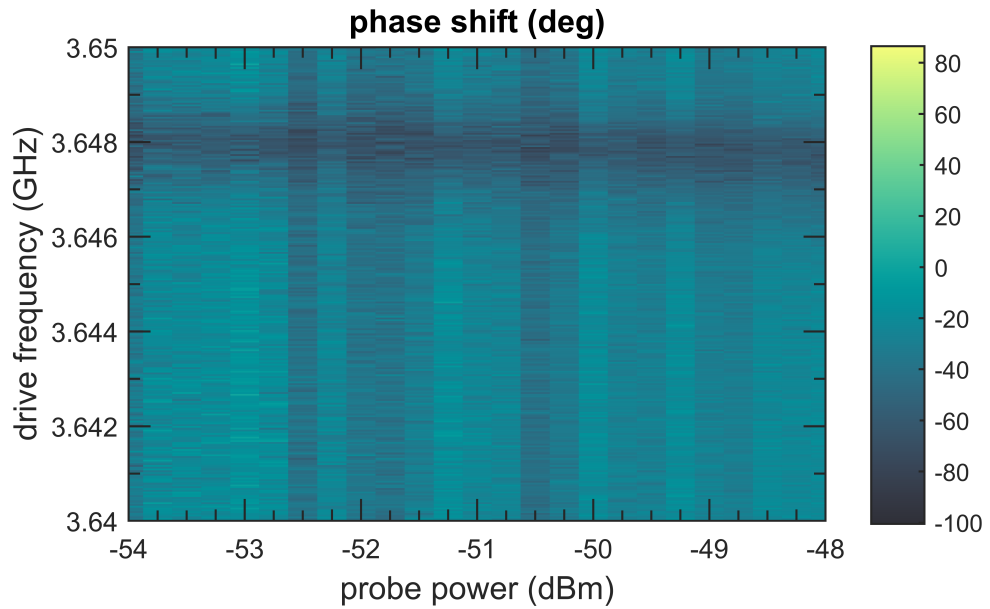


Figure 4.14: Qubit two-tone spectroscopy in the low power limit. Colourscale indicates phase shift ϕ in degrees of the probe signal, at $f_p = 5.4635$ GHz. The drive tone power is -25 dBm.

limit and a time-resolved measurement of relaxation is necessary to determine T_1 .

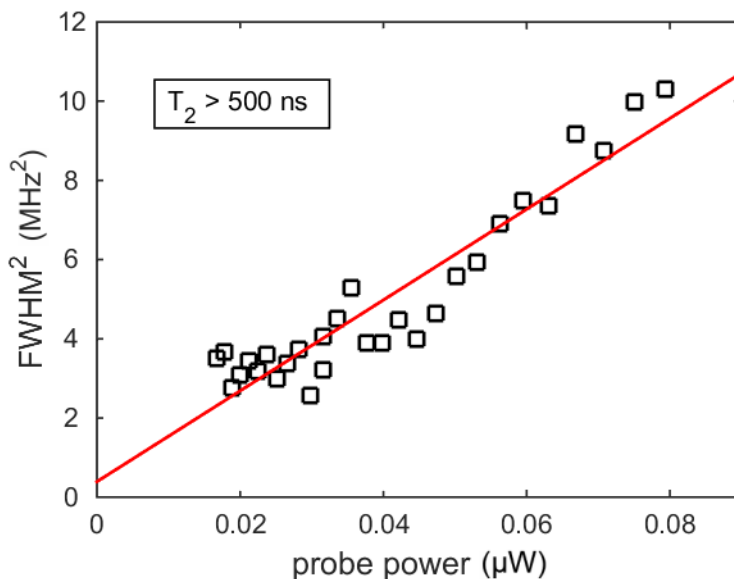


Figure 4.15: Squared qubit linewidth (FWHM) as a function of input power. Linear fit extrapolated to zero power for T_2 estimate.

We now investigate the effect of the drive power on the spectroscopy results. Figure 4.16 plots a sweep of the qubit drive power and frequency, where a -35 dBm readout tone is applied at the ground state cavity frequency. Increased power leads to broadening of the qubit line, and at high powers the E_{12} qubit transition emerges. This transition

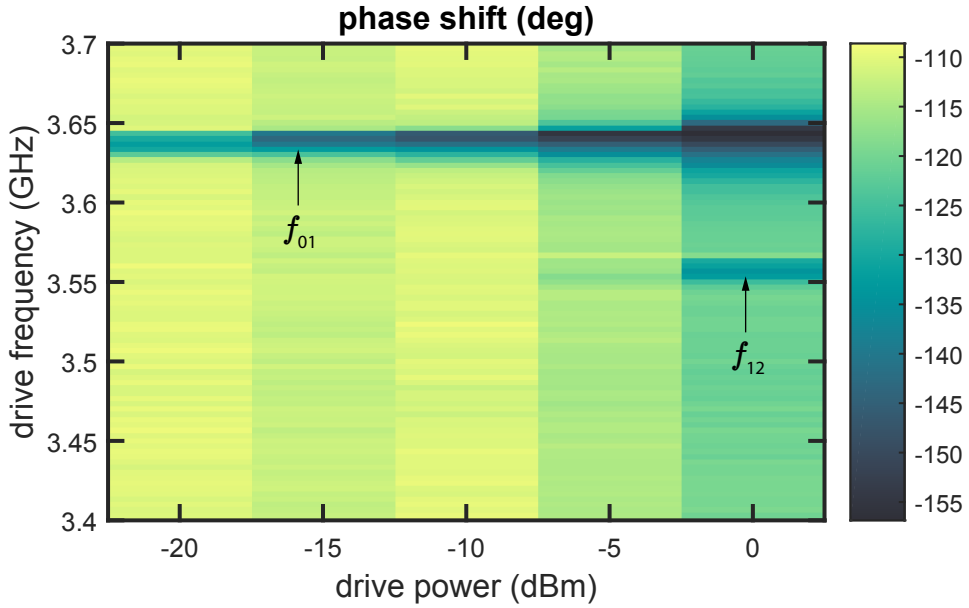


Figure 4.16: Qubit two-tone spectroscopy sweeping the drive power. At high drive powers, it is possible to discern the second qubit transition. The probe power amounts to -35 dBm ($n_p = 2.5$).

reaches the second qubit excited state and is driven by a two-photon process [45]. A large drive signal photon population is therefore critical for this excitation to occur. At a drive

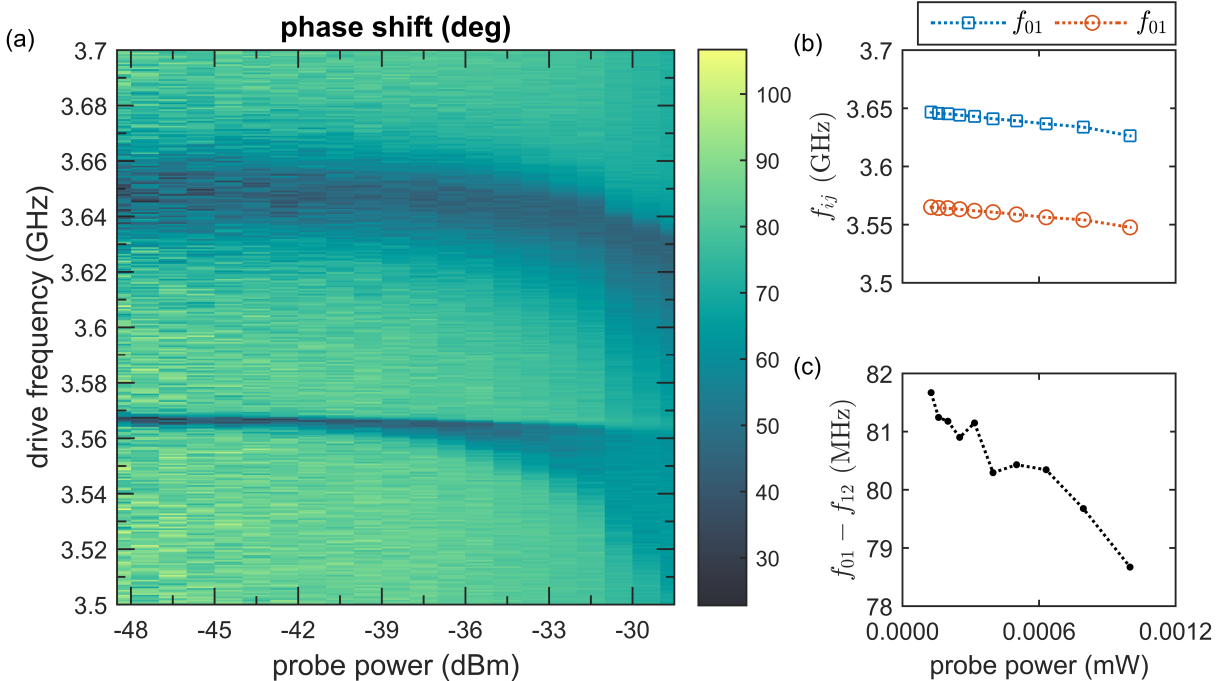


Figure 4.17: (a) Two-tone spectroscopy with strong drive. (b) Frequencies for the first and second transition. (c) Anharmonicity $f_{01} - f_{12}$. The drive power is 5 dBm.

power of 5 dBm, the second level is clearly visible in two-tone spectroscopy, as shown

in Fig. 4.17 (a). This transition has a slightly reduced ac Stark shift due to the larger detuning from the cavity frequency. Figure 4.17 (c) shows the anharmonicity at different probe powers. As expected, the non-uniform ac Stark shift leads to reduced anharmonicity at high probe powers.

In the low power limit, the second transition frequency is found to be $f_{12} = 3.567 \text{ GHz}$. This gives a relative anharmonicity $A_{rel} = (E_{01} - E_{12})/E_{01}$ of 2.2 %. We see that the energy levels have a relatively uniform spacing, which suggests that we are indeed in the large E_J/E_C limit. Solving Eqs. (2.8 - 2.9) for E_C yields $E_C = E_{01} - E_{12}$. This gives an energy ratio $E_J/E_C = 265$ and a total capacitance $C_\Sigma = 239 \text{ fF}$. For the Josephson junction we obtain a critical current $I_c = 43.2 \text{ nA}$. This close resemblance to the harmonic oscillator means also the second excited state could influence the dressed state properties.

4.2.2 High power spectroscopy

In addition to two-tone spectroscopy with a weak readout signal, we also measure the cavity response over broad power ranges without driving the qubit. These experiments are essentially identical to the ones presented in Sec. 4.1.3, the difference being that for the results presented here, the transmon chip is mounted in the cavity. At high readout power, we observe the onset of a strongly transmitted "bright" cavity transmission state corresponding to the bare resonator frequency. From the frequency shift of this state with respect to the dressed cavity resonance, the coupling strength may be calculated.

Figure 4.18 (a) shows a single tone power sweep around the cavity frequency. In the power range $P_p = -20 \text{ dBm}$ to $P_p = -15 \text{ dBm}$, we observe a discontinuous change in the cavity resonance. While the frequency jump is discontinuous, there is a coexistence region where both peaks are visible and gradually changing brightness. The shift amounts to almost 1.2 MHz. Fitting Lorentzians to find the linewidths of the branches, we find that for the upper, low power branch $Q = 2.4 \cdot 10^4$, and for the high power bright state $Q = 3.2 \cdot 10^4$.

Switching the qubit drive on, the features of the upper branch of the cavity resonance changes at high powers. As this branch fades, it splits into two diverging structures, one of which crosses the high power resonant line. When driving close to the qubit frequency, this feature appears more prominently. This is shown in Figures 4.18 (b) and 4.18 (d), where -10 dBm drive tones are applied at 3.65 GHz and 3.58 GHz, respectively. Note that due to the ac Stark shift, 3.58 GHz is closer to the qubit frequency in this case.

If instead of driving the qubit, the drive tone is applied at the frequency of the upper branch, the readout transmission coincides with the lower branch for all readout powers. This is shown in Fig. 4.18 (c). A saturation effect does seem to occur for the upper branch when stimulated with sufficient power. This structure in the cavity spectrum has been observed in previous experiments [46], where the transition to the bare cavity state was shown to exhibit bistability, with the high power cavity response depending on the

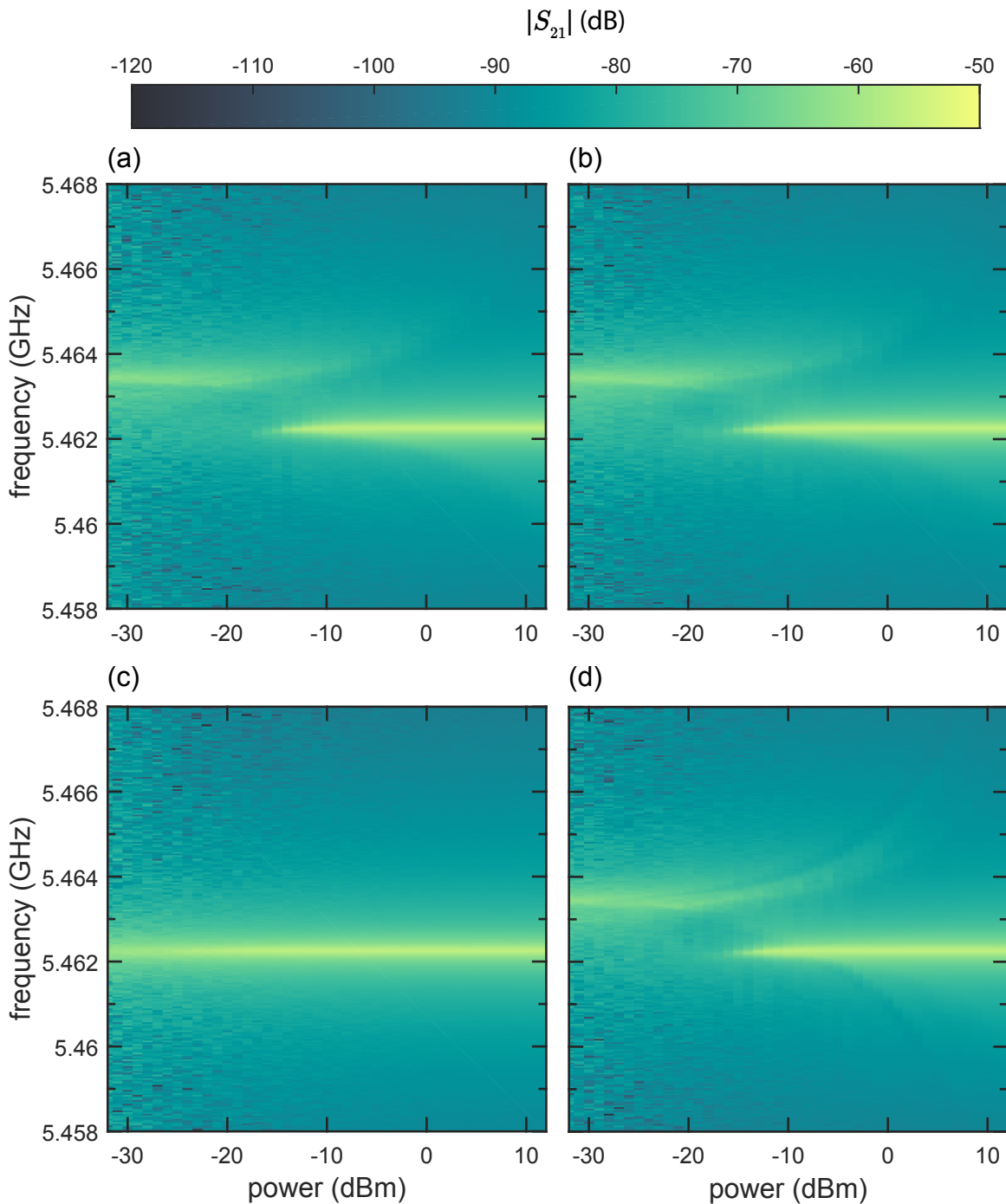


Figure 4.18: (a) Single tone spectroscopy power sweep. At high readout power, the cavity frequency is abruptly downshifted. No qubit drive is applied in this measurement. (b) Two-tone spectroscopy power sweep with -10 dBm drive tone at 3.65 GHz. Due to the ac Stark shift, this drive has a considerable detuning from the first qubit transition. (c) Two-tone spectroscopy power sweep with -10 dBm drive tone at 5.4635 GHz. When driving at the upper branch frequency, the lower branch resonance is observed at all readout powers. (d) Two-tone spectroscopy power sweep with -10 dBm drive tone at 3.58 GHz.

qubit state. The apparent splitting of the upper branch under qubit driving may thus be an effect of significant population of the qubit excited state. As in the high power limit, the frequency response corresponds to the bare resonator, the frequency difference between the branches is given by the dispersive shift. For transmon experiments carried out in [46], as well as the associated theoretical models [47], it is demonstrated that the Jaynes-Cummings Hamiltonian introduced in Eq. (2.22) accounts for the appearance of a bright state shifted by g^2/Δ away from the dressed cavity resonance. A reduced shift due to the influence of the second qubit transition is not observed.

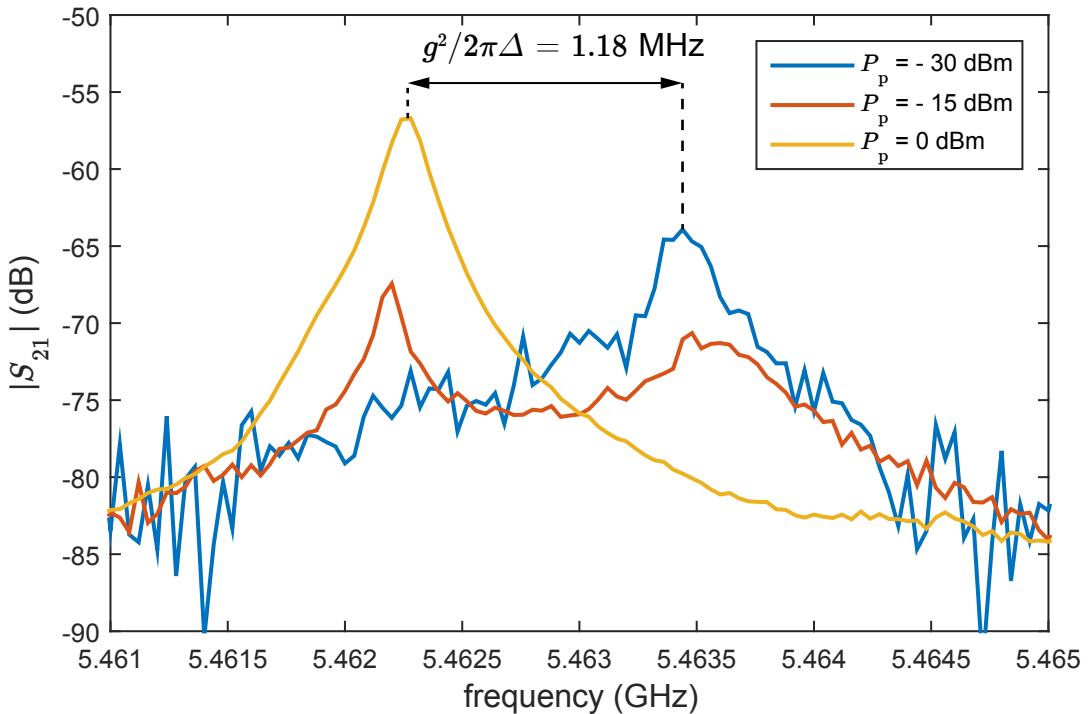


Figure 4.19: Cavity spectra without qubit drive for different readout powers. At $P_p = -15 \text{ dBm}$ ($n_p = 250$), both branches are observed to coexist.

The bare cavity resonance frequency is found at $f_{\text{bare}} = 5.4623 \text{ GHz}$. This is lower than the resonance measured in Sec. 4.1.3 only due to the effect of the dielectric silicon wafer. Figure 4.19 shows the transmission spectrum without qubit drive at selected readout powers. We take the frequency difference in the cavity resonances between the high and low power limits to equal g^2/Δ . Calculating the detuning between the bare resonator f_{bare} and the bare qubit frequency $\omega_q/2\pi$ from Eq. (2.24), we obtain the coupling strength $g/2\pi = 46.4 \text{ MHz}$. As this frequency exceeds both the decay rate and cavity loss rate by at least one order of magnitude, we are well into the strong coupling regime ($g \gg \kappa, \Gamma$).

In addition to spectroscopy carried out with the pins inserted deeply into the cavity volume (1.4 mm), we also measure the cavity with the qubit in a retracted pin (-1.6 mm) configuration. This data also shows a high power bright state, with a shift of the same

magnitude as recorded here.

Simulation estimate of the coupling strength

We use a CST simulation to provide an estimate of the coupling strength g from electrodynamics. With a CST model of the cavity with the transmon chip inserted, we obtain the field values at the resonance frequency. We then numerically integrate to evaluate the mode volume (cf. Eq. (2.35)) and obtain $V_{mode}/(abd) = 0.258$. The dielectric properties of the wafer along with the wall curvature causes the slight mode volume increase as compared to the rectangular cavity analytical value of $1/4$. The dipole moment μ arises

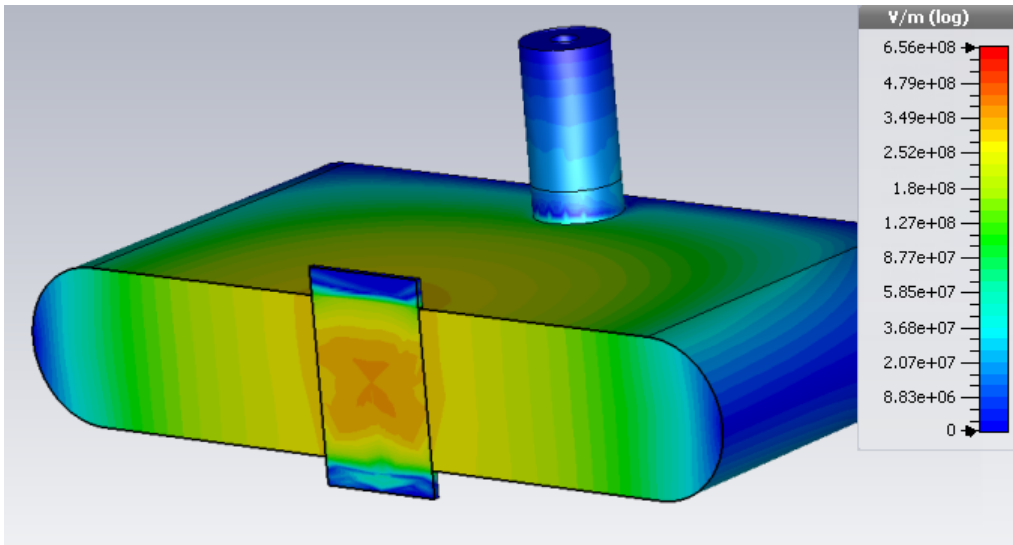


Figure 4.20: Cavity model with transmon mounted in the experimental configuration. The image shows the electric field distribution for one half of the cavity, with the cut through the transmon wafer. The simulated input power is 1 W and the pin depth 1.4 mm.

from charge transfer across the qubit junction. We estimate it by fixing the amount of net charge on either pad to $+2e$ and $-2e$ respectively, and assuming uniform charge distribution across the pads. Together with the calculated mode volume and RMS field of Eq. (2.35), this yields a coupling of $g/2\pi = 52.5$ MHz. This value is only slightly greater than the measured result from Sec. 4.2.4. Several reasons may be identified as to why the values differ. The calculation assumes optimal qubit positioning with respect to the electric field, something which is difficult to realize in practice. We also make a simplified assumption with respect to the distribution of excess charge across the structure. Considering the complexity of the electrodynamic geometry, the estimation is still very close to the measured value and the procedure useful to qubit design.

4.2.3 ac Stark shift and photon number calibration

The coupling strength value g and the ac Stark shift of the qubit can be combined to calibrate the photon number in the cavity. This is how previously stated n_p values have been obtained. As given by Eq. (2.24), the qubit frequency is a linear function of the photon number with a slope of $2g^2/\Delta$. We now use the coupling strength obtained above (cf. Sec. 4.2.2) to calibrate the spectroscopy photon population of the cavity. A qubit frequency $\omega_{q,1ph} = \omega_{q,0} - 2g^2/\Delta$ corresponds to a single cavity photon ($n_p = 1$), if $\omega_{q,0}$ is the dressed qubit frequency in the low power limit. We analyse the two-tone spectroscopy data (cf. Fig. 4.13) to find the probe power P_p at which the qubit frequency reaches $\omega_{q,1ph}$. This calibration gives the single photon probe power at the VNA of -39 dBm. At single photon population, the cavity energy loss rate amounts to

$$P_{cl} = \hbar\omega\kappa/2\pi. \quad (4.14)$$

$\kappa/2\pi = f_r/Q$ is the cavity loss rate per photon. With a Q of $2.4 \cdot 10^4$, we get $\kappa/2\pi \approx 230$ kHz. Comparing P_{cl} with the probe power, we are able to determine the losses in the input lines. Including the 20 dB attenuator at room temperature and reflection at the cavity input, these amount to 110 dB.

Using the calibration from above and the transitions frequencies of Fig. 4.13 (a), we plot the qubit frequency vs. photon number in Fig. 4.21 to confirm that the slope of the ac Stark shift is consistent with the obtained value for the coupling strength g . As is evident in Fig. 4.21, qubit frequencies measured at photon populations $n_p > 2.5$ deviate from the estimate derived from the coupling strength to a greater extend than the low-power limit data. This is due to the fact that the Lorentzian or Gaussian lineshape fitting is less accurate at higher power, where the qubit transition is broadened and not perfectly symmetric. Fitting a line to the qubit frequency, restricting the fit to values where $n_p < 2.5$, we obtain a coupling $g_{fit}/2\pi = 49.3$ MHz. This value is slightly less than 7 % higher than the coupling obtained from the shift between the bare and dressed cavity resonances observed in high power spectroscopy. Considering the noise level in the qubit spectroscopy data (cf. Fig. 4.12), we conclude that the magnitude of the ac Stark shift of the qubit is consistent with the parameters obtained from the dispersive shift. The measured results are best explained using the highly simplified Jaynes-Cummings model, even though there is reason to believe the dynamics would be better represented by models accounting for the transmon level structure in more detail. This has turned out to be the case also for other experiments coupling transmons to resonator structures [48].

4.2.4 Dressed cavity transmission spectrum

We now record the cavity spectrum at low readout power with a frequency sweep of the qubit drive. We observe clearly the change in cavity response when the system is

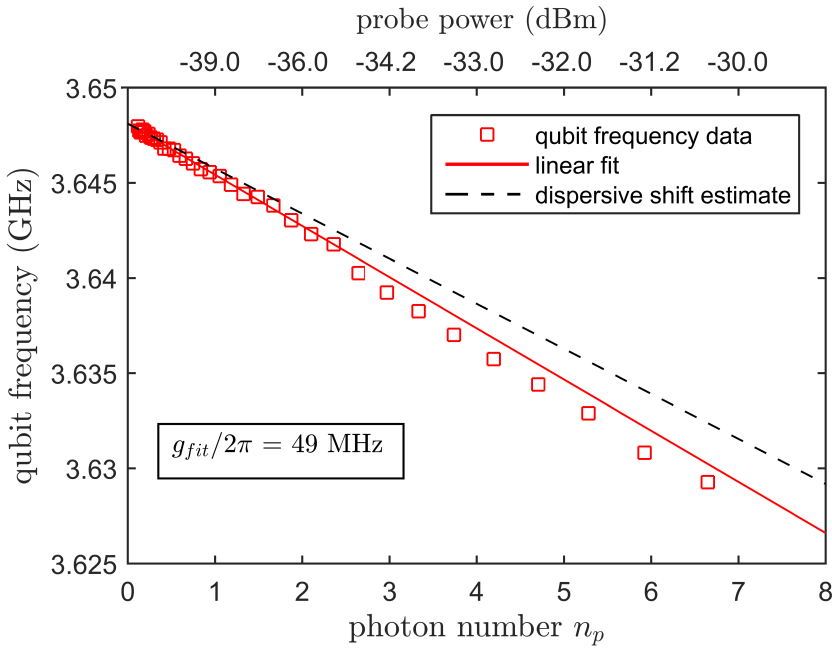


Figure 4.21: Qubit frequency vs. readout photon population in the cavity. The photon number calibration is obtained by comparing qubit frequency data (red boxes) to the ac Stark shift estimated from the coupling strength calculated from the dispersive shift in Sec. 4.2.2. This estimated ac Stark shift (black dotted line) is plotted for comparison. Fitting a line to the qubit frequency (red line) gives an additional estimate g_{fit} for the coupling strength. The fit is restricted to data below $n_p = 2.5$.

driven close to the qubit frequency. Figure 4.22 shows such a two-tone frequency sweep performed with readout power $P_p = -40$ dBm. Fitting Lorentzian curves to the cavity transmission, we observe a decrease in the qubit-induced shift for increased probe powers. This is plotted in Fig. 4.23.

In general, the observed shifts are much smaller than the dispersive shift of the cavity as observed from the onset of the bright state at high probe powers, and do not exceed 200 kHz. From the Hamiltonian of Eq. (2.23), driving the qubit from the ground state into a mixed state where $\langle \sigma_z \rangle = 0$ should shift the cavity resonance frequency by $g^2/2\pi\Delta$. This description relies on the two-level approximation and assumes no higher transitions of the qubit are involved. The low anharmonicity of the transmon may therefore explain the small effect on the cavity response from driving the qubit. As an increased probe power leads to broadening of the qubit transitions and further reduced anharmonicity, the reduced shift at higher P_p may be due to stronger influence of higher qubit levels. At probe powers above -30 dBm, the shift vanishes almost completely. This is also the reason why we rely on the bright state shift in the high power limit for calculating g and calibrating the cavity photon number.

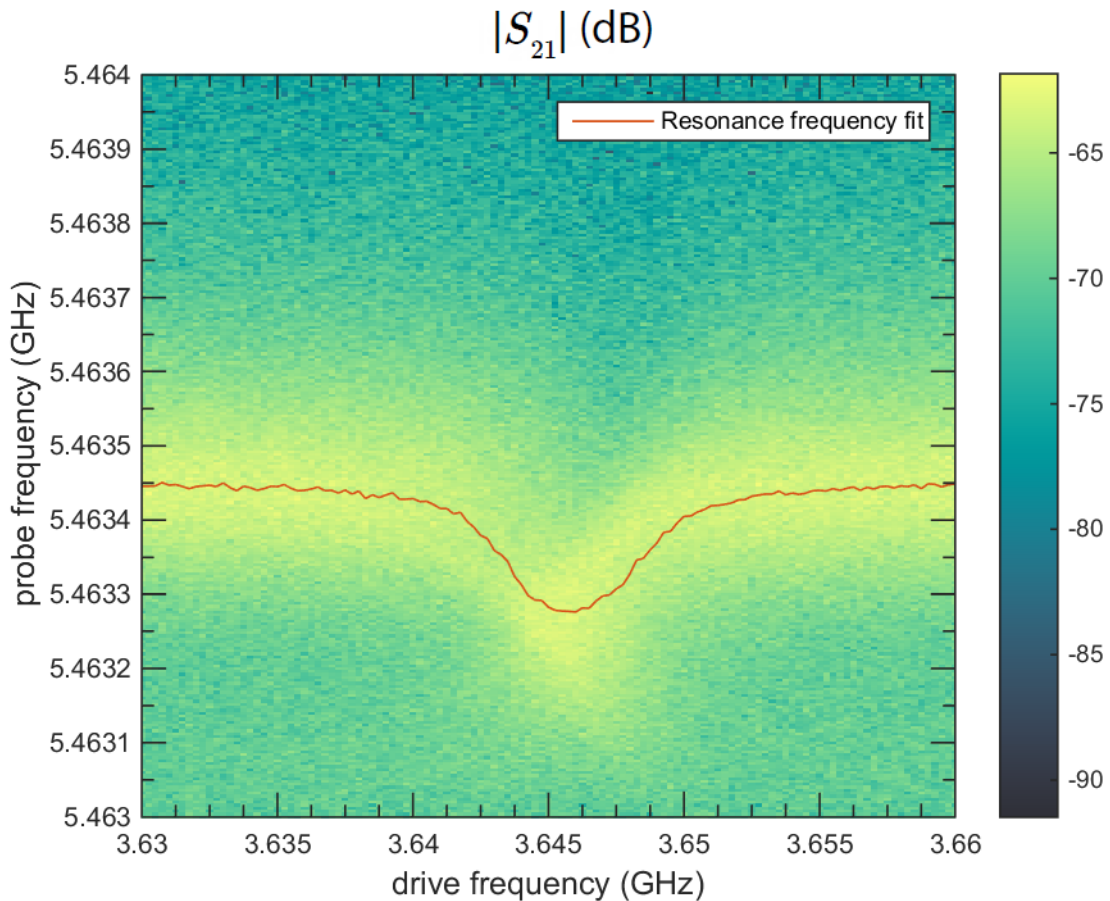


Figure 4.22: Qubit two-tone spectroscopy. Both the drive and readout frequencies are varied in order to observe the effect on the cavity resonance. Colourscale indicates transmission. The resonance frequencies (red line) are obtained by Lorentzian fit, and show a shift when driving at the qubit frequency.

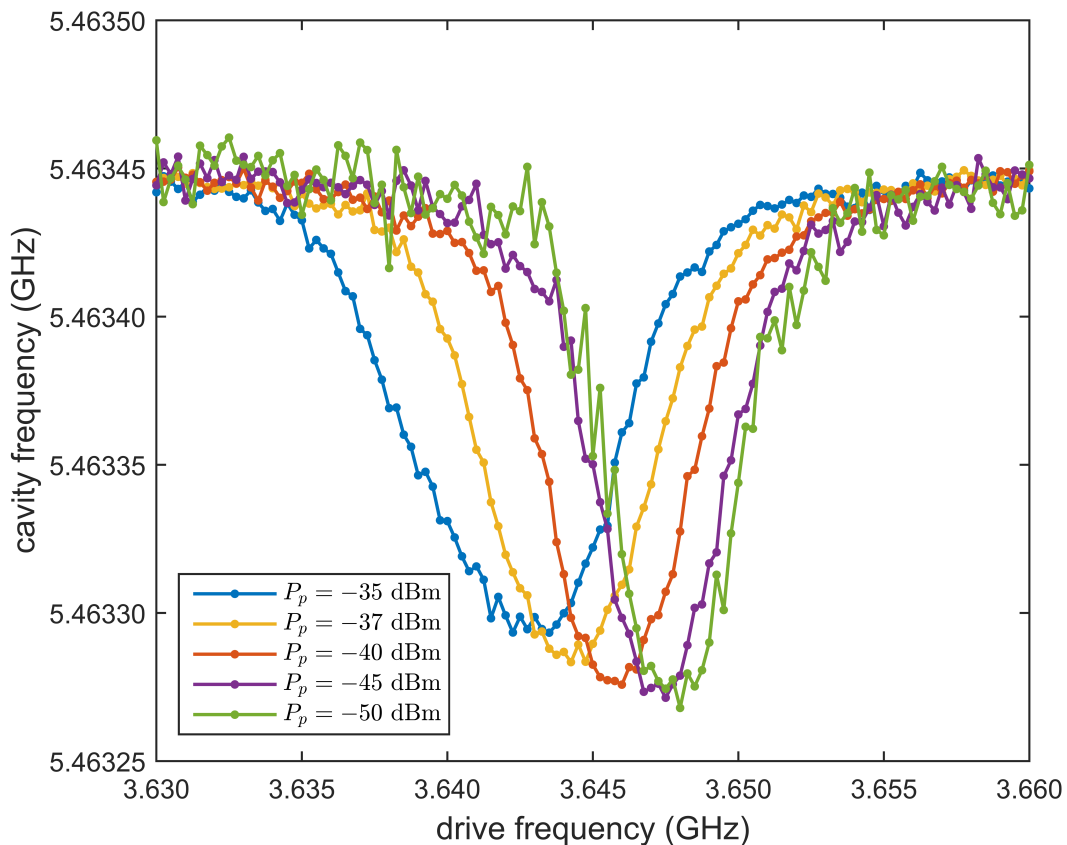


Figure 4.23: Dressed cavity frequency as a function of qubit drive frequency and readout power. The cavity frequency minima occur at different drive frequencies due to the ac Stark shift of the qubit. The drive power is -10 dBm .

Chapter 5

Conclusions and outlook

The main purpose of this thesis is the experimental characterization of the interaction of a transmon qubit with a 3D cavity. Microwave measurement techniques are the main tool, complemented by numerical analysis.

The cavity transmission has been characterized at room temperature and a frequency tuning schemes have been developed and evaluated. We have investigated the superconducting cavity properties and observed an internal quality factor of the order of 10^6 for the pure aluminium cavity. The quality factor has been shown to be independent of the transmitted power. The unperturbed resonant frequency of the alloy and pure aluminium cavities at 50 mK was found to be 5.715 GHz and 5.718 GHz, respectively.

We have then shown the functional operation of a transmon qubit coupled to this high quality resonator in a 3D architecture. The bare qubit frequency is determined to be 3.649 GHz. The ac Stark shift of the qubit is measured and the response of the cavity is characterized in terms of the dispersive shift. From the linewidth of the qubit transition, we estimate the dephasing time T_2 to be in excess of 500 ns. From the second qubit transition, we find the anharmonicity to be 2.2 % and determine the energies E_C and E_J . We demonstrate strong coupling of the transmon to the cavity field, with a coupling strength $g/2\pi$ of 46.4 MHz. The onset of a bright cavity transmission state at high readout powers has been observed and used to derive the coupling strength.

This analysis represents the first steps towards more complex quantum information processing experiments involving 3D resonator networks. Numerical modelling and simulations have been developed to that end, showing a promising route forward for this project. In the following we will review the outlook of immediate future steps to be taken.

To verify the coupling strength figure and determine the coherence times T_1 and T_2 , an important next step for the project is to perform time-resolved qubit measurements. Time domain measurements are commonplace in circuit QED, as they allow controlled qubit rotations on the Bloch sphere and, in an averaged picture, characterization of the time evolution of excited qubit and cavity states. This is done via driven Rabi oscillation experiments [49] [50]. Such a measurement procedure is carried out by sending drive pulses that generate well defined rotations of the qubit state on the Bloch sphere.

As part of this thesis, work towards implementing such a setup has been made. This

effort is facilitated by setup schemes and software development made previously at the WMI for propagating microwave experiments [51]. For real time data acquisition, we use an Agilent Acqiris digitizer capable of recording 420 megasamples per second. The GHz-regime frequency of the output signal therefore has to be downconverted through local oscillator mixing. A data timing generator (DTG) is used to trigger microwave drive signal output and data acquisition. During this thesis, a test setup including the acqiris digitizer, a DTG and a waveform generator as a test signal has been configured and verified to function. A suitable next step for the project involves the completion and testing of the setup, outlined in more detail in Appendix C.

At the time of writing, a double cavity sample is scheduled for fabrication in the WMI workshop. The design is based in part on analysis of a two cavity system performed in this thesis. With this setup, it should be possible to observe entangled single photon states present in both cavities simultaneously. The generation of such non-local entangled states is set to benefit from a frequency-degenerate design, so that the photon frequency coincides with the eigenmode of both cavities. The idea is to compensate for fabrication imprecisions by some means of frequency tuning, as outlined in Sec. 4.1.2.

The filter bias line designed should be possible to fabricate using standard optical lithographic methods. This paves the way for implementing a tunable transmon in a two cavity setup. The qubit-mediated coupling between the cavities is then controllable in situ, potentially leading to quantum mechanical switching behaviour as the flux bias is varied. Figure 5.1 shows the CAD design of the two cavity geometry, with slits for a transmon wafer and flux bias line. While the most straightforward extension to two cavities, this model may not be optimal for scaling beyond that. For a 3D resonator network, we are considering an architecture where the top cavity is displaced by half its length relative to the bottom cavity. That would require the transmons to couple to the second mode to connect the cavities, but enable scaling to a resonator chain by duplicating the same structure multiple times.

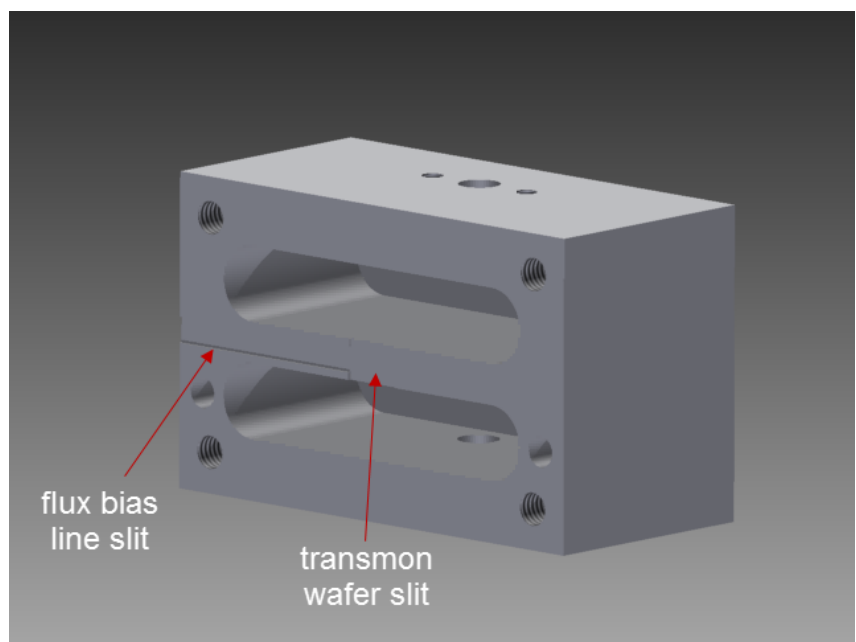


Figure 5.1: Rendered image of CAD drawing of the two-cavity concept. The dimensions are those of the simulated 3D model.

Appendix A

Dual cavity measurement

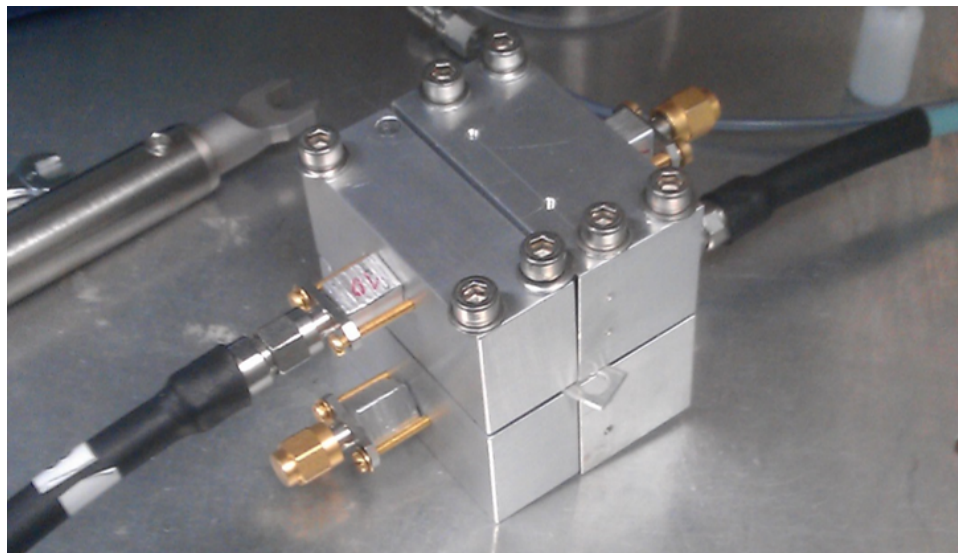


Figure A.1: Dual cavity cross-transmission measurement arrangement.

As a preliminary analysis of scaling possibilities, we measure the transmission between the cavities at room temperature, coupled only by a gap between the two pieces of each cavity. The purpose is to investigate the cross-transmission between the cavities due only to a connecting opening in the cavity center. In an ideal resonator network, the only cavity-cavity coupling is provided by bridge transmons. We therefore seek to minimize cross-transmission arising out of the resonator geometry.

In [37], the alloy cavity transmission has been measured with such a gap without significant effect on the quality factor. The cavity setup is shown in Fig.A.1.

We observe no propagation of the first mode between the cavities. This is consistent with the finding that a resonator with a gap between the two halves preserves total Q . However, the second mode does exhibit considerable cross-transmission. This is most clearly visible in the retracted pin limit. Figure A.2 shows the cross-transmission amplitude for pin depths close to -2 mm . We also observe a smaller peak next to the second mode, possibly corresponding to some additional mode present due to the enlarged total resonant volume.

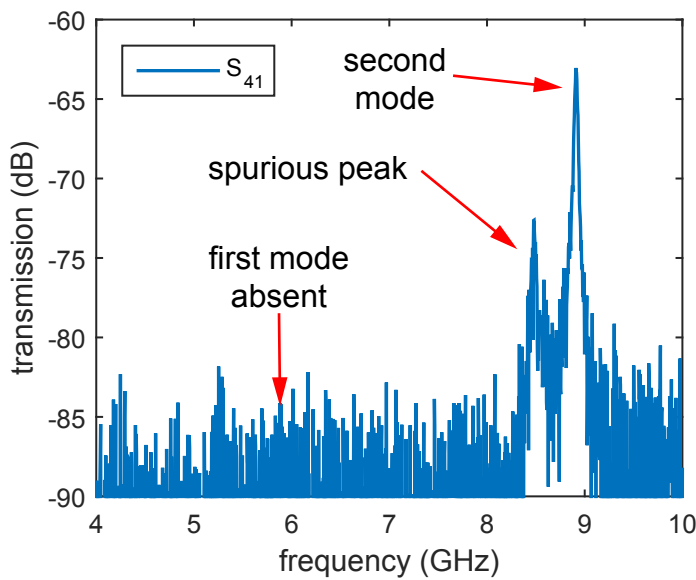


Figure A.2: Cavity cross-transmission measured in a configuration mounting both cavities together. The measurement power is -10 dBm . While the first mode shows no cross-transmission between the cavities, the second mode is observed clearly. Close to the second mode, we see a spurious resonant structure.

The second mode has a magnetic field antinode at the gap position in the cavity centre, allowing inductive coupling of this mode between the cavities. For the fundamental mode with a magnetic field node at this position, the coupling is suppressed.

Appendix B

Cavity technical data

Alloy contents

The EN AW-2007 alloy used to fabricate the alloy cavity has the following contents:

Alloy component	Content (%)
Al	88 – 93
Cu	3.3 – 46
Mg	< 1.8
Pb	< 1.5
Fe	0.8
Si	0.8
Zn	0.8
Ni	0.2
Ti	0.2
Cr	0.1

Detailed electropolishing result

Below we present the full results of electropolishing for the alloy cavity. Mesurement scans were done for one cavity half prior to treatment, and both pieces after. The amplitude parameters are described in [52], with the average roughness R_a being the most widely used. Position 1 refers to the curved side where milling traces are visible. Positions 2 and 3 are located on the flat surface where the milling was more effective.

Before electropolish			
parameter	pos 1 (μm)	pos 2 (μm)	pos 3 (μm)
R_a	1.280	0.295	0.330
R_z	5.293	1.664	2.530
R_{max}	5.622	2.106	3.580
Electropolished piece 1			
parameter	pos 1 (μm)	pos 2 (μm)	pos 3 (μm)
R_a	0.978	0.627	0.719
R_z	7.095	4.818	5.990
R_{max}	9.320	7.672	7.801
Electropolished piece 2			
parameter	pos 1 (μm)	pos 2 (μm)	pos 3 (μm)
R_a	0.714	0.670	0.884
R_z	5.842	5.228	6.829
R_{max}	9.430	7.215	8.856

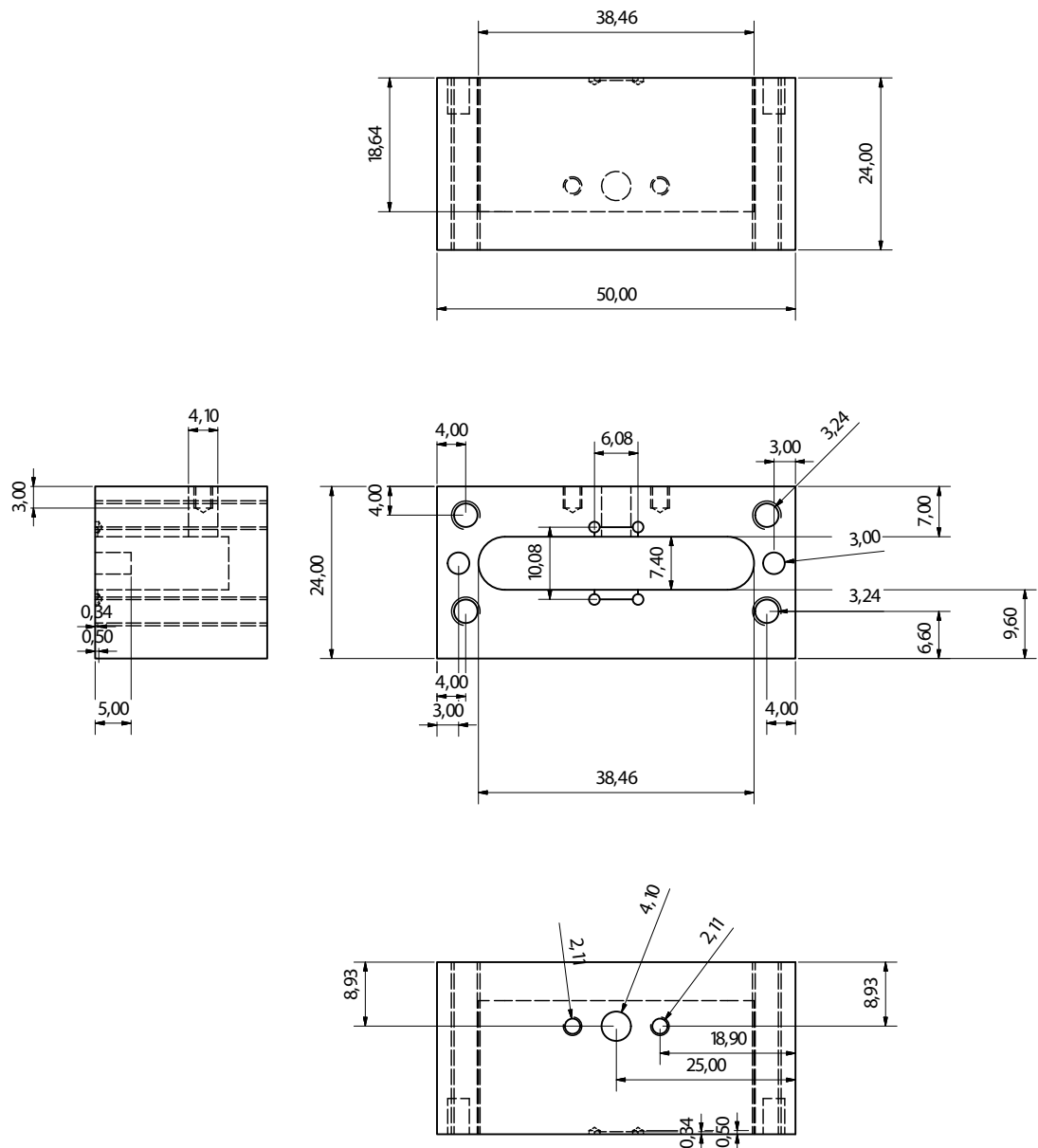


Figure B.1: Technical drawings of the alloy cavity as used by the workshop. The pure aluminium cavity has identical internal dimensions and differs only in the thickness of the metal walls.

Appendix C

Time domain setup

The circuit diagram for the time domain measurement setup under development is shown in Fig. C.1.

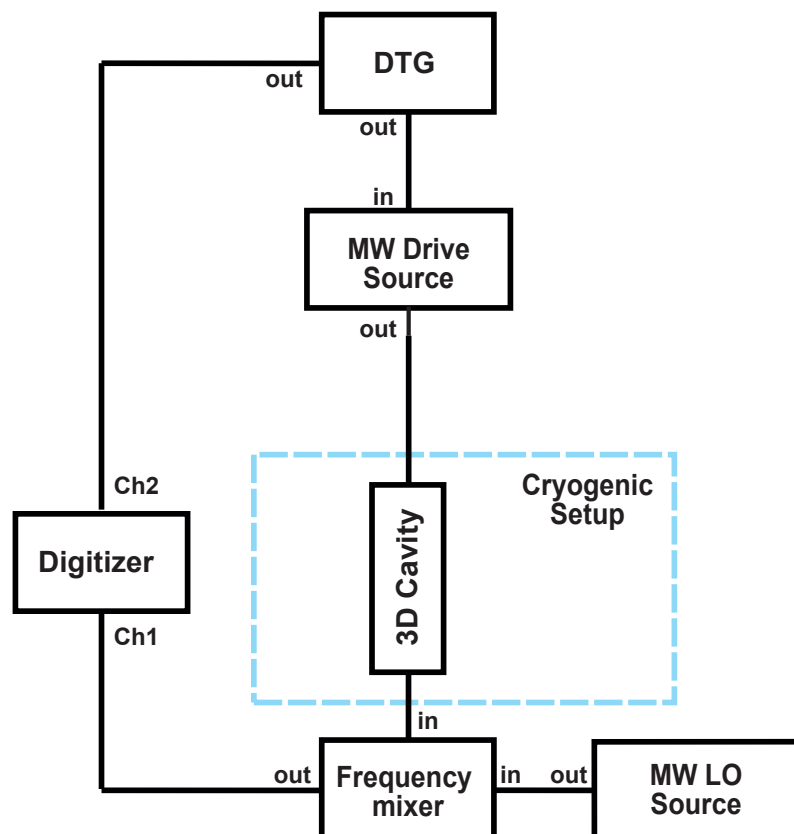


Figure C.1: Circuit diagram of the planned time domain measurement setup. The cryogenic part has been left out in this picture.

Bibliography

- [1] P. Shor, “Polynomial-Time Algorithms for Prime Factorization and Discrete Logarithms on a Quantum Computer”, arXiv:quant-ph (1996).
- [2] M. H. Devoret and R. J. Schoelkopf, “Superconducting Circuits for Quantum Information: An Outlook”, *Science* **339**, 1169 (2013).
- [3] J. Koch, T. M. Yu, J. Gambetta, A. A. Houck, D. I. Schuster, J. Majer, A. Blais, M. H. Devoret, S. M. Girvin, and R. J. Schoelkopf, “Charge-insensitive qubit design derived from the Cooper pair box”, *Phys. Rev. A* **76**, 486 (2007).
- [4] C. Rigetti, J. M. Gambetta, S. Poletto, B. L. T. Plourde, J. M. Chow, A. D. Córcoles, J. A. Smolin, S. T. Merkel, J. R. Rozen, G. A. Keefe, M. B. Rothwell, M. B. Ketchen, and M. Steffen, “Superconducting qubit in a waveguide cavity with a coherence time approaching 0.1 ms”, *Phys. Rev. B* **86**, 100506 (2012).
- [5] T. Orlando and K. Delin, *Foundations of Applied Superconductivity*, Electrical Engineering Series (Addison-Wesley, 1991), ISBN 9780201183238, URL <http://books.google.se/books?id=7yRRAAAAMAAJ>.
- [6] J. Bardeen, L. N. Cooper, and J. R. Schrieffer, “Theory of Superconductivity”, *Phys. Rev.* **108**, 1175 (1957).
- [7] B. Josephson, “Possible new effects in superconductive tunnelling”, *Phys. Lett.* **1**, 251 (1962).
- [8] R. Gross and A. Marx, *Applied Superconductivity: Josephson Effect and Superconducting Electronics* (2005), lecture notes.
- [9] M. Tinkham, *Introduction to Superconductivity* (1996).
- [10] S. Dürr, “Ultrakalte Quantengase 1”, (2013), lecture notes.
- [11] A. Cottet, “Implementation of a quantum bit in a superconducting circuit”, Ph.D. Thesis (2002).
- [12] J. R. Johansson, P. Nation, and F. Nori, “QuTiP 2: A Python framework for the dynamics of open quantum systems”, *Comp. Phys. Comm.* **184** (2013).

- [13] J. D. Strand, M. Ware, F. Beaudoin, T. A. Ohki, B. R. Johnson, A. Blais, and B. L. T. Plourde, “First-order sideband transitions with flux-driven asymmetric transmon qubits”, *Phys. Rev. B* **87**, 220505 (2013).
- [14] D. Pozar, *Microwave Engineering, Quantum Physics of Atoms, Molecules, Solids, Nuclei and Particles* (Wiley, 1985), ISBN 978-0-470-63155-3.
- [15] B. Aune, R. Bandelmann, D. Bloess, B. Bonin, A. Bosotti, M. Champion, C. Crawford, G. Deppe, B. Dwersteg, D. A. Edwards, H. T. Edwards, M. Ferrario, M. Fouaidy, P.-D. Gall, A. Gamp, A. Gössel, J. Graber, D. Hubert, M. Hüning, M. Juillard, T. Junquera, H. Kaiser, G. Kreps, M. Kuchnir, R. Lange, M. Leenen, M. Liepe, L. Lilje, A. Mathiesen, W.-D. Möller, A. Mosnier, H. Padamsee, C. Pagani, M. Pekeler, H.-B. Peters, O. Peters, D. Proch, K. Rehlich, D. Reschke, H. Safa, T. Schilcher, P. Schmüser, J. Sekutowicz, S. Simrock, W. Singer, M. Tigner, D. Trines, K. Twarowski, G. Weichert, J. Weisend, J. Wojtkiewicz, S. Wolff, and K. Zapfe, “Superconducting TESLA cavities”, *Phys. Rev. ST Accel. Beams* **3**, 092001 (2000).
- [16] D. Bogorin, M. Ware, D. McClure, S. Sorokanich, and B. Plourde, “Reducing surface loss in 3D microwave copper cavities for superconducting transmon qubits”, *Superconductive Electronics Conference (ISEC)* (2013).
- [17] M. Kummer, *Grundlagen der Mikrowellentechnik* (1989).
- [18] R. Miller, T. E. Northup, K. M. Birnbaum, A. Boca, A. D. Boozer, and H. J. Kimble, “Trapped atoms in cavity QED: coupling quantized light and matter”, *Journal of Physics B: Atomic, Molecular and Optical Physics* **38**, S551 (2005).
- [19] S. Haroche, “Controlling photons in a box and exploring the quantum to classical boundary”, (2012), nobel Lecture, URL http://www.nobelprize.org/nobel_prizes/physics/laureates/2012/.
- [20] J. Sakurai and J. Napolitano, *Modern Quantum Mechanics* (Addison-Wesley, 2011), ISBN 9780805382914, URL <http://books.google.de/books?id=N4I-AQAACAAJ>.
- [21] G. Lindblad, “On the generators of quantum dynamical semigroups”, *Communications in Mathematical Physics* **48**, 119 (1976).
- [22] A. Rivas and S. F. Huelga, *Open Quantum Systems* (2012).
- [23] A. Blais, R.-S. Huang, A. Wallraff, S. M. Girvin, and R. J. Schoelkopf, “Cavity quantum electrodynamics for superconducting electrical circuits: An architecture for quantum computation”, *Phys. Rev. A* **69**, 062320 (2004).
- [24] M. O. Scully and M. S. Zubairy, *Quantum Optics* (Cambridge University Press, 1997), ISBN 978-0521435956.

- [25] E. M. Purcell, “Proceedings of the American Physical Society”, *Phys. Rev.* **69**, 674 (1946).
- [26] H. Paik, D. I. Schuster, L. S. Bishop, G. Kirchmair, G. Catelani, A. P. Sears, B. R. Johnson, M. J. Reagor, L. Frunzio, L. I. Glazman, S. M. Girvin, M. H. Devoret, and R. J. Schoelkopf, “Observation of High Coherence in Josephson Junction Qubits Measured in a Three-Dimensional Circuit QED Architecture”, *Phys. Rev. Lett.* **107** (2011).
- [27] C. Cohen-Tannoudj, J. Dupont-Roc, and G. Grynberg, *Photons and Atoms: Introduction to Quantum Electrodynamics* (Wiley, 1997), ISBN 978-0-471-18433-1.
- [28] Product description, URL <http://www.ni.com/labview/>.
- [29] G. Dolan, “Offset masks for lift-off photoprocessing”, *Appl. Phys. Lett.* **31** (1977).
- [30] E. Xie, “Optimized fabrication process for nanoscale Josephson junctions used in superconducting quantum circuits”, Master’s thesis, Technische Universität München (2013).
- [31] E. Hoffmann, “Investigations of the surface resistance of superconducting materials”, Ph.D. Thesis (2013).
- [32] T. Rylander and P. Ingelström, *Computational Electromagnetics* (Springer, 2013), ISBN 978-1-4614-5350-5.
- [33] M. Mariantoni, F. Deppe, A. Marx, R. Gross, F. K. Wilhelm, and E. Solano, “Two-resonator circuit QED: A superconducting quantum switch”, *Phys. Rev. B* **78** (2008).
- [34] M. D. Reed, “Entanglement and Quantum Error Correction with Superconducting Qubits”, Ph.D. Thesis (2013).
- [35] A. A. Houck, J. A. Schreier, B. R. Johnson, J. M. Chow, J. Koch, J. M. Gambetta, D. I. Schuster, L. Frunzio, M. H. Devoret, S. M. Girvin, and R. J. Schoelkopf, “Controlling the Spontaneous Emission of a Superconducting Transmon Qubit”, *Phys. Rev. Lett.* **101** (2008).
- [36] M. D. Reed, B. R. Johnson, A. A. Houck, L. DiCarlo, J. M. Chow, D. I. Schuster, L. Frunzio, and R. J. Schoelkopf, “Fast Reset and Suppressing Spontaneous Emission of a Superconducting Qubit”, *Appl. Phys. Lett.* **96** (2010).
- [37] J. Müller, “3D Cavities for Circuit Quantum Electrodynamics”, Master’s thesis, Technische Universitaet Muenchen (2014).
- [38] T. Junginger, “Investigations of the surface resistance of superconducting materials”, Ph.D. Thesis (2012).

- [39] C. M. Quintana, A. Megrant, Z. Chen, A. Dunsworth, B. Chiaro, R. Barends, B. Campbell, Y. Chen, I.-C. Hoi, E. Jeffrey, J. Kelly, J. Y. Mutus, P. J. J. O’Malley, C. Neill, P. Roushan, D. Sank, A. Vainsencher, J. Wenner, T. C. White, A. N. Cleland, and J. M. Martinis, “Characterization and reduction of microfabrication-induced decoherence in superconducting quantum circuits”, *Appl. Phys. Lett.* **105**, 062601 (2014).
- [40] D. P. Pappas, M. R. Vissers, D. S. Wisbey, J. S. Kline, and J. Gao, “Two Level System Loss in Superconducting Microwave Resonators”, *Applied Superconductivity* **21**, 871 (2011).
- [41] D. I. Schuster, A. Wallraff, A. Blais, L. Frunzio, R.-S. Huang, J. Majer, S. M. Girvin, and R. J. Schoelkopf, “ac Stark Shift and Dephasing of a Superconducting Qubit Strongly Coupled to a Cavity Field”, *Phys. Rev. Lett.* **94** (2005).
- [42] A. Abragam, *The Principles of Nuclear Magnetism* (1961).
- [43] H. Yokoyama and K. Ujihara, *Spontaneous Emission and Laser Oscillation in Microcavities* (CRC Press, 1995), ISBN 0-8493-3786-0.
- [44] A. P. Sears, A. Petrenko, G. Catelani, L. Sun, H. Paik, L. I. G. G. Kirchmai and, L. Frunzio, S. M. Girvin, and R. J. Schoelkopf, “Photon Shot Noise Dephasing in the Strong-Dispersive Limit of Circuit QED”, *Phys. Rev. B.* **86** (2012).
- [45] L. S. Bishop, J. M. Chow, J. Koch, M. H. Devoret, E. Thuneberg, S. M. Girvin, and R. J. Schoelkopf, “Nonlinear response of the vacuum Rabi resonance”, *Nature Physics* **5** (2008).
- [46] M. D. Reed, L. DiCarlo, B. R. Johnson, L. Sun, D. I. Schuster, L. Frunzio, and R. J. Schoelkopf, “High-Fidelity Readout in Circuit Quantum Electrodynamics Using the Jaynes-Cummings Nonlinearity”, *Phys. Rev. Lett.* **105**, 173601 (2010).
- [47] L. S. Bishop, E. Ginossar, and S. M. Girvin, “Response of the Strongly Driven Jaynes-Cummings Oscillator”, *Phys. Rev. Lett.* **105**, 100505 (2010).
- [48] D. I. Schuster, A. A. Houck, J. A. Schreier, A. Wallraff, J. M. Gambetta, A. Blais, L. Frunzio, J. Majer, B. Johnson, M. H. Devoret, S. M. Girvin, and R. J. Schoelkopf, “Resolving photon number states in a superconducting circuit”, *Nature* **445** (2007).
- [49] L. Henriet, Z. Ristivojevic, P. P. Orth, and K. L. Hur, “Quantum dynamics of the driven and dissipative Rabi model”, *Phys. Rev. A* **90** (2014).
- [50] A. Wallraff, D. I. Schuster, A. Blais, L. Frunzio, R.-S. Huang, J. Majer, S. Kumar, S. M. Girvin, and R. J. Schoelkopf, “Strong coupling of a single photon to a superconducting qubit using circuit quantum electrodynamics”, *Nature* **431** (2004).

- [51] P. Eder, “Dual-path receiver for state reconstruction of propagating quantum microwaves”, Master’s thesis, Technische Universität München (2012).
- [52] “Surface Metrology Guide - Profile Parameters”, (2011), URL http://db.materialoptions.com/ASSETSDefense/SEDB/EHC_Alts/Tech_Matls_Info/Surface%20Metrology%20Guide%20-%20Profile%20Parameters.pdf.

Acknowledgement

For the opportunity to write my Master's thesis at the WMI, I would like to thank Prof. Dr. Rudolf Gross.

I also thank Prof. Dr. David Haviland for serving as the KTH supervisor for this thesis.

I am most grateful to my advisor Edwar Xie who provided valuable guidance throughout my work. He was always available for discussions and demonstrated an outstanding willingness to help. I acknowledge especially his instructions to the lab and experimental equipment, as well as his contributions towards the fabrication of the microwave cavities and transmon sample. He deserves further thanks for proofreading this thesis.

I want to thank Dr. Frank Deppe for bringing to my attention the work of quantum information processing group at the WMI, and his proofreading and feedback on the this thesis.

Furthermore, I thank former Bachelor Student Jonathan Müller for his contributions to this project.

For their helpful hints and advice on experimental techniques, I would finally like to thank Dr. Kirill Fedorov, Dr. Edwin P. Menzel, Ling Zhong, Jan Goetz and Max Häberlein from our group.